Supporting Information

Bulk Inclusions of Double Pyridazine Molecular Rotors in Hexagonal Tris(*o*-phenylene)cyclotriphosphazene (TPP)

Jiří Kaleta,[a,b]* Guillaume Bastien,[a] Jin Wen,[a]* Martin Dračínský,[a] Edward Tortorici,[c] Ivana Císařová,[d] Paul D. Beale,[c] Charles T. Rogers,[c] and Josef Michl[a,b]

[a] *Institute of Organic Chemistry and Biochemistry AS CR, Flemingovo nám. 2, 166 10 Prague 6, Czech Republic.*
[b] *Department of Chemistry, University of Colorado, Boulder, CO 80309-0215, United States*
[c] *Department of Physics, University of Colorado, Boulder, CO 80309, United States*
[d] *Department of Inorganic Chemistry, Faculty of Science, Charles University in Prague, Hlavova 2030, 12840 Prague 2, Czech Republic.*

Table of Contents

Parameters of Single Crystals.

Table S1. Parameters of Single Crystals of **1**, **2**, **9**, **18**, **19**, and **21**.

Cmpd.	Crystal System	Space Group	Cell Lengths (Å)	Cell Angles (°)
1	monoclinic	P 2_1/n	*a* 5.8512(2)	*α* 90
			b 8.3937(3)	*β* 93.3020(10)
			c 50.6823(17)	*γ* 90
2	monoclinic	C 2/c	*a* 22.3659(8)	*α* 90
			b 9.9919(4)	*β* 113.8010(10)
			c 10.6756(4)	*γ* 90
9	orthorhombic	P $2_12_12_1$	*a* 8.6776(3)	*α* 90
			b 10.6049(3)	*β* 90
			c 10.8506(4)	*γ* 90
18	tetragonal	P 4_2bc	*a* 10.9366(4)	*α* 90
			b 10.9366(4)	*β* 90
			c 17.1631(8)	*γ* 90
19	monoclinic	P 2_1/n	*a* 7.9200(5)	*α* 90
			b 7.8005(7)	*β* 93.006(3)
			c 15.4524(12)	*γ* 90
21	monoclinic	P 2_1/c	*a* 13.8295(6)	*α* 90
			b 5.7329(2)	*β* 102.868(2)
			c 9.3551(3)	*γ* 90

Amounts of Guest Used for Preparation of Inclusion Compounds.

Table S2. Amounts of Guest Used for Preparation of Inclusion Compounds.

Cmpd.	Guest Weight (mg)	Inclusion Label
1	18.74	30%**1**@TPP-d_{12}
	24.99	40%**1**@TPP-d_{12}
2	12.24	15%**2**@TPP-d_{12}
	24.48	30%**2**@TPP-d_{12}
3	13.77	20%**3**@TPP-d_{12}
	27.53	25%**3**@TPP-d_{12}
4	18.86	15%**4**@TPP-d_{12}
	22.95	30%**4**@TPP-d_{12}
5	15.30	15%**5**@TPP-d_{12}
	25.49	25%**5**@TPP-d_{12}

Estimation of Maximum Guest Loading.

The idea is to virtually rearrange all TPP molecules present in crystalline sample to one long channel and then to evaluate the number of molecules that could be accommodated inside.

Hexagonal TPP has layered structure and one TPP channel is defined by three TPP molecules (each of them participates by one third) within one layer. Two successive layers, which are rotated 60 degrees with respect to each other, are needed to form characteristic hexagonal channels.

A TPP sample with the weight m_{TPP} consists of N molecules ($N = n_{TPP} \times N_A$ where N_A is Avogadro number). The number of molecules N is then equal to number of present TPP layers of the height h, and the length of that one hypothetical channel L is defined as $L = N \times h$.

Knowing the approximate length l of the considered guest, it is possible to evaluate the number of guest molecules which can be inserted into that TPP channel ($N_{guest} = L / l$), then to find the corresponding number of moles ($n_{guest} = N_{guest} / N_A$) and conclude to a maximum loading ratio between the guest and the host (n_{guest} / n_{TPP}) using following equation:

$$\frac{n_{Guest}}{n_{TPP}} = \frac{h}{l}$$

The h is the height of one TPP layer (5.08 Å), and l the length of the considered guest molecules (in Å).

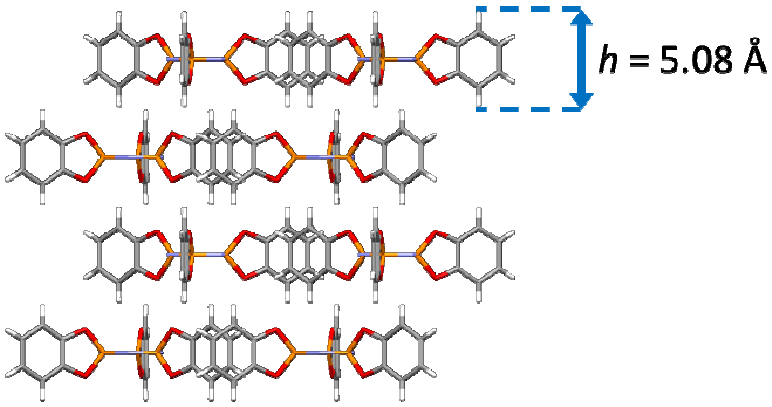

Differential Scanning Calorimetry (DSC).

The DSC trace of neat **1** (Figure S1B) showed two endotherms. A weak one is centered at 226 °C and is probably due to a transition between crystal structures, and a strong one occurs at 250 °C and is assigned to melting. The inclusion 30%**1**@TPP-d_{12} is characterized by a relatively sharp exotherm at 159 °C and almost equally intense endotherm at 230 °C, which is attributed to melting (Figure S1C).

The heating of **2** resulted in complex set of exotherms with maxima at 272 °C, 275 °C, 283 °C, and the most intense one at 291 °C, suggesting gradual decomposition (Figure S1D). The DSC profile of 30%**2**@TPP-d_{12} consists of two very weak exotherms centered at 148 °C and 166 °C, one much stronger at 271 °C, and one endotherm at 238 °C (Figure S1E). The peak at ~240 °C could be due to melting, while the one at ~270 °C is attributed to exothermic decomposition of **2**.

The DSC traces of **3** showed a weak exotherm at 262 °C and a strong one at 283 °C, which could be attributed to explosive decomposition of the strained acetylene substituted BCP cage (Figure S1F). The DSC traces of 20%**3**@TPP-d_{12} (Figure S1G) contain a weak exotherm at 156 °C and an endotherm attributed to melting at 244 °C, which is overlapped with a broad exotherm peaking at 256 °C and due to decomposition of the guest molecules.

The DSC analysis of **4** revealed one strong exotherm at 255 °C with a small shoulder at 250 °C, due to explosive decomposition (Figure S1H). A similar strong exotherm at ~253 °C is also present in 15%**4**@TPP-d_{12}. The melting of this inclusion is characterized by an endotherm at 246 °C (Figure S1I).

The limited stability of **5** upon heating is clearly demonstrated by one strong exotherm at 239 °C in its DSC trace (Figure S1J). This peak is associated with explosive decomposition of this diyne substituted BCP cage. The DSC traces of 15%**5**@TPP-d_{12} show two exotherms (one small and broad centered at ~158 °C, and one much stronger peaking at ~260 °C), and one endotherm at 245 °C, which is overlapped with the high-temperature exotherm (Figure S1K).

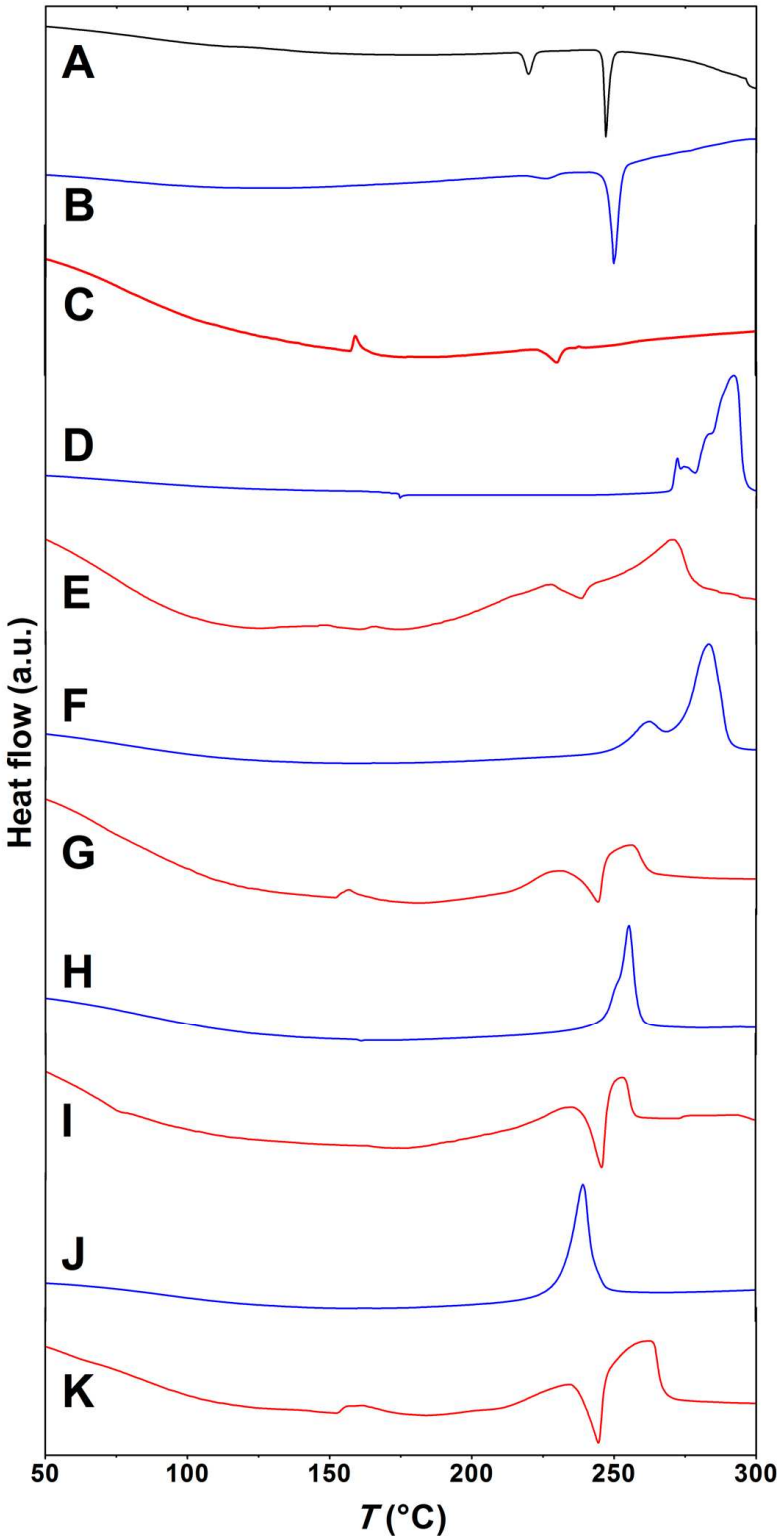

Figure S1. DSC traces from 50 °C to 300 °C for guest-free TPP-d_{12} (A), neat molecular rotors **1** - **5** (blue lines, **1**: B, **2**: D, **3**: F, **4**: H, and **5**: J), and bulk inclusions (red lines, 30%**1**@TPP-d_{12}: C, 30%**2**@TPP-d_{12}: E, 20%**3**@TPP-d_{12}: G, 15%**4**@TPP-d_{12}: I, and 15%**5**@TPP-d_{12}: K).

Transmission Electron Microscope Imaging.

Morphology of 30%**1**@TPP-d_{12} was determined by TEM (Figure S2). The sample consists of conglomerates composed mostly of disks with a ~50 nm diameter and ~25 nm thickness.

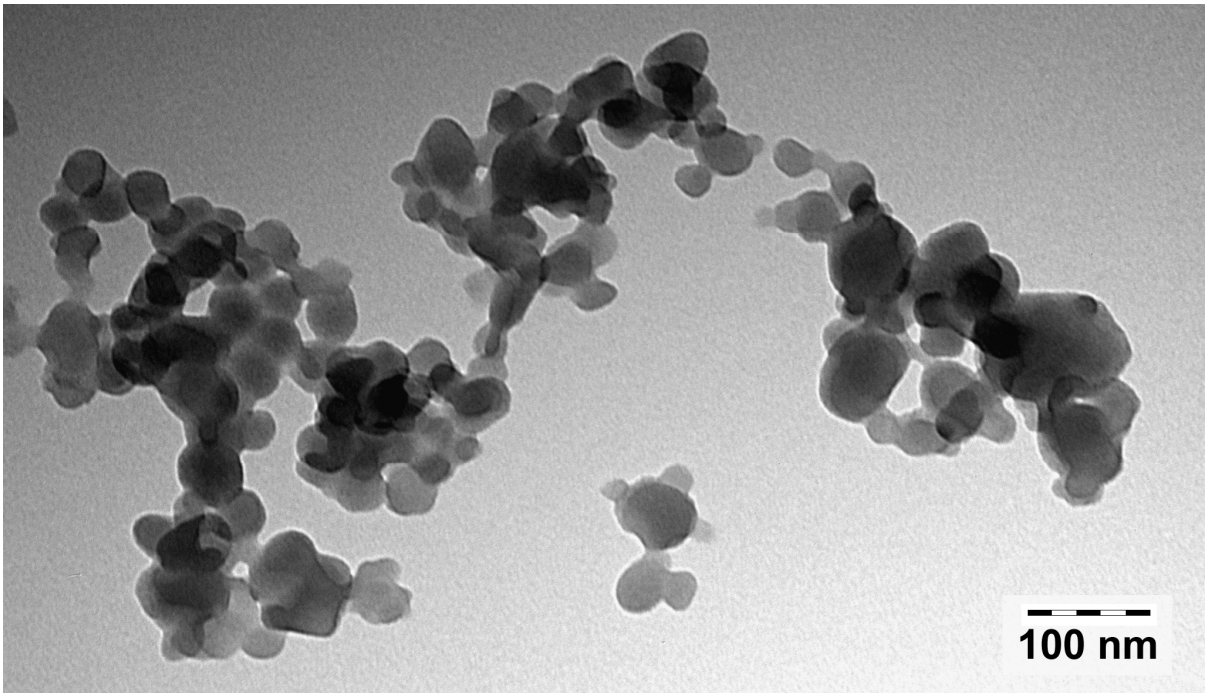

Figure S2. TEM of 30%**1**@TPP-d_{12}.

Figure S3. ^{13}C NMR spectrum of **3** in solution (A), ^{13}C CP MAS NMR of neat **3** (B), 20%**3**@TPP-d_{12} (C), and 25%**3**@TPP-d_{12} (D). ^{31}P SPE NMR: 20%**3**@TPP-d_{12} (E), 25%**3**@TPP-d_{12} (G), and ^{31}P CP MAS NMR: 20%**3**@TPP-d_{12} (F), 25%**3**@TPP-d_{12} (I). The peaks marked by asterisks are spinning side bands.

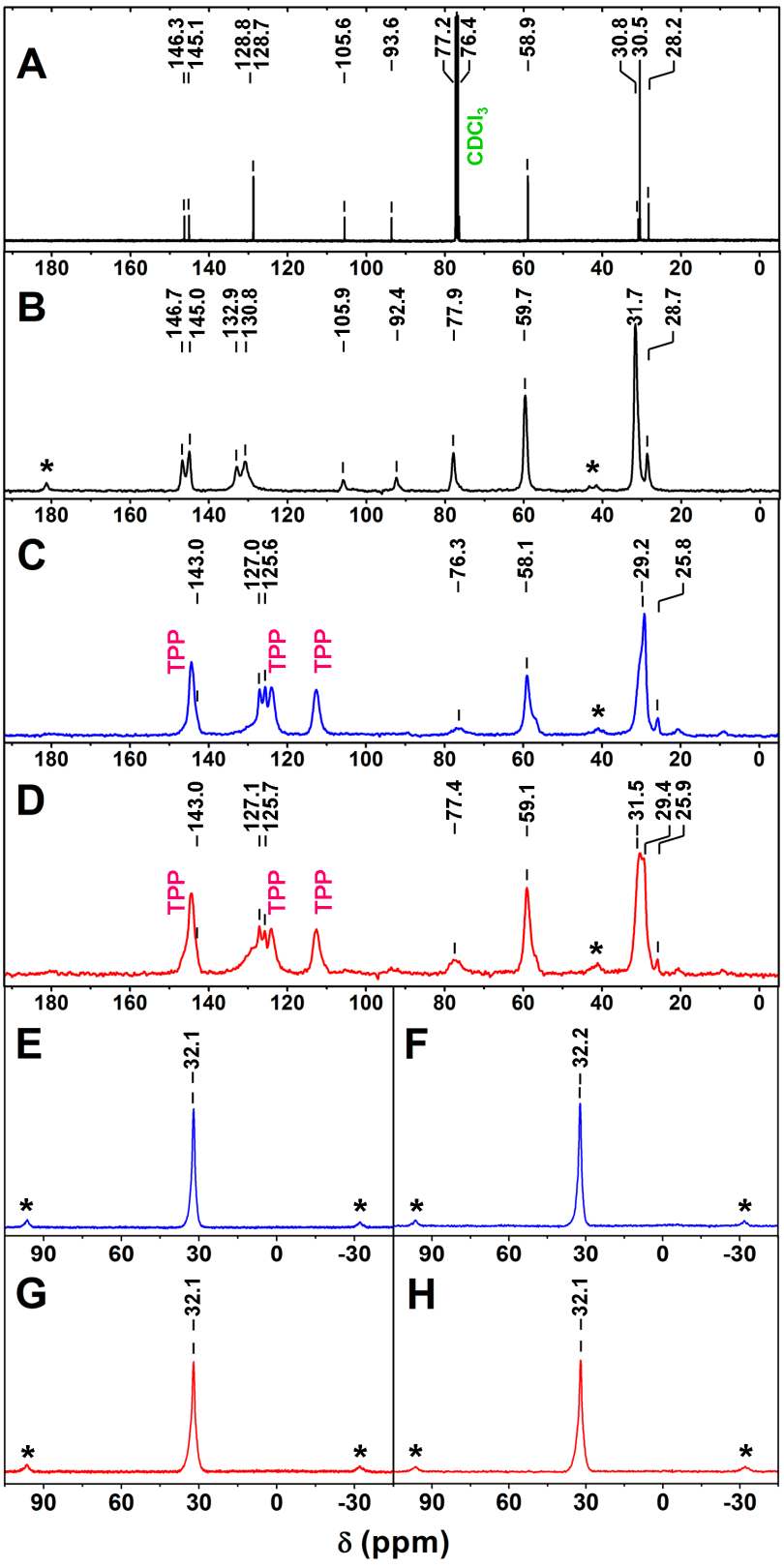

Figure S4. ^{13}C NMR spectrum of **4** in solution (A), ^{13}C CP MAS NMR of neat **4** (B), 15%**4**@TPP-d_{12} (C), and 30%**4**@TPP-d_{12} (D). ^{31}P SPE NMR: 15%**4**@TPP-d_{12} (E), 30%**4**@TPP-d_{12} (G), and ^{31}P CP MAS NMR: 15%**4**@TPP-d_{12} (F), 30%**4**@TPP-d_{12} (I). The peaks marked by asterisks are spinning side bands.

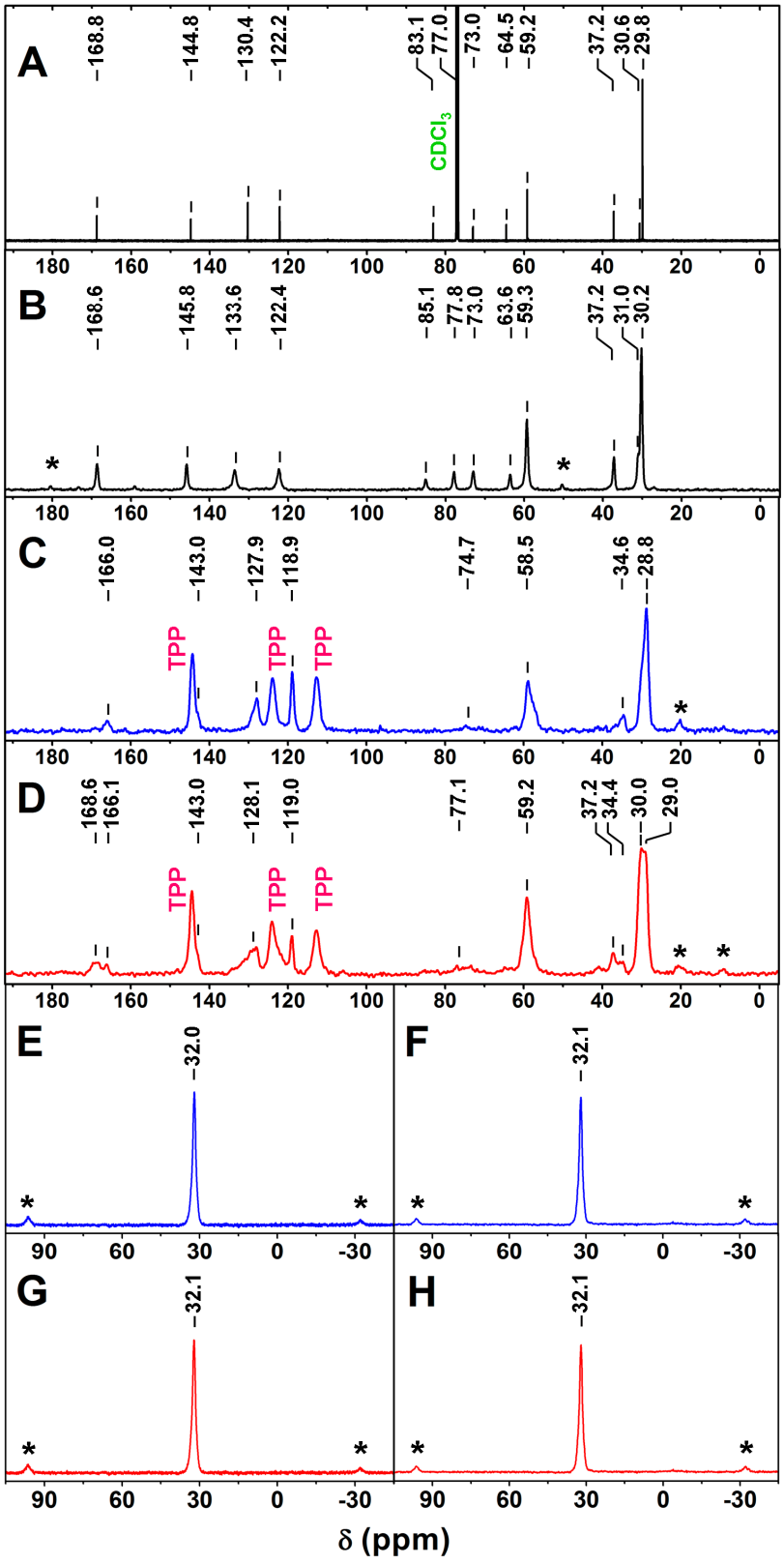

Figure S5. ^{13}C NMR spectrum of **5** in solution (A), ^{13}C CP MAS NMR of neat **5** (B), 15%**5**@TPP-d_{12} (C), and 25%**5**@TPP-d_{12} (D). ^{31}P SPE NMR: 15%**5**@TPP-d_{12} (E), 25%**5**@TPP-d_{12} (G), and ^{31}P CP MAS NMR: 15%**5**@TPP-d_{12} (F), 25%**5**@TPP-d_{12} (I). The peaks marked by asterisks are spinning side bands.

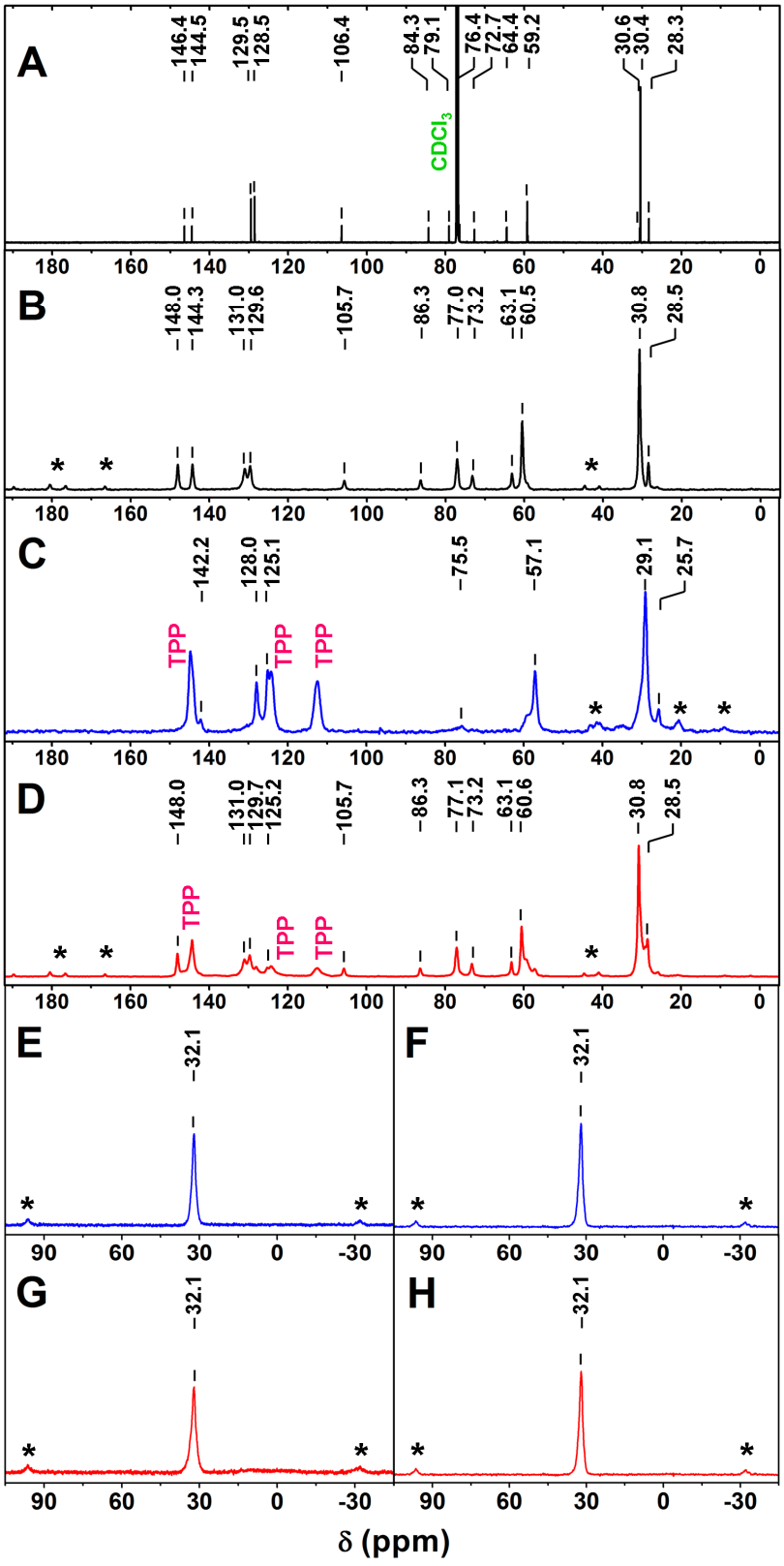

Figure S6. PXRD spectra of 30%**1**@TPP-d_{12} (A), 40%**1**@ TPP-d_{12} (B), 15%**2**@ TPP-d_{12} (C), 30%**2**@ TPP-d_{12} (D), 20%**3**@ TPP-d_{12} (E), 25%**3**@ TPP-d_{12} (F), 15%**4**@ TPP-d_{12} (G), 30%**4**@ TPP-d_{12} (H), 15%**5**@ TPP-d_{12} (I), and 25%**5**@ TPP-d_{12} (J).

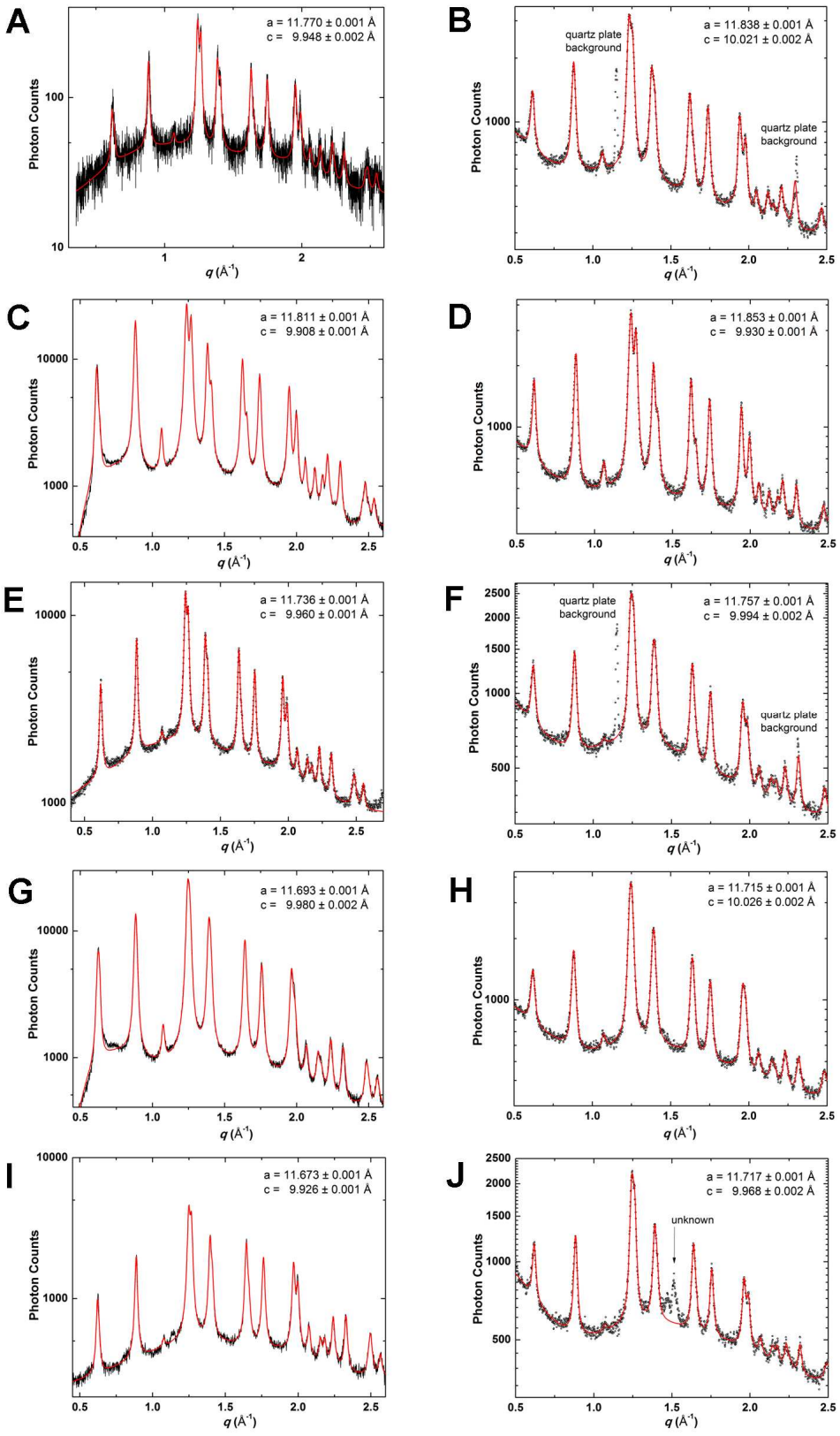

Figure S7. Dielectric spectra of 30%**1**@TPP-d_{12} (A), 40%**1**@ TPP-d_{12} (B), 15%**2**@ TPP-d_{12} (C), 30%**2**@ TPP-d_{12} (D), 20%**3**@ TPP-d_{12} (E), 25%**3**@ TPP-d_{12} (F), 15%**4**@ TPP-d_{12} (G), 30%**4**@ TPP-d_{12} (H), 15%**5**@ TPP-d_{12} (I), and 25%**5**@ TPP-d_{12} (J).

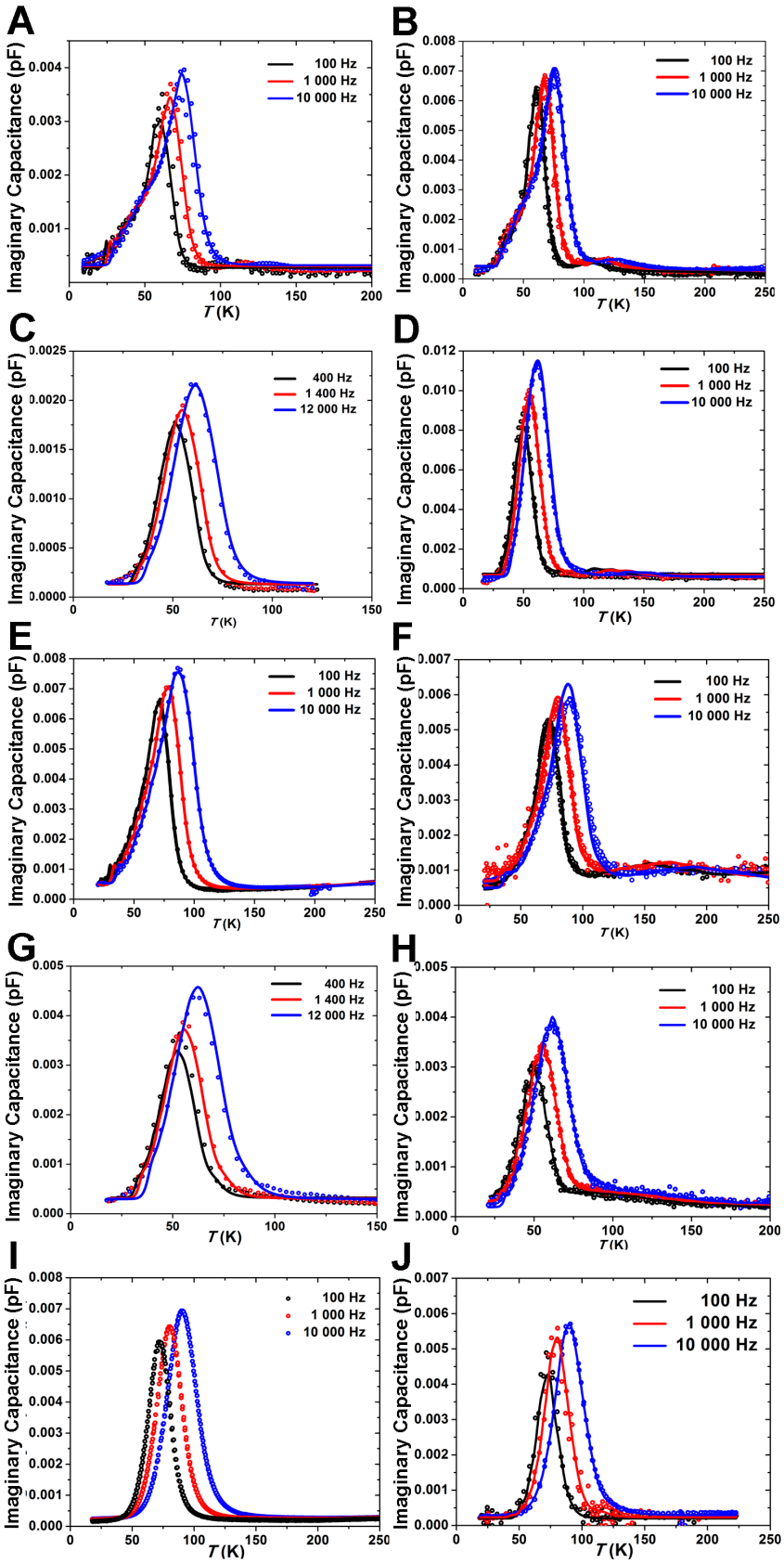

Table S3. Chemical shifts of molecular rotors **1** – **5** in $CDCl_3$ solution, neat **1** - **5** and their bulk inclusions.

Sample	Spectrum	Chemical Shift (ppm)													
		a	**b**	**c**	**d**	**e**	**f**	**g**	**h**	**i**	**j**	**k**	**l**	**m**	**n**
1	^{13}C	88.8	144.9	130.0	122.5	169.2	37.2	29.9	-	-	-	-	-	-	-
	^{13}C CP MAS	89.6	144.7	131.9	127.5	169.6	37.9	30.6	-	-	-	-	-	-	-
30%**1**@TPP-d_{12}	^{13}C CP MAS	x	143.2	127.1	119.3	166.2	35.2	29.4	-	-	-	-	-	-	-
	$^{13}C(\delta_{TPP}-\delta_S)$	x	-1.7	-2.9	-3.2	-3.0	-2.0	-0.5	-	-	-	-	-	-	-
2	^{13}C	58.9	30.7	91.6	77.3	145.4	129.4	122.2	168.4	37.0	29.9	-	-	-	-
	^{13}C CP MAS	59.7	30.9	90.8	79.6	145.0	133.4	126.9	169.0	37.8	30.2	-	-	-	-
				89.9	77.8	144.7	129.0	125.1	167.5	36.8		-	-	-	-
15%**2**@TPP-d_{12}	^{13}C CP MAS	56.7	~29	x	x	143.2	127.0	119.0	165.6	34.2	28.5	-	-	-	-
	$^{13}C(\delta_{TPP}-\delta_S)$	-2.2	-1.7	x	x	-2.2	-2.4	-3.2	-2.8	-2.8	-1.4	-	-	-	-
3	^{13}C	58.9	30.8	93.6	77.2	145.1	128.8	128.7	146.3	76.4	105.6	28.2	30.5	-	-
	^{13}C CP MAS	59.7	~32	92.4	77.9	145.0	132.9	130.8	146.7	77.9	105.9	28.7	31.7	-	-
20%**3**@TPP-d_{12}	^{13}C CP MAS	58.1	~30	x	x	143.0	127.0	125.6	x	x	x	25.8	29.2	-	-
	$^{13}C(\delta_{TPP}-\delta_S)$	-0.8	-0.8	x	x	-2.1	-1.8	-3.1	x	x	x	-2.4	-1.3	-	-
4	^{13}C	59.2	30.6	83.1	64.5	77.0	73.0	144.8	130.4	122.2	168.8	37.2	29.8	-	-
	^{13}C CP MAS	59.3	31.0	85.1	63.6	77.8	73.0	145.8	133.6	122.4	168.6	37.2	30.2	-	-
15%**4**@TPP-d_{12}	^{13}C CP MAS	58.5	~30	x	x	x	x	143.0	127.9	118.9	166.0	34.6	28.8	-	-
	$^{13}C(\delta_{TPP}-\delta_S)$	-0.7	-0.6	x	x	x	x	-1.8	-2.5	-3.3	-2.7	-2.6	-1.0	-	-
5	^{13}C	59.2	30.6	84.3	64.4	79.1	72.7	144.5	129.5	128.5	146.4	76.4	106.4	28.3	30.4
	^{13}C CP MAS	60.5	~31	86.3	63.1	77.0	73.2	144.3	131.0	129.6	148.0	77.0	105.7	28.5	30.8
15%**5**@TPP-d_{12}	^{13}C CP MAS	57.1	~29	x	62.3	x	68.2	142.2	128.0	125.1	x	x	x	25.7	29.1
	$^{13}C(\delta_{TPP}-\delta_S)$	-2.1	-1.6	x	-2.1	x	-4.5	-2.3	-1.5	-3.4	x	x	x	-2.6	-1.3

x = values are not available (peaks are absent or overlap with neighboring signals)

Figure S8. Top and side views of 7-channel model of TPP lattice.

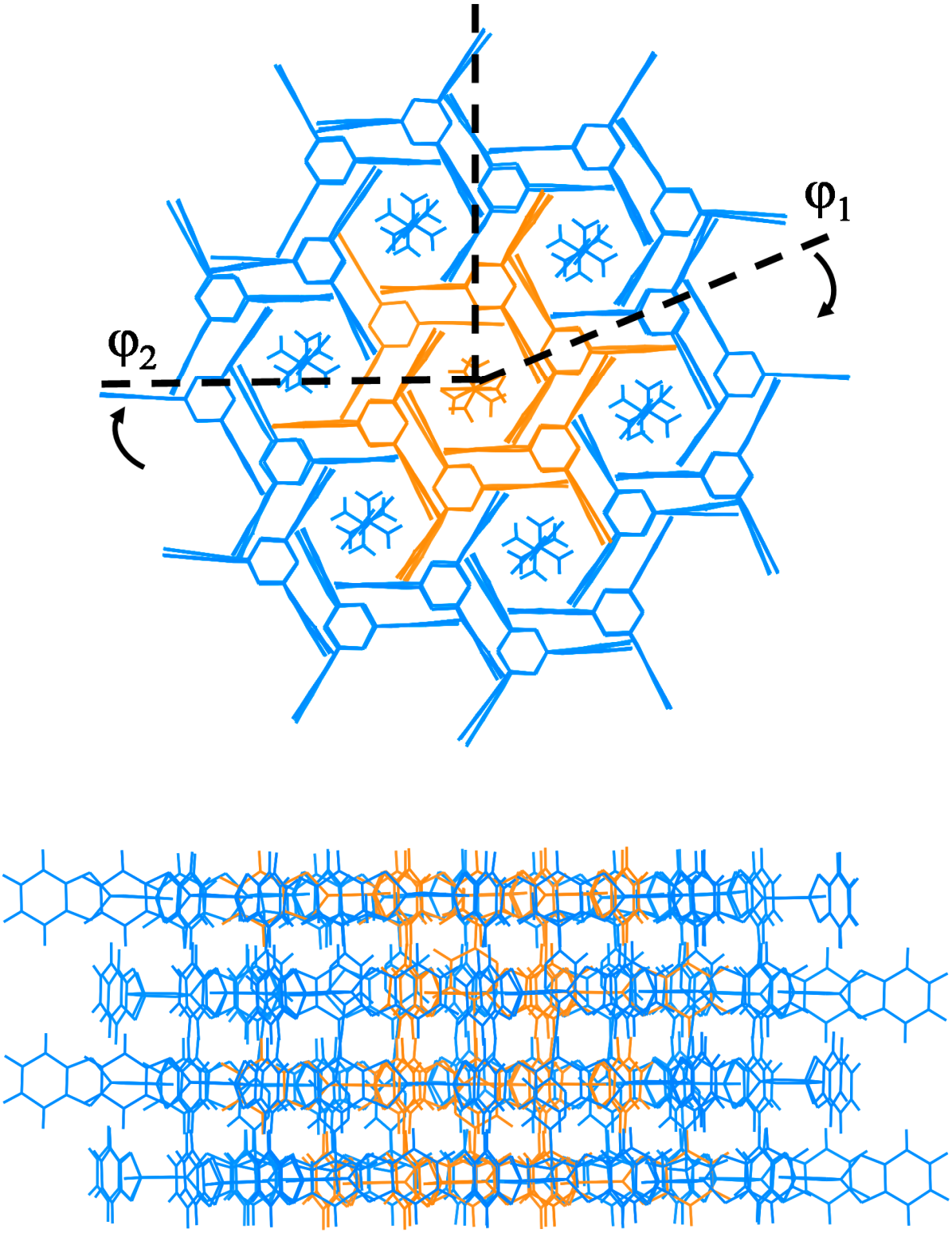

Assuming that the local rotational potential seen by a dipole rotator in a particular TPP layer reflects the three-fold symmetry, we expect a rotational potential landscape with three wells. For the various double pyridazine rotor molecules, placing one of the dipole rotators in a given layer then places the second dipole in a layer that is either 6.7 Å away for **1**, 12.7 Å away for **2** and **3**, and 17.8 Å away for **4** and **5**. Given the 5 Å layer spacing and the alternating 60 degree rotations, this picture suggests that dilute double pyridazine inclusion compounds will fall into one of two classes with respect to local rotational potential landscape, depending upon whether the dipoles of individual double pyridazine rotor molecules are separated by an odd or even number of TPP layers. For example, dipole pairs for inclusion compounds of **1** are separated by 6.7 Å, placing the individual dipoles roughly one TPP layer spacing apart. In other words, they are in adjacent TPP layers of the bilayer crystal structure. So, they experience local TPP contributions to the rotational potential that will be three fold, but rotated by 60 degrees with respect to each other. Similarly, inclusions of **4** and **5** will have dipoles separated by approximately 3 layers, so again, will have dipoles that experience local three-fold environments, but where the dipole local environments are rotated by 60 degrees. In the other class are inclusions of **2** and **3**, where the dipoles in a given double pyridazine are separated by two TPP layers. Each dipole is in a local three-fold environment, and the local environments are oriented so that they are aligned. A dipole moving in a three-fold local potential will have a neighbor moving also in a three-fold potential and the potentials are rotationally aligned.

In the simplest picture of three-fold potential barriers, dilute inclusion compounds of **1**, **4**, and **5** allow for dipoles in the different layers to be anti-ferroelectrically aligned, with one dipole possibly in a well, and the other dipole in another well that can be 120 degrees away plus the 60 degree rotation between layers leading to a total 180 degrees separation. Given two dipole moments each of which can occupy three potential wells i.e., nine possible configurations, three of these configurations are anti-ferroelectric and lead to a net dipole moment of zero. The other six configurations lead to partial alignment, a situation we refer to as “ferrielectric”, and a net moment of magnitude equal to the single dipoles and oriented at 60 degrees to each of the two. By comparison inclusion compounds of **2** and **3** have double pyridazine dipole pairs where the nine configurations break into three where the dipoles are aligned leading to a net dipole moment that is the sum of the two, and six ferrielectric configurations where the net moment is again equal to a single moment in magnitude and is again oriented at 60 degrees to the two rotators. These arguments suggest that the local barriers to rotation could lead the dipole moment pairs within an individual double pyridazine molecule to have possible anti-ferroelectric and ferrielectric orientations for inclusions of **1**, **4,** and **5**, but only ferroelectric or ferrielectric orientations for inclusions of **2** and **3**.

For inclusions at higher double pyridazine densities, similar arguments must be applied to the locations of neighboring molecules and the associated spacing and rotational potentials for all rotors along the channel. For the molecules considered here, the separation between the nearest dipoles on neighboring double pyridazine molecules is estimated in Chart 1 as either 6.8 Å for fully populated inclusions of **1**, **2**, or **4** or 12.0 Å for inclusions of **3** or **5**, based on the assumption of full packing of rotor molecules in the inclusion. These distances are not commensurate with the 5 Å layer spacing of TPP, but suggest that nearest neighbor dipoles for inclusions of **1**, **2**, or **4** would have the possibility of anti-ferroelectric/ferrielectric orientation, whereas nearest neighbor dipoles for inclusions of **3** or **5** would favor the ferroelectric/ferrielectric orientations.

Relative Dielectric Susceptibility

The capacitance of our interdigital capacitors can be analyzed using conformal mapping techniques.[1,2] To an excellent approximation, an empty interdigital capacitor such as

those used in our work, where the device is fabricated from gold electrodes on silica substrates with interdigital electrode finger widths and finger spacings that are small compared to the silica substrate thickness (10 μm fingers and spacings compared to 400 μm substrate thickness) has a total capacitance that can be calculated as arising from a half-space with the relative dielectric constant of silica, $\varepsilon_{SiO2}(T)$ (near 3.8 at 300 K), and a second half space with the dielectric constant of roughly 1 for air or in vacuum (Equation 2).

$$C_{empty}(T) \approx [1 + \varepsilon_{SiO2}(T)]C_{Geom} \quad (2)$$

Here, C_{Geom} is a geometry-dependent overall capacitance that is determined by finger spacing, finger width, and the number of fingers in the device, and is of order 350 fF for our devices, both by calculation and measurement.

Similarly, a device that is loaded with a powder inclusion will show a loaded capacitance that is increased due to replacing the electric response of vacuum with the dielectric response of the powder. Assuming that the powder has a partial filling fraction, α, and an inclusion relative dielectric response function, $\varepsilon_{Inclusion}(T)$ (Equation 3).

$$\begin{aligned} C_{loaded}(T) &\approx [1(1 - \alpha) + \alpha\varepsilon_{Inclusion}(T) + \varepsilon_{SiO2}(T)]C_{Geom} \\ &= \alpha(\varepsilon_{Inclusion} - 1)C_{Geom} + C_{empty} \end{aligned} \quad (3)$$

The difference between relative dielectric response function and unity is just the dielectric susceptibility, $\chi_{Inclusion}(T)$. Therefore, we can determine the product of powder filling fraction and relative dielectric susceptibility via equation 4.

$$\alpha\chi_{Inclusion} = (C_{loaded} - C_{empty})/C_{Geom} \quad (4)$$

Both the partial filling fraction, α, and the geometric capacitance, C_{Geom}, can be functions of temperature due to thermal expansion coefficients. However, that dependence is typically very weak compared to the changes in loaded capacitance due to the temperature-dependent dipole response of the inclusion powders. By ignoring the temperature dependences of α and C_{Geom}, we can compare the dielectric susceptibility temperature dependence to that at any reference temperature, T_{ref}, as in equation 5:

$$\chi_{Inclusion}(T) / \chi_{Inclusion}(T_{ref}) = [(C_{loaded}(T) - C_{empty}(T))] / [(C_{loaded}(T_{ref}) - C_{empty}(T_{ref}))] \quad (5)$$

We refer to this ratio as the relative dielectric susceptibility. It is very easy to calculate directly from the measured temperature-dependent loaded and empty capacitor values. Taking the reference temperature at lowest temperatures, where the behavior of the dipole moments has been frozen out, leaving only the behavior of the polarizable TPP host and included molecules then allows us to compare the relative importance of dipole rotor motion in the different inclusion compounds. It is this relative susceptibility that is shown in our Figure 12 for the five fully loaded inclusion compounds.

Nine-State Dielectric Response Models

As we discussed above and as is shown schematically in Figure S9 dipole pairs within an individual double pyridazine molecule can be approximately modeled as having nine distinct combinations of dipole orientation. For molecules **1**, **4**, and **5**, where dipole-dipole spacing is respectively about one TPP layer or three TPP layers, the local three-fold potentials provide three configurations that allow the dipoles to point in opposite directions, and six

which allow for only partial dipole-dipole alignment. Similarly, the intermolecular dipole spacing of 15 Å for **4** and **5** gives roughly three layer spacing and leads again to either anti-aligned configurations or partially aligned configurations. In comparison, **2** and **3** have intramolecular dipole-dipole separation of roughly 12.7 Å, or just over two TPP layers, and therefore find that the two dipoles live in identical three-fold rotation potentials (Figure S9B). In this case, there are no anti-aligned configurations, but instead three fully aligned and six partially aligned configurations for the intramolecular dipoles. For **1**, **2**, and **4** inter-molecular dipoles are again expected to have 10 Å separation, two TPP layers, and again possible aligned configurations, so the net effect is to have a set of well systems allowing for a mixture of aligned, anti-aligned, and partly aligned or configurations. Each of the double pyridazines is listed in Table 6 as having a variety of such odd-layer or even-layer configurations.

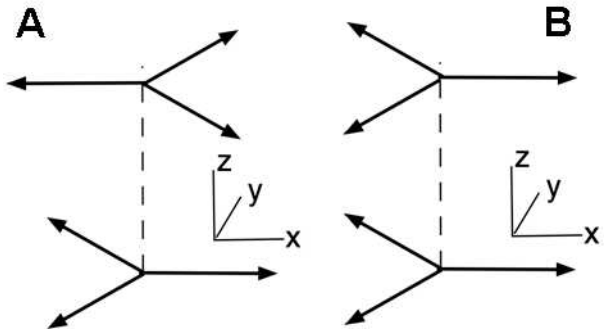

Figure S9. Simple models for possible alignments of neighboring dipoles within one TPP channel: the case where dipoles are located an odd (A) and even (B) number of TPP layers apart.

We have developed two simple statistical mechanics models for these two different nine-state local models.

In each case, there are nine possible energy states. We assume a common energy in the nine wells, an energy term, $-\vec{p}g\vec{E}$, for each dipole of the pair due to possible externally applied electric field, $\vec{E}$, and energy differences that arise only the dipole-dipole energies due to the different alignments. Given these dipole energies, the Partition Function, *Z*, is a sum of the nine Boltzmann factors that depend upon state energies, $\varepsilon_1 - \varepsilon_9$, of which in zero applied field three are equal (anti-aligned low energies for the odd-layer cases and aligned high energies for the even-layer cases) and six more are equal, but different. Then (Equation 6),

$$Z_{(odd,even)} = \sum_{i=1}^{9} \exp\left(-\varepsilon_{(odd,even),i} \big/ k_B T\right) \tag{6}$$

The system free energy is then (Equation 6):

$$F_{(odd,even)} = -k_B T \ln Z_{(odd,even)} \tag{7}$$

The net dipole moment cartesian components and elements of the dipole susceptibility tensor of such a nine-state system are then respectively (Equation 7):

$$p_{(odd,even),(x,y,z)} = \nabla_{E_{(x,y,z)}} F_{(odd,even)} \tag{8}$$

where the gradient is taken with respect to the components of the applied electric field, and (Equation 9):

$$\chi_{(odd,even)ij} = \nabla_{E_i} p_{(odd,even)j} \tag{9}$$

These results determine the dipole moment and susceptibility for arbitrary applied electric fields. Assuming a system of independent nine-state systems of volume density *N/V*, we find that the zero-field susceptibilities are, assuming that the asymmetry is due to point dipolar interactions between dipoles some distance, *a*, apart (Equation 10):

$$\chi_{odd} \approx \frac{N}{V}\frac{p^2}{3k_BT}\frac{9e^{-S/2k_BT}}{\left(6e^{-S/2k_BT}+3e^{+S/k_BT}\right)} \text{ and } \chi_{even} \approx \frac{N}{V}\frac{p^2}{3k_BT}\frac{\left(3e^{+S/2k_BT}+6e^{-S/k_BT}\right)}{\left(6e^{+S/2k_BT}+3e^{-S/k_BT}\right)} \text{ with } S \approx \frac{3p^2}{8\pi\varepsilon\varepsilon_0 a^3} \tag{10}$$

These susceptibilities obtain down to low enough temperatures where the kinetics of barrier crossing freeze out dipole motion. They are identical for zero asymmetry. Finite asymmetry leads to a suppression of susceptibility for the odd layer case, while the even case retains the Curie-like behavior.

References

1. Wu, H.-D.; Zhang, Z.; Barnes, F. *IEEE Transactions of Applied Superconductivity* **1994**, *4*, 156-160.

2. Galt, D. "Dielectric properties of thin film $SrTiO_3$ at Microwave Frequencies" University of Colorado thesis, **1996**. (URL: http://libraries.colorado.edu/-record=b2674427~S3)

^{1}H NMR (400 MHz, $CDCl_3$): 1,2-Bis(6-*tert*-butylpyridazin-3-yl)ethyne (**1**)

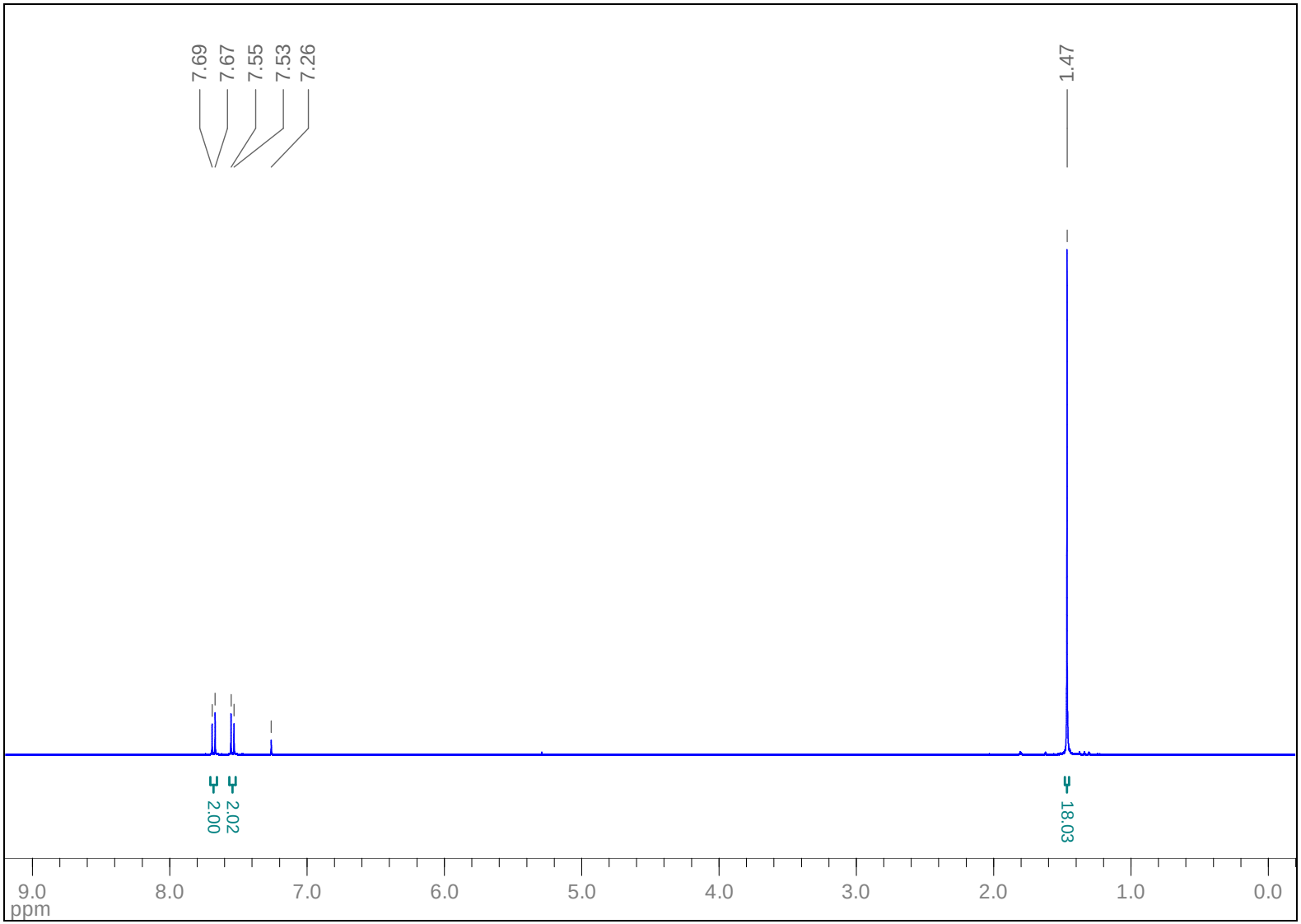

^{13}C {^{1}H} NMR (100 MHz, $CDCl_3$): 1,2-Bis(6-*tert*-butylpyridazin-3-yl)ethyne (**1**)

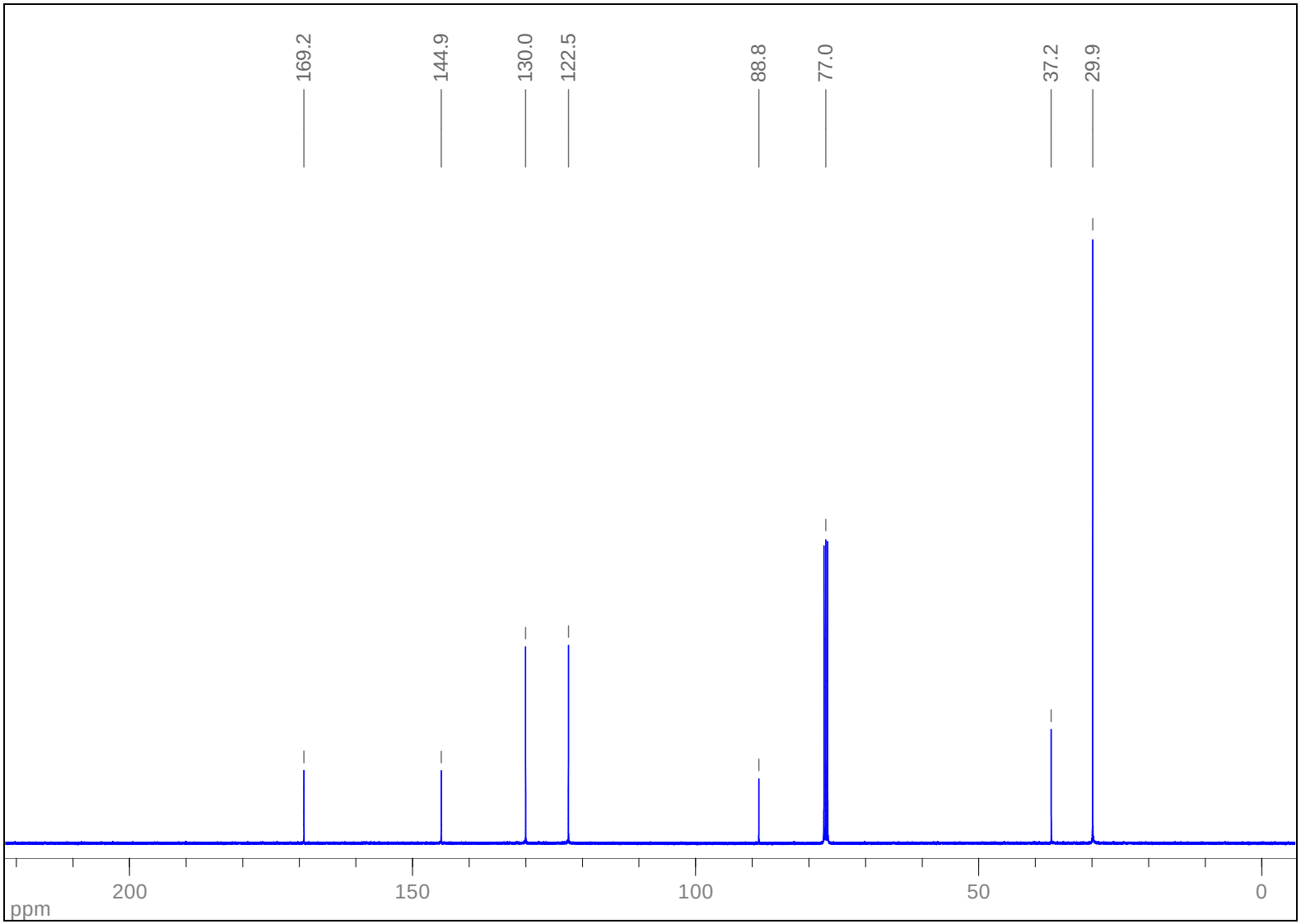

^{13}C APT NMR (100 MHz, $CDCl_3$): 1,2-Bis(6-*tert*-butylpyridazin-3-yl)ethyne (**1**)

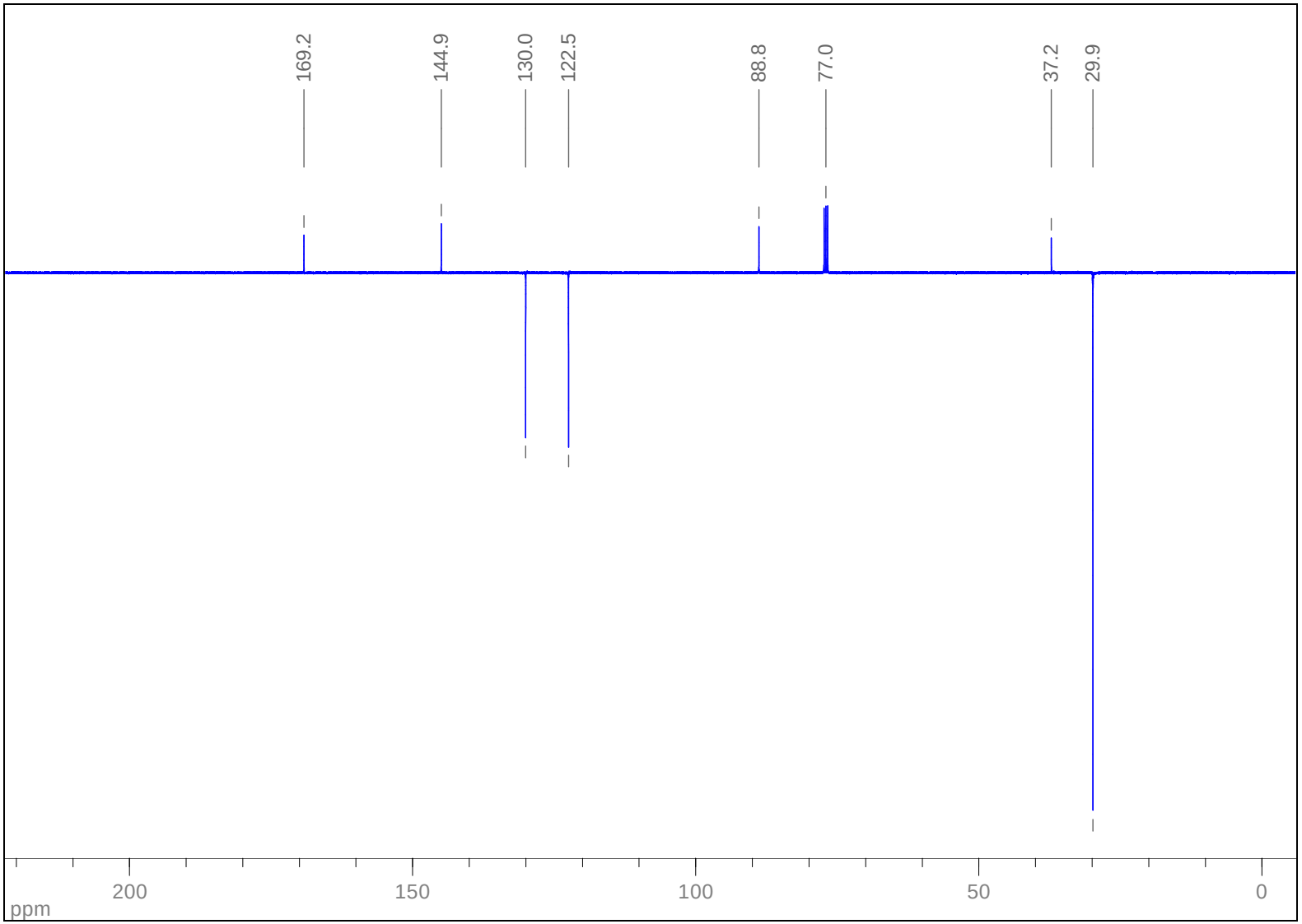

HSQC ($CDCl_3$): 1,2-Bis(6-*tert*-butylpyridazin-3-yl)ethyne (**1**)

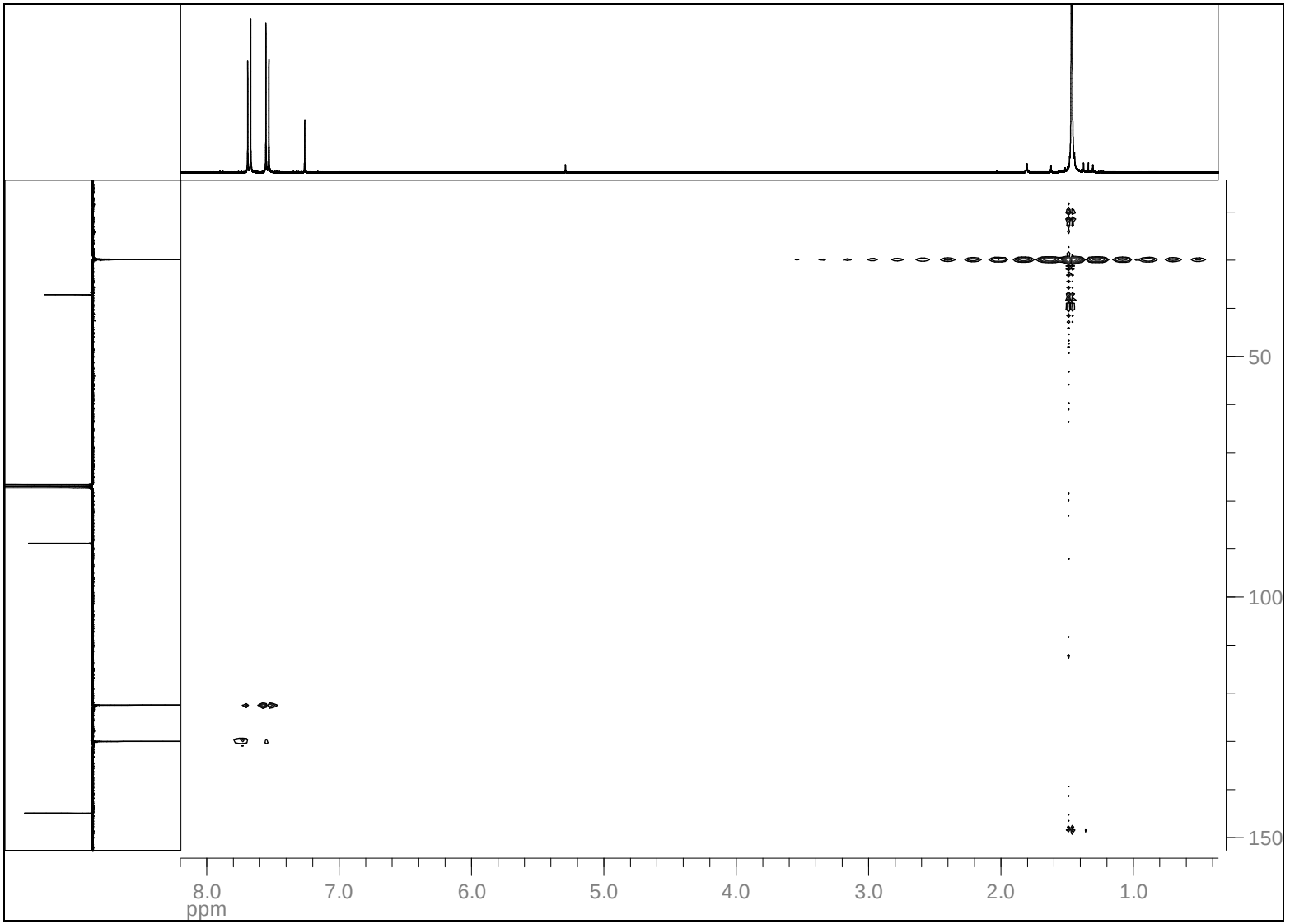

HMBC ($CDCl_3$): 1,2-Bis(6-*tert*-butylpyridazin-3-yl)ethyne (**1**)

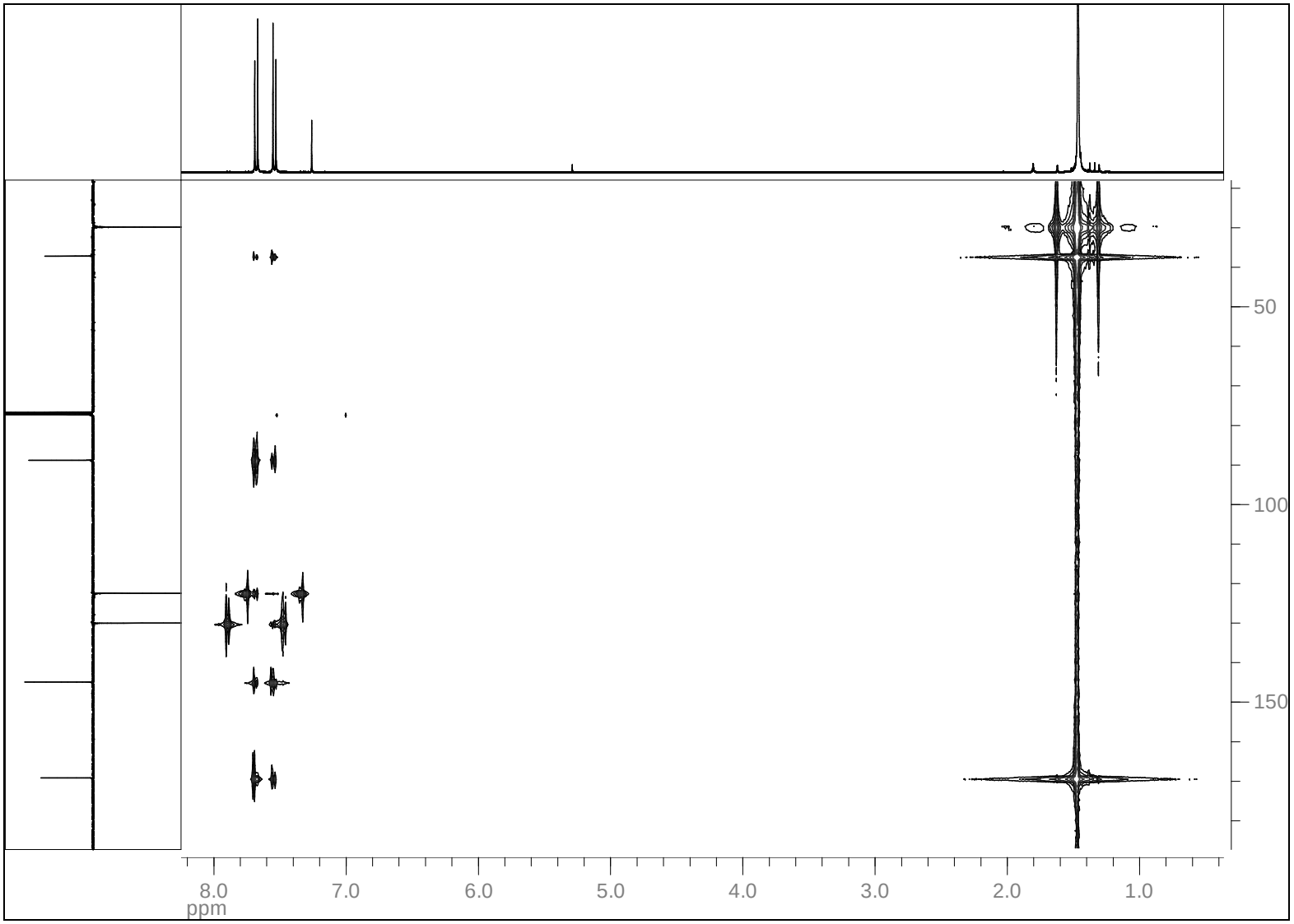

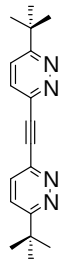

^{1}H NMR (400 MHz, $CDCl_3$): 1,3-Bis((6-*tert*-butylpyridazin-3-yl)ethynyl)bicyclo[1.1.1]pentane (**2**)

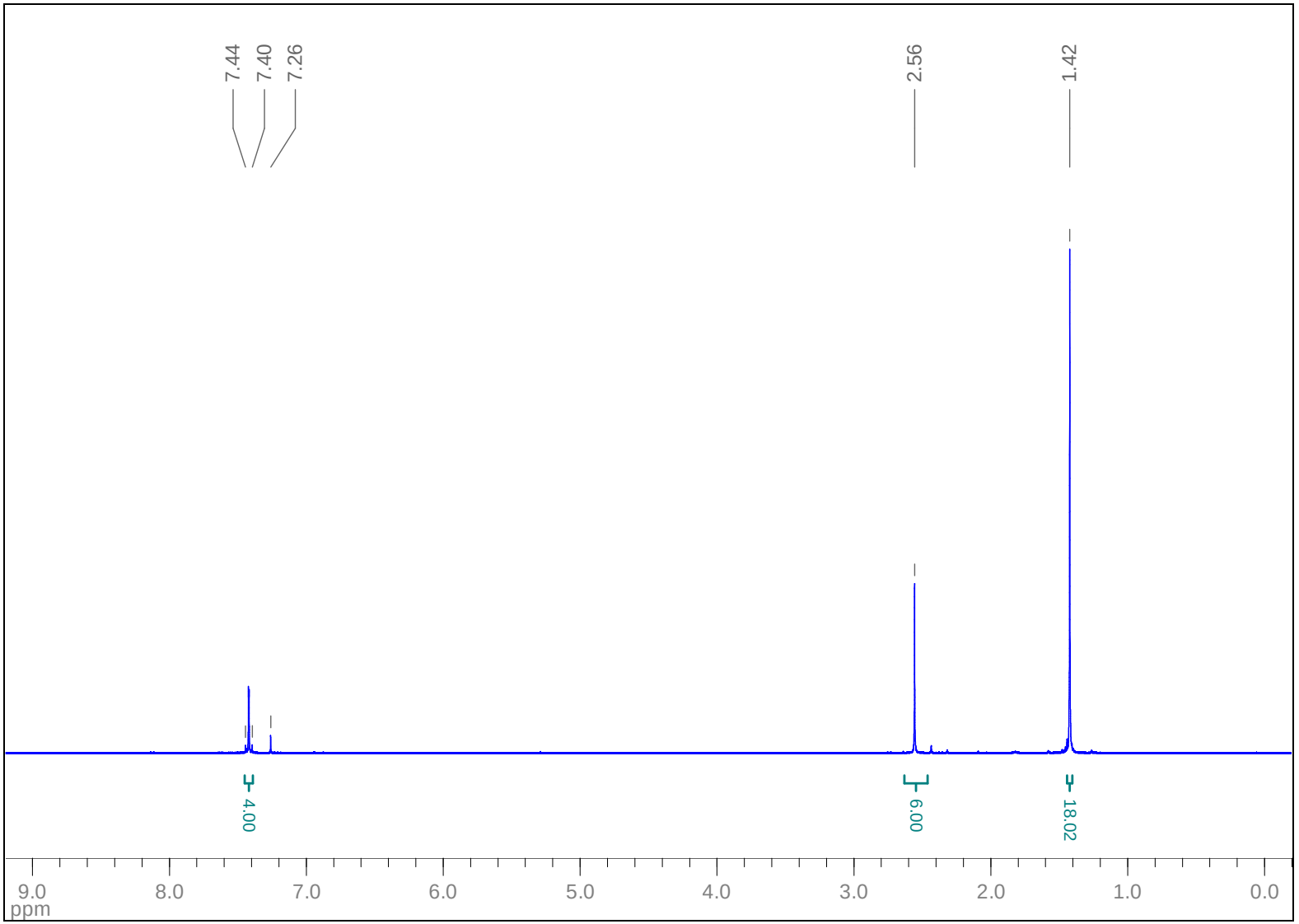

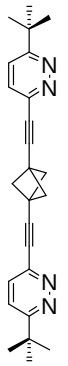

^{13}C {^{1}H} NMR (100 MHz, $CDCl_3$): 1,3-Bis((6-*tert*-butylpyridazin-3-yl)ethynyl)bicyclo[1.1.1]pentane (**2**)

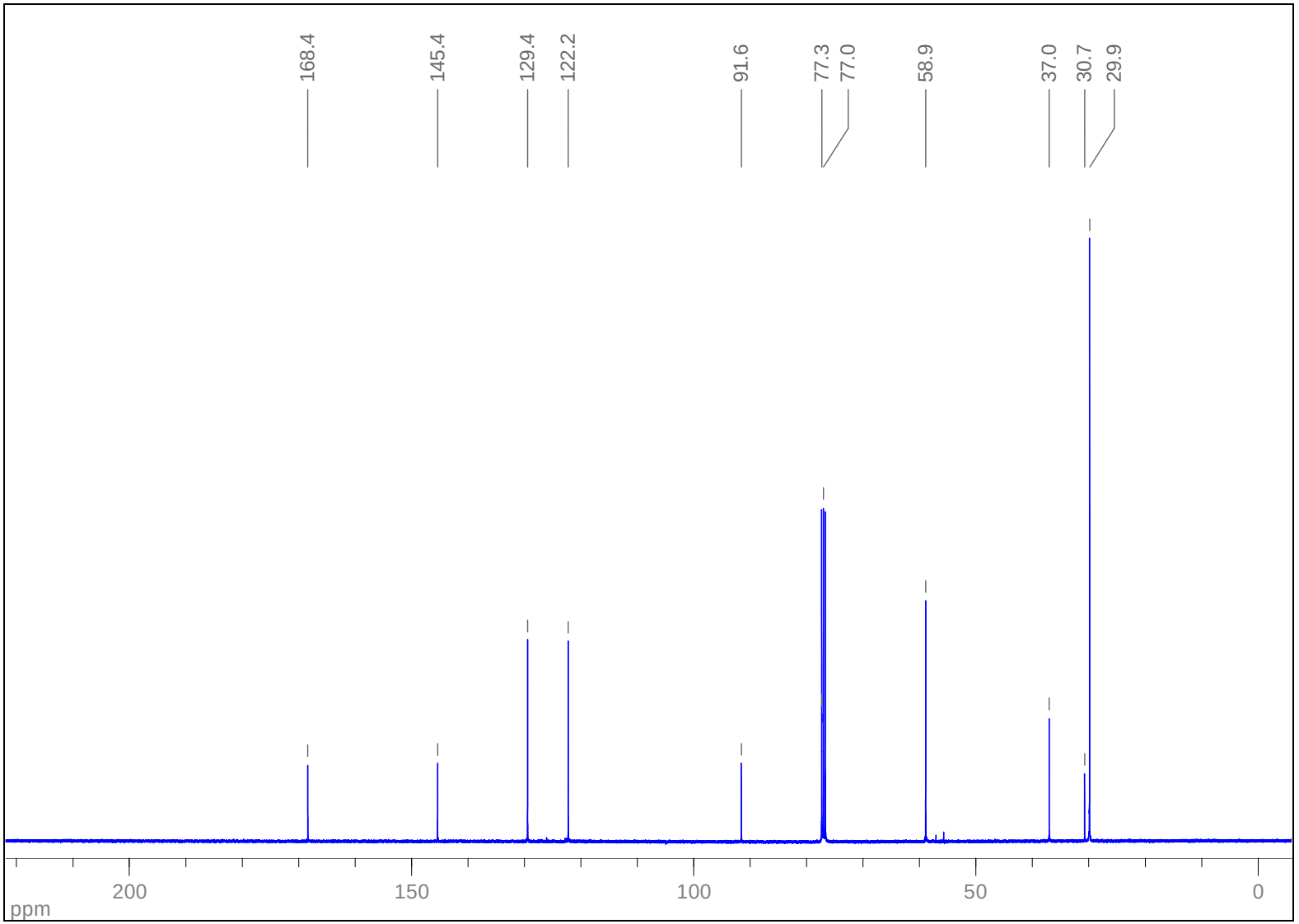

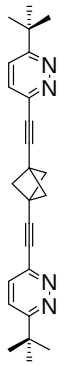

^{13}C APT NMR (100 MHz, $CDCl_3$): 1,3-Bis((6-*tert*-butylpyridazin-3-yl)ethynyl)bicyclo[1.1.1]pentane (**2**)

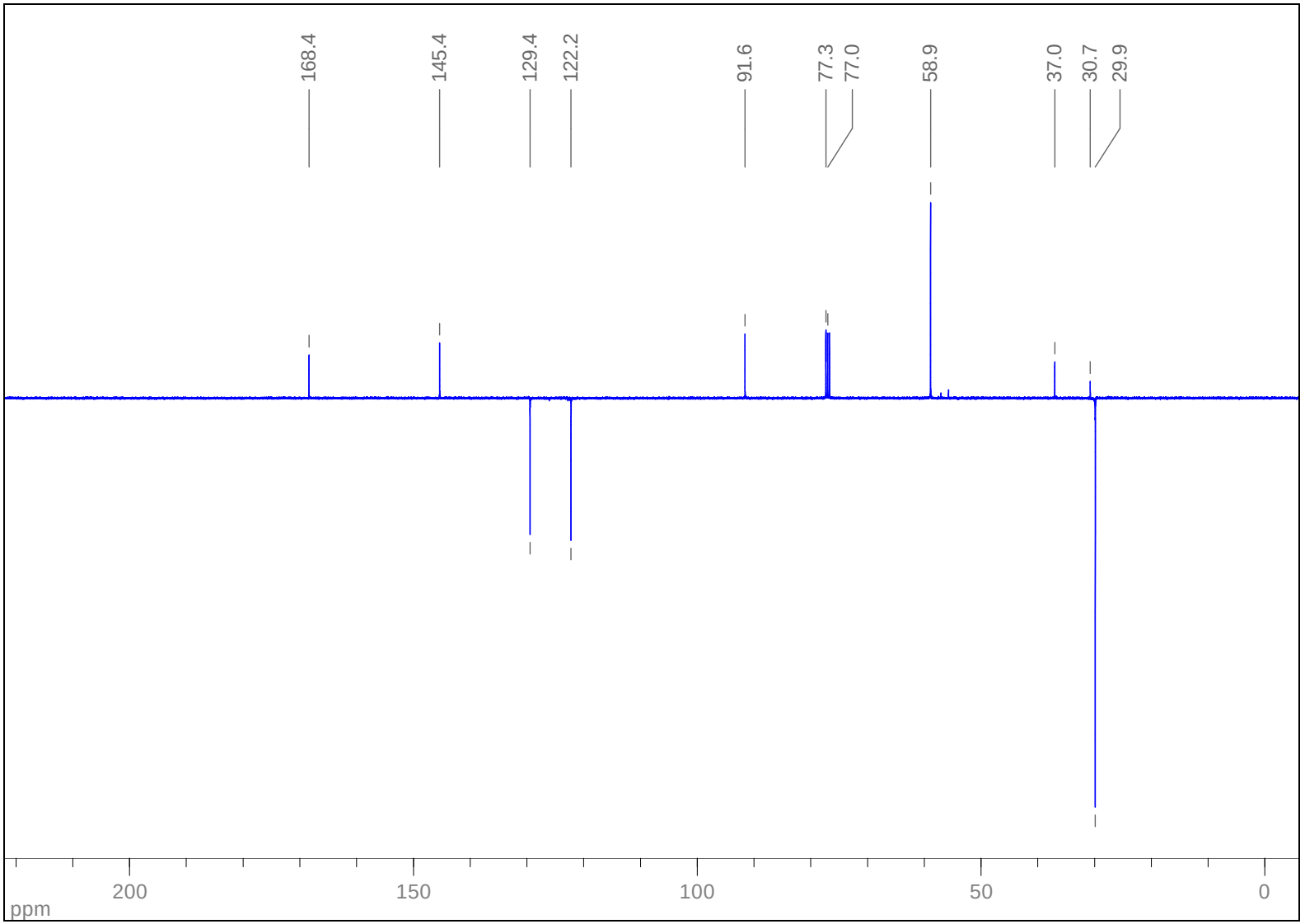

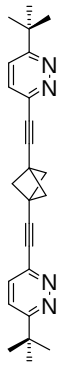

^{1}H – ^{1}H COSY ($CDCl_3$): 1,3-Bis((6-*tert*-butylpyridazin-3-yl)ethynyl)bicyclo[1.1.1]pentane (**2**)

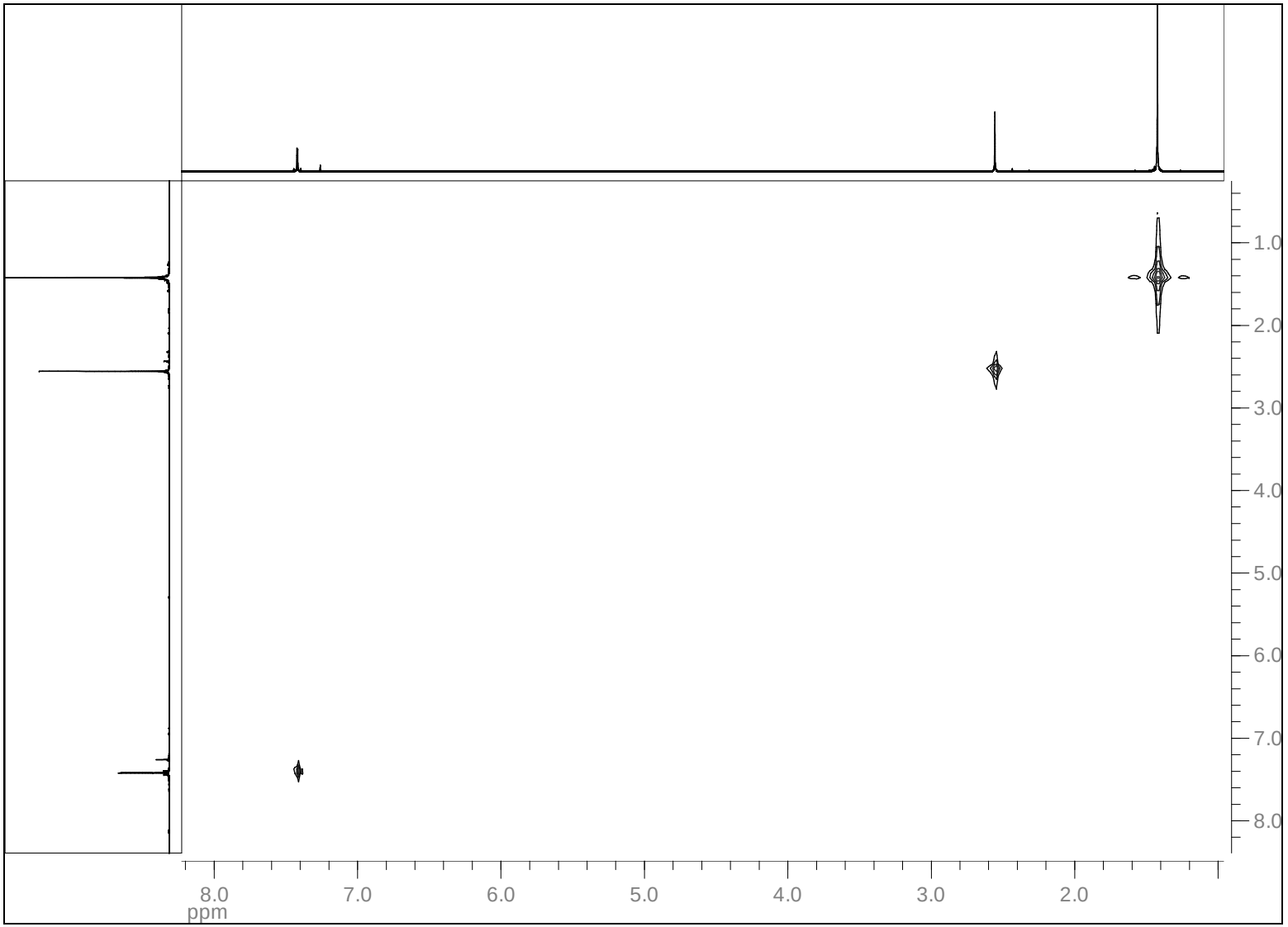

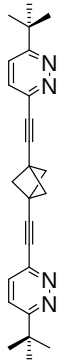

HSQC ($CDCl_3$): 1,3-Bis((6-*tert*-butylpyridazin-3-yl)ethynyl)bicyclo[1.1.1]pentane (**2**)

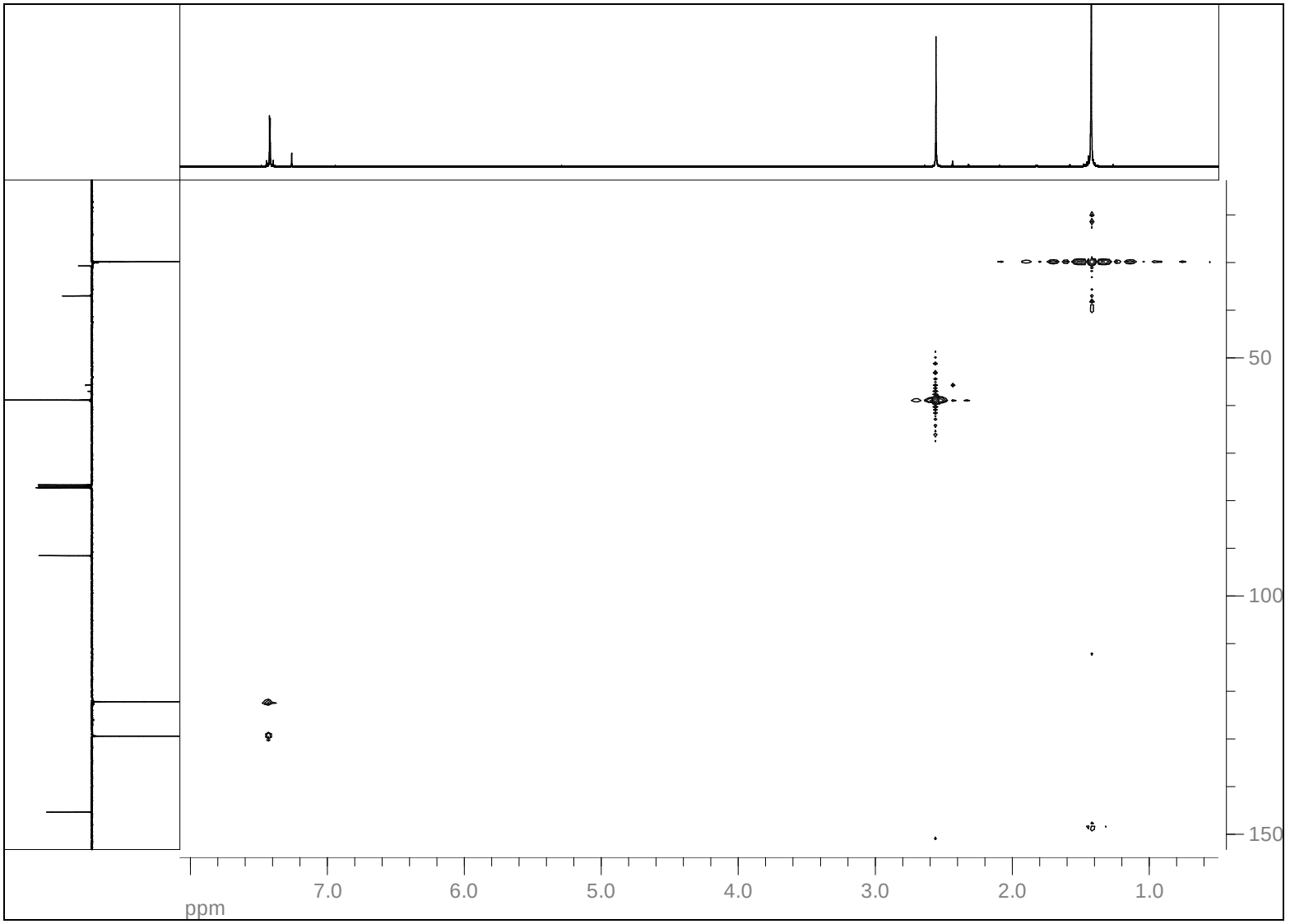

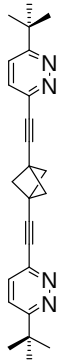

HMBC ($CDCl_3$): 1,3-Bis((6-*tert*-butylpyridazin-3-yl)ethynyl)bicyclo[1.1.1]pentane (**2**)

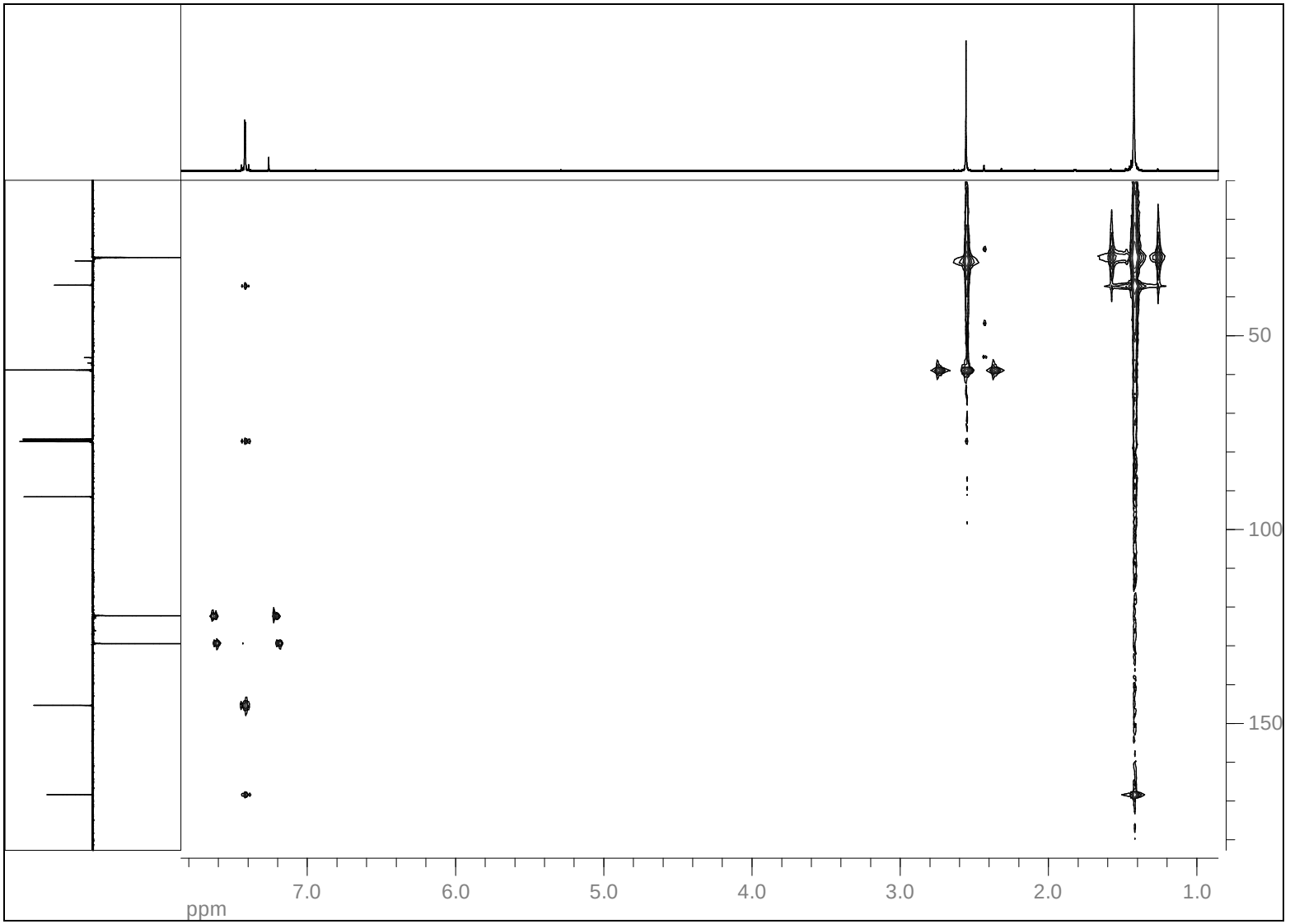

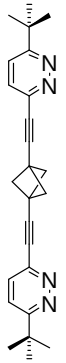

^{1}H NMR (400 MHz, $CDCl_3$): 1,3-Bis((6-(3,3-dimethylbut-1-ynyl)pyridazin-3-yl)ethynyl)bicyclo[1.1.1]pentane (**3**)

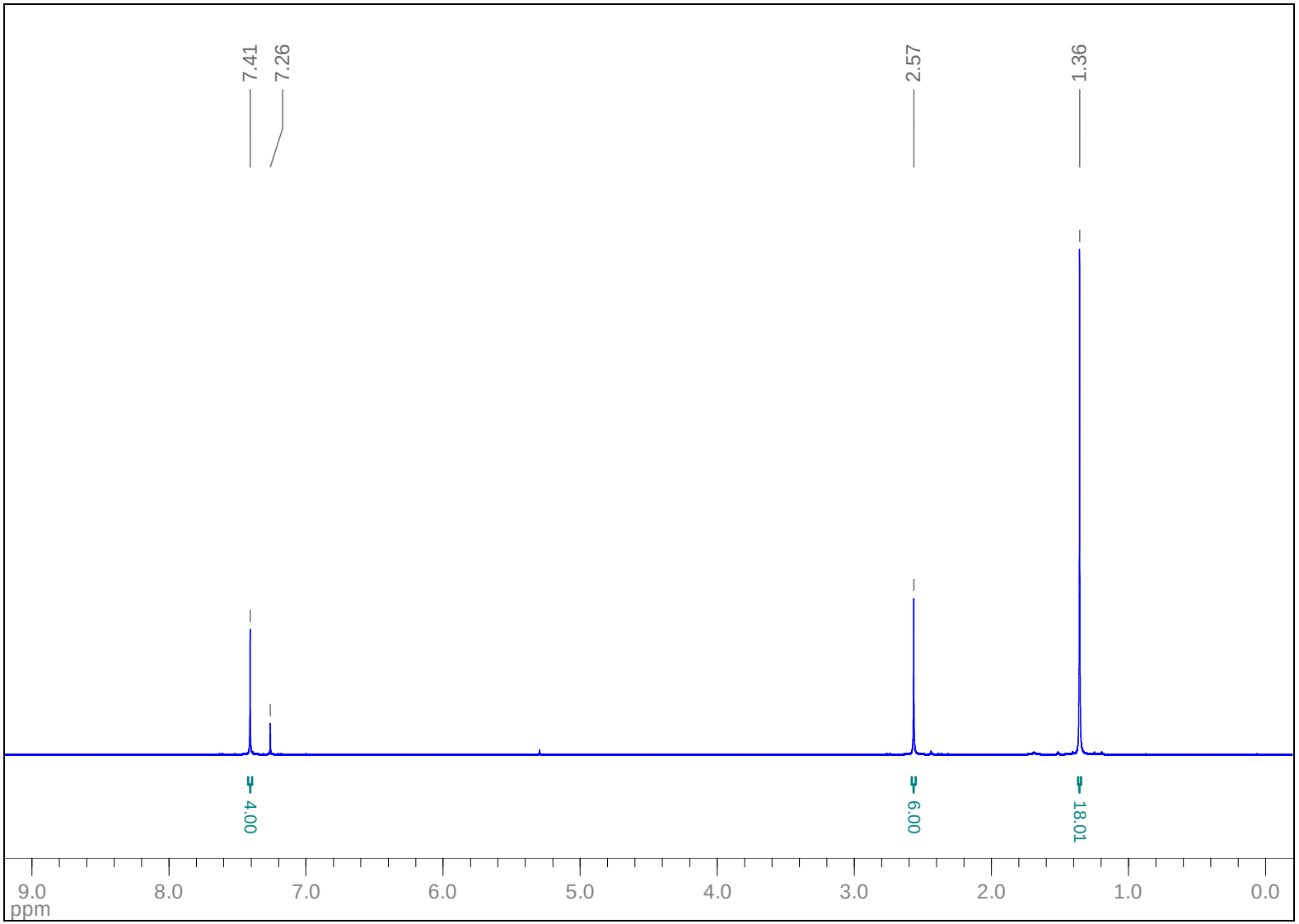

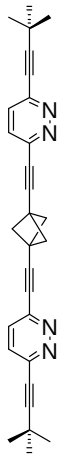

^{13}C {^{1}H} NMR (100 MHz, $CDCl_3$): 1,3-Bis((6-(3,3-dimethylbut-1-ynyl)pyridazin-3-yl)ethynyl)bicyclo[1.1.1]pentane (**3**)

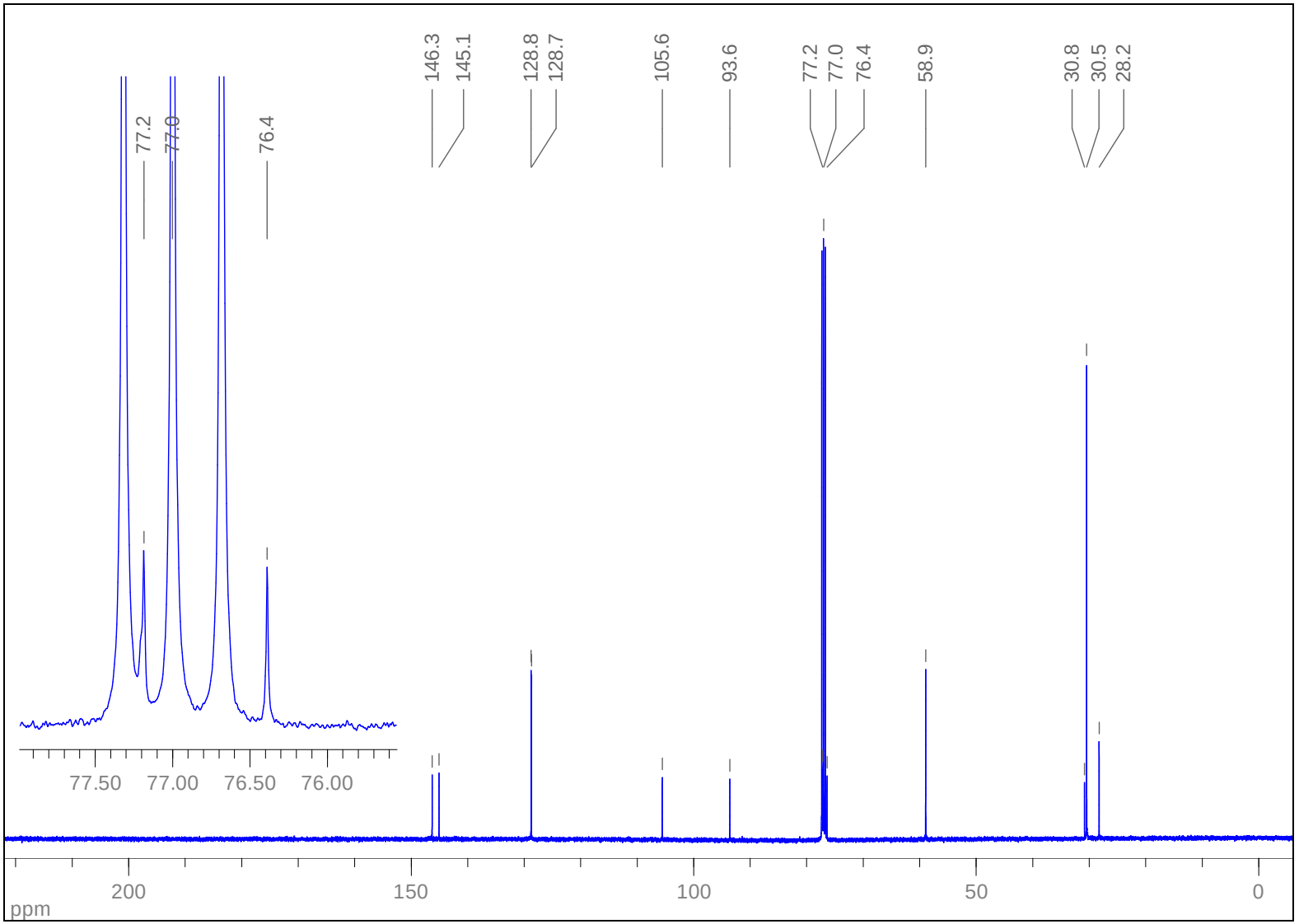

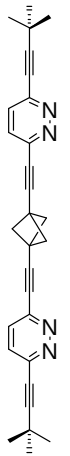

^{13}C APT NMR (100 MHz, $CDCl_3$): 1,3-Bis((6-(3,3-dimethylbut-1-ynyl)pyridazin-3-yl)ethynyl)bicyclo[1.1.1]pentane (**3**)

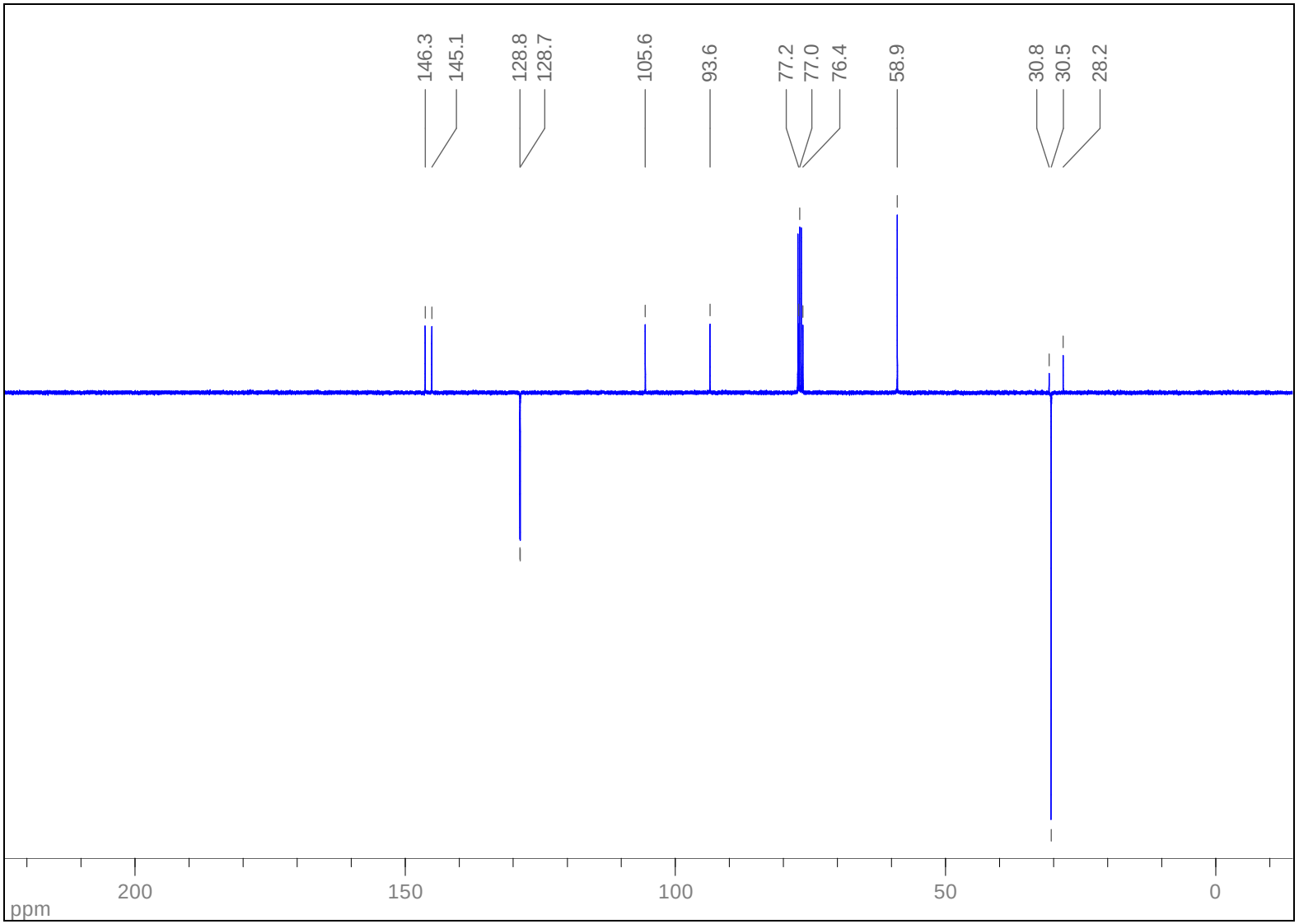

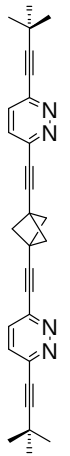

^{1}H – ^{1}H COSY ($CDCl_3$): 1,3-Bis((6-(3,3-dimethylbut-1-ynyl)pyridazin-3-yl)ethynyl)bicyclo[1.1.1]pentane (**3**)

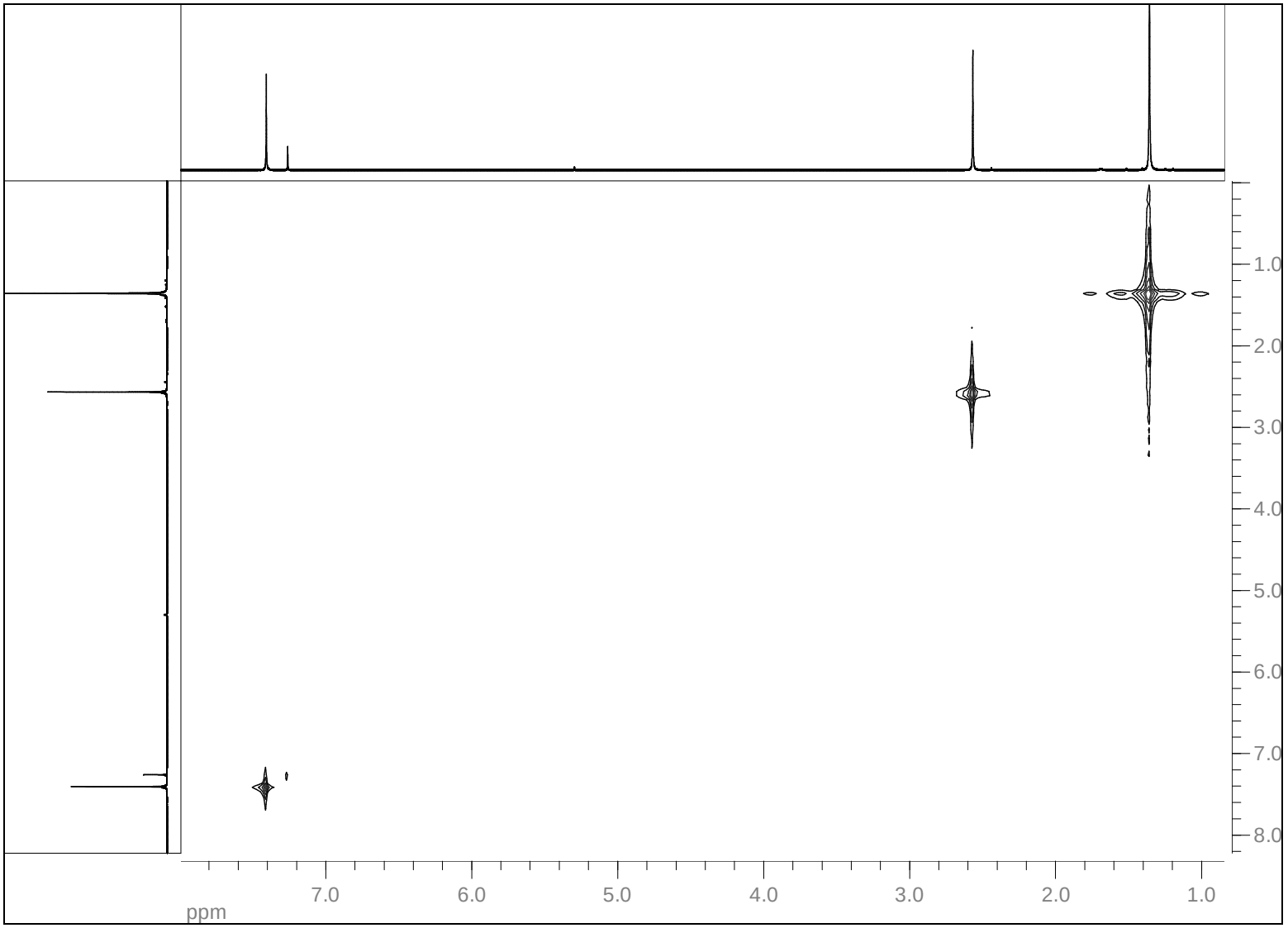

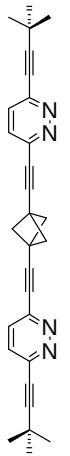

HSQC ($CDCl_3$): 1,3-Bis((6-(3,3-dimethylbut-1-ynyl)pyridazin-3-yl)ethynyl)bicyclo[1.1.1]pentane (**3**)

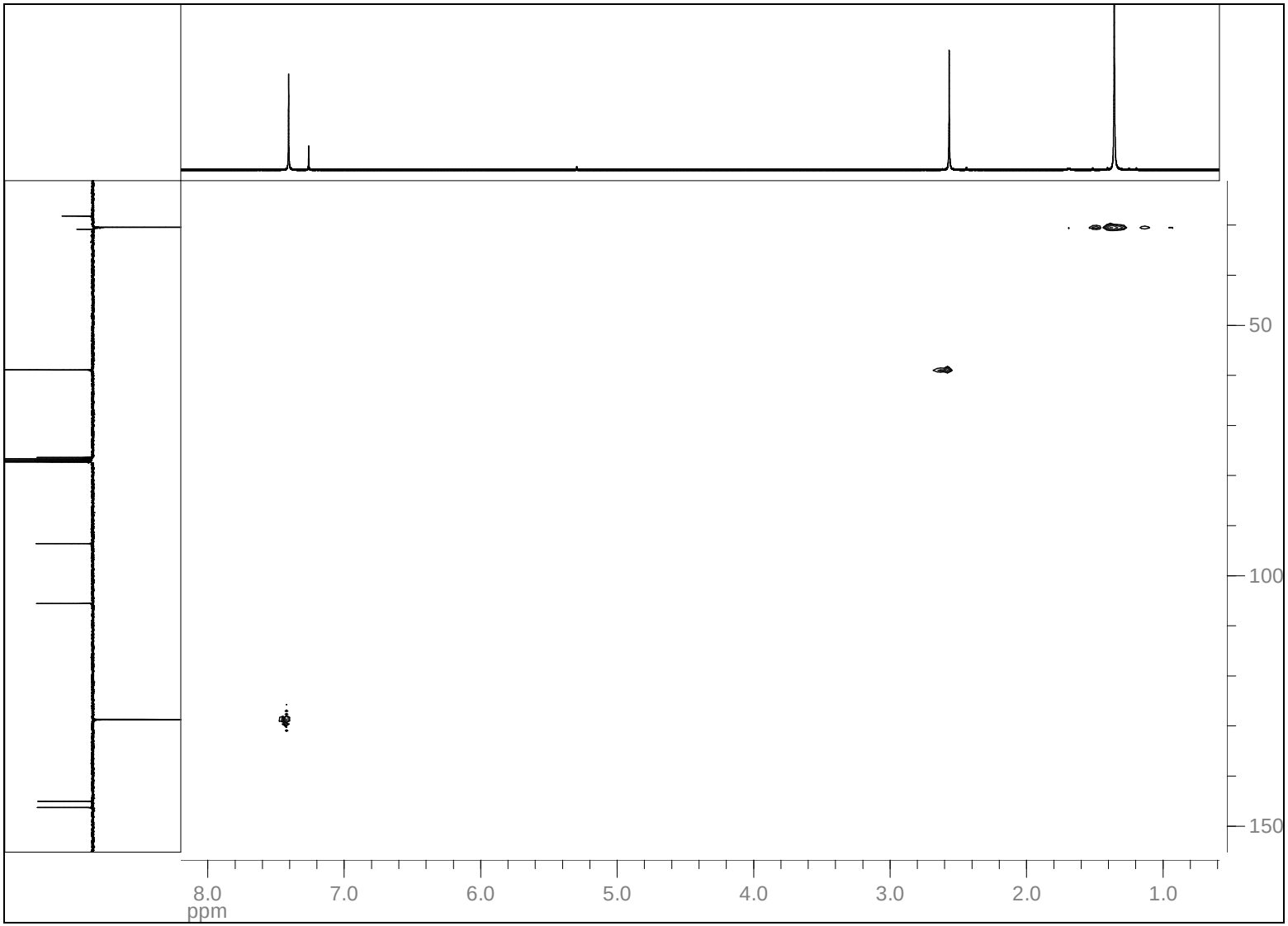

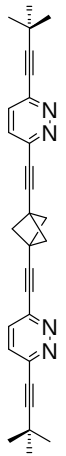

HMBC ($CDCl_3$): 1,3-Bis((6-(3,3-dimethylbut-1-ynyl)pyridazin-3-yl)ethynyl)bicyclo[1.1.1]pentane (**3**)

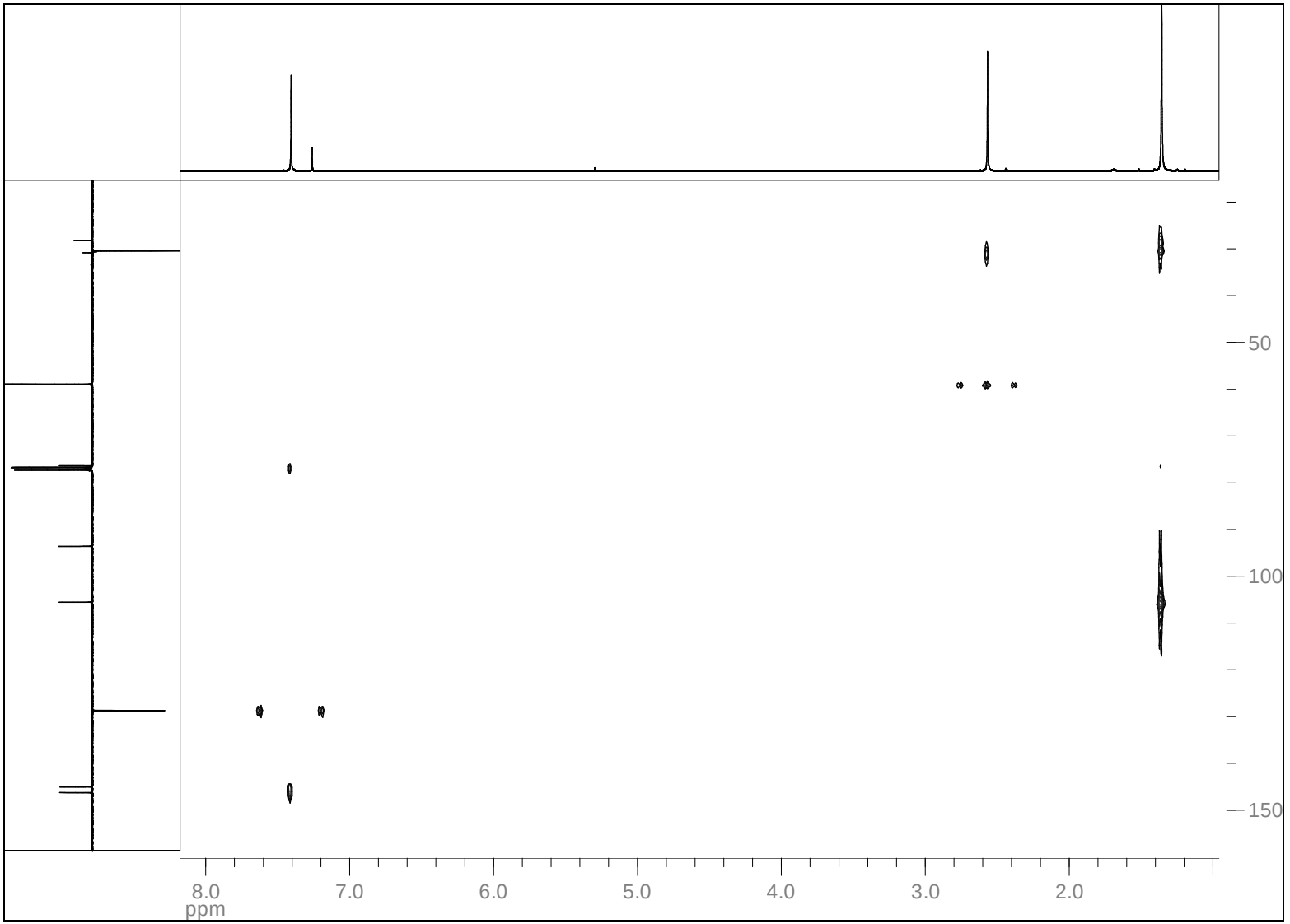

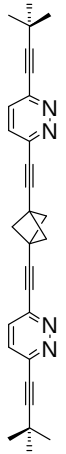

^{1}H NMR (400 MHz, $CDCl_3$): 1,3-Bis((6-*tert*-butylpyridazin-3-yl)buta-1,3-diynyl)bicyclo[1.1.1]pentane (**4**)

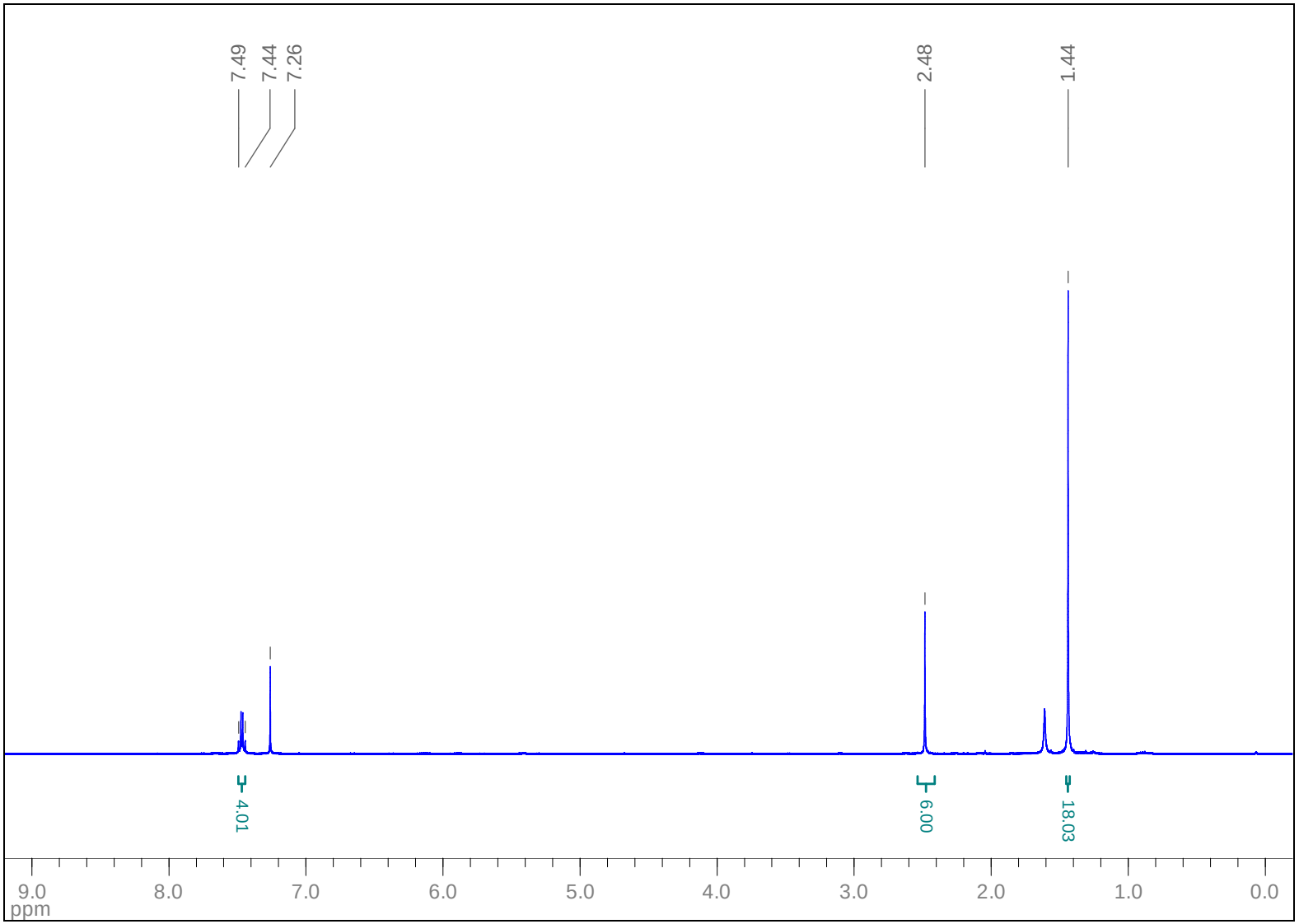

^{13}C {^{1}H} NMR (100 MHz, $CDCl_3$): 1,3-Bis((6-*tert*-butylpyridazin-3-yl)buta-1,3-diynyl)bicyclo[1.1.1]pentane (**4**)

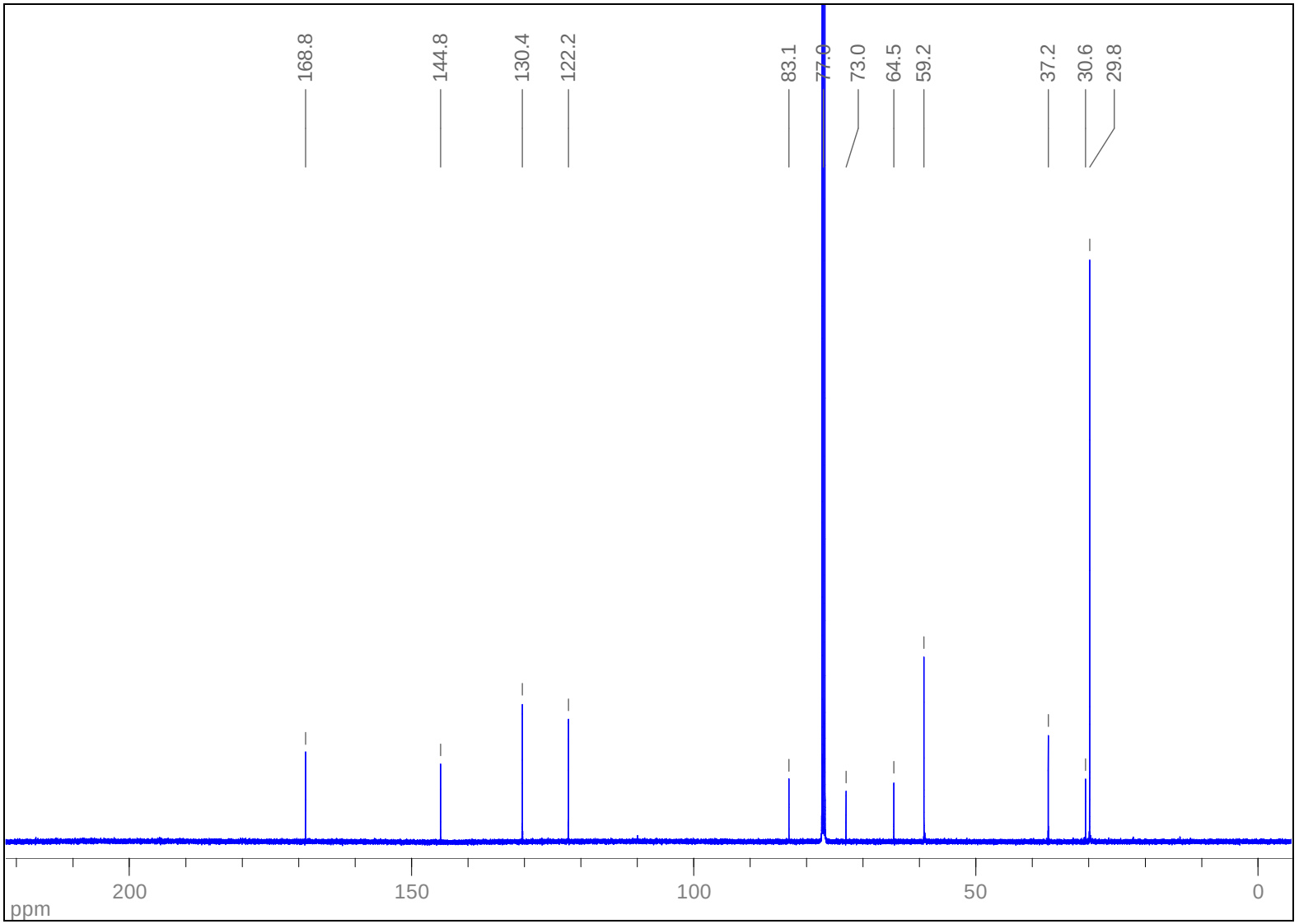

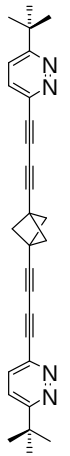

^{13}C APT NMR (100 MHz, $CDCl_3$): 1,3-Bis((6-*tert*-butylpyridazin-3-yl)buta-1,3-diynyl)bicyclo[1.1.1]pentane (**4**)

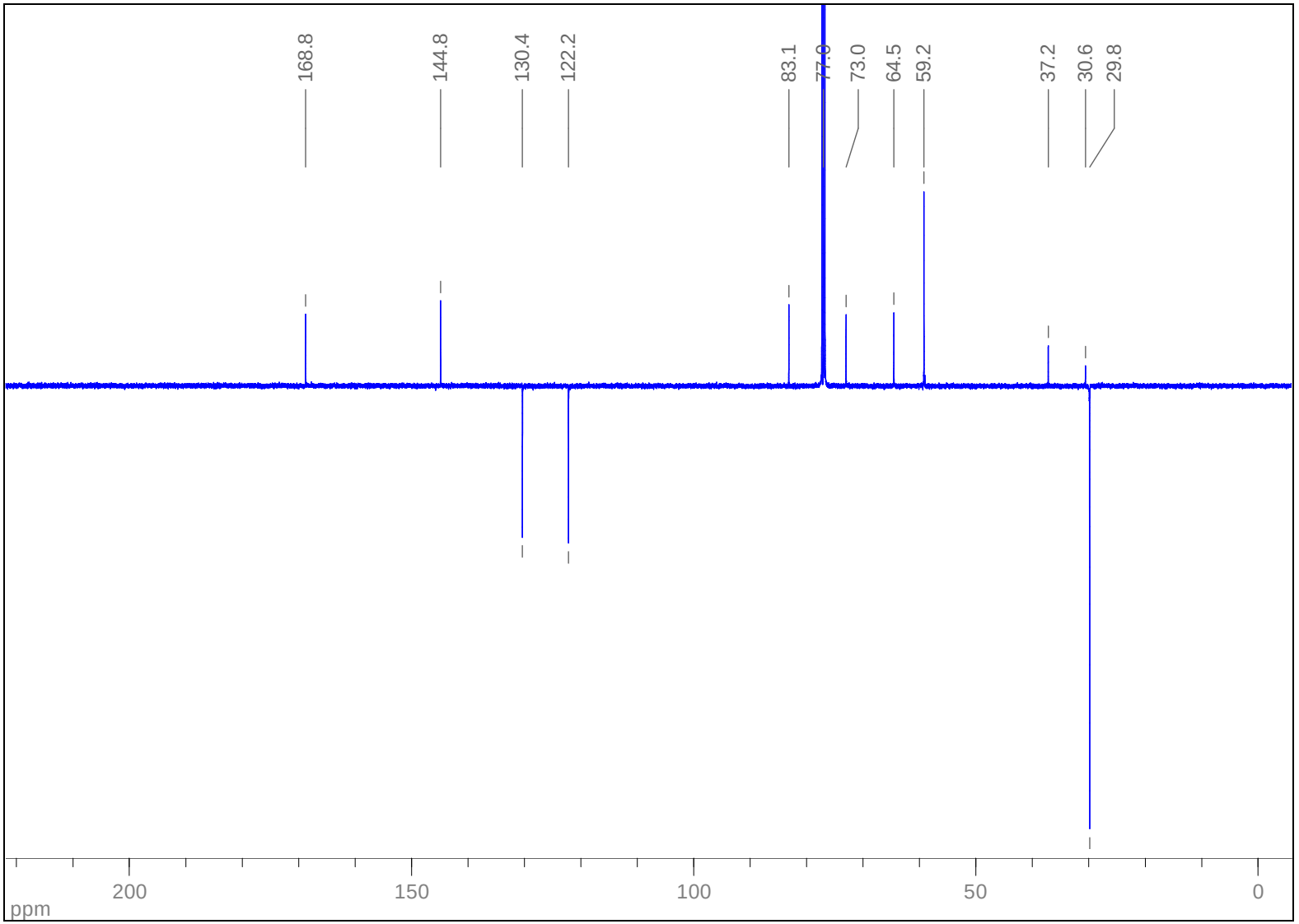

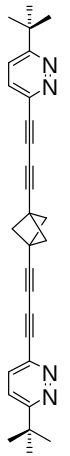

HSQC ($CDCl_3$): 1,3-Bis((6-*tert*-butylpyridazin-3-yl)buta-1,3-diynyl)bicyclo[1.1.1]pentane (**4**)

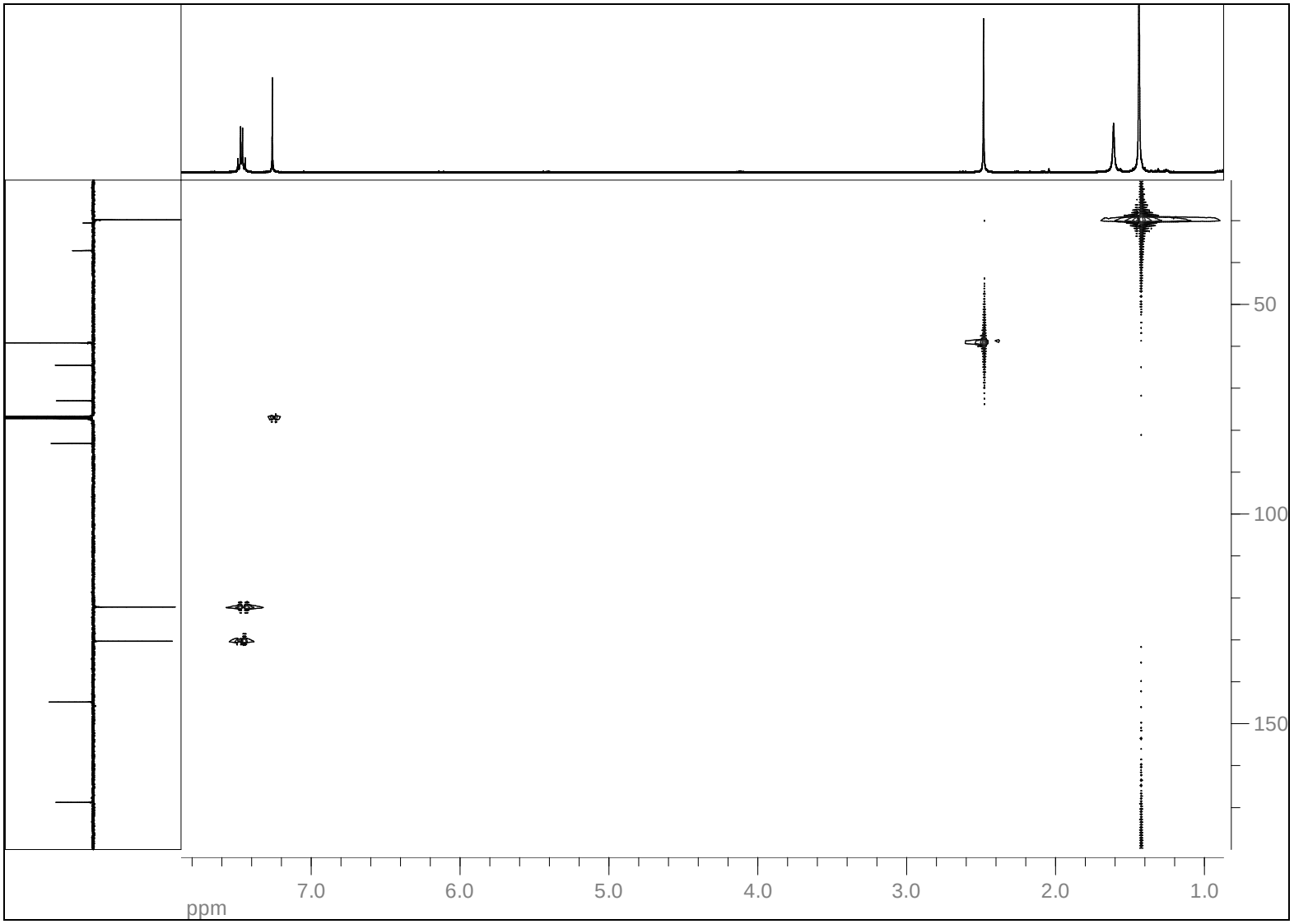

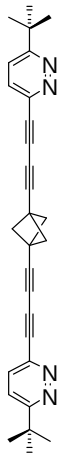

HMBC ($CDCl_3$): 1,3-Bis((6-*tert*-butylpyridazin-3-yl)buta-1,3-diynyl)bicyclo[1.1.1]pentane (**4**)

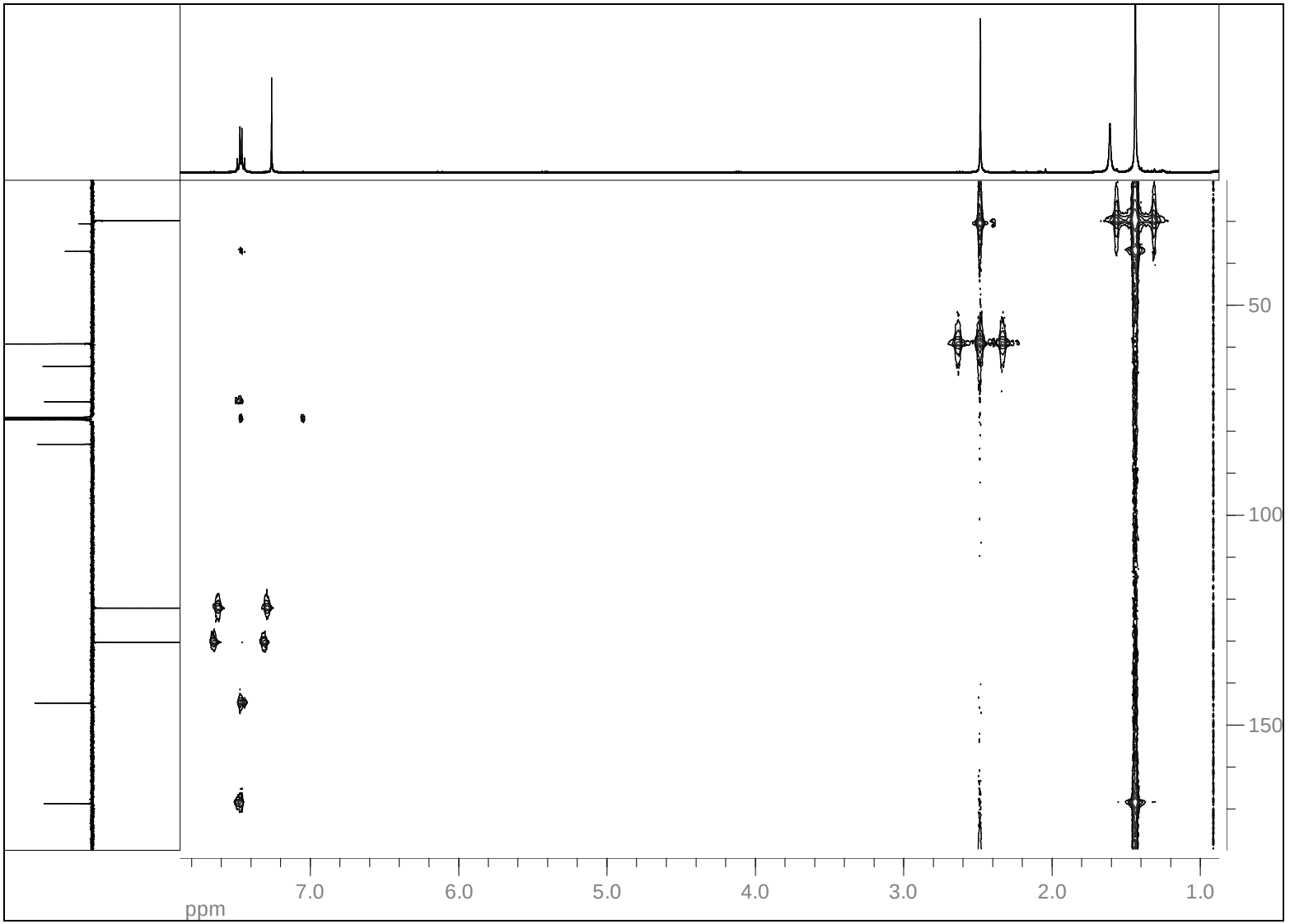

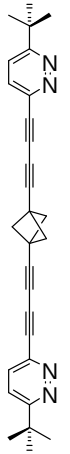

^{1}H NMR (500 MHz, $CDCl_3$): 1,3-Bis((6-(3,3-dimethylbut-1-ynyl)pyridazin-3-yl)buta-1,3-diynyl)bicyclo[1.1.1]pentane (**5**)

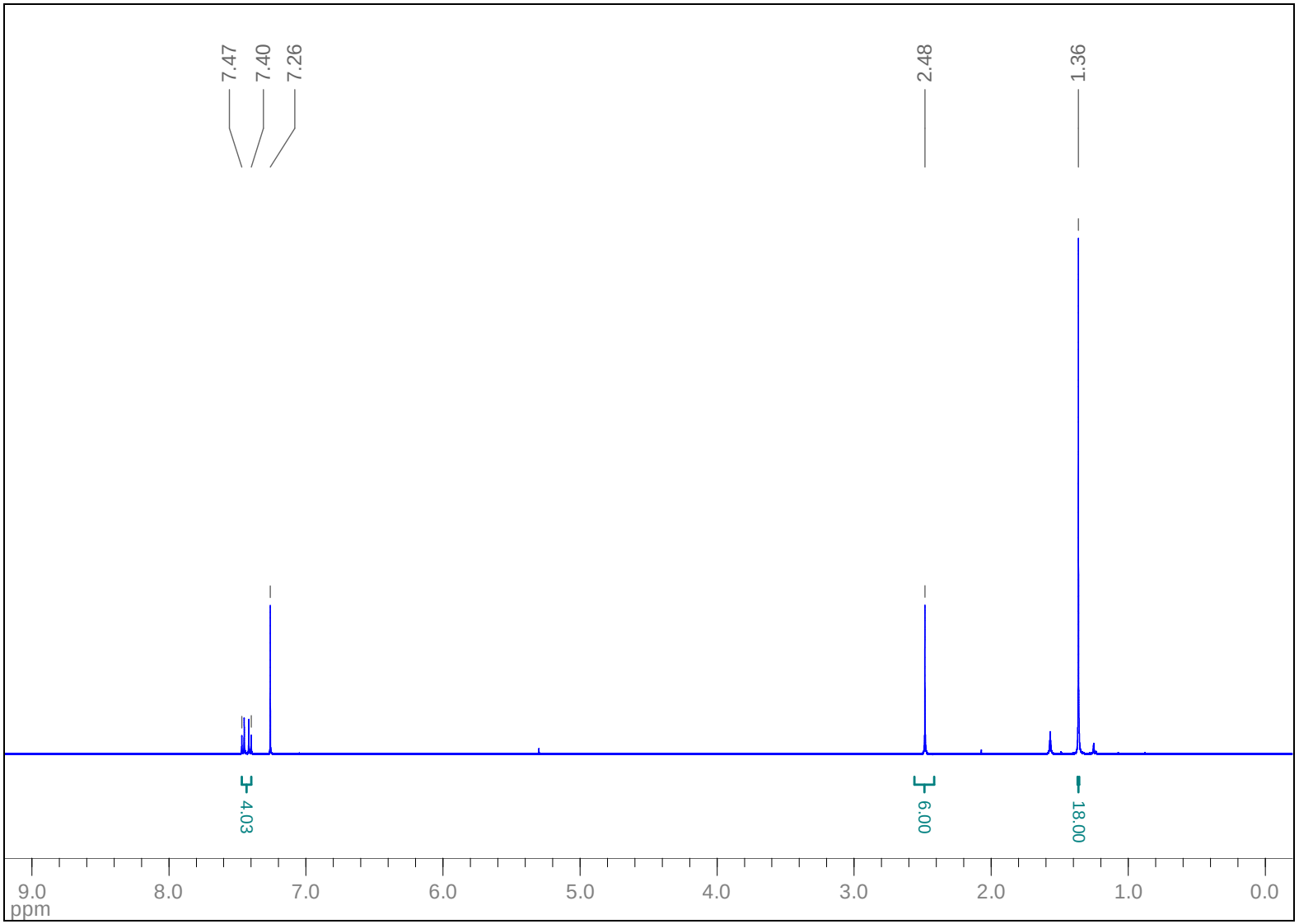

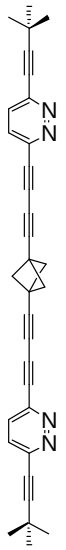

^{13}C {^{1}H} NMR (125 MHz, $CDCl_3$): 1,3-Bis((6-(3,3-dimethylbut-1-ynyl)pyridazin-3-yl)buta-1,3-diynyl)bicyclo[1.1.1]pentane (**5**)

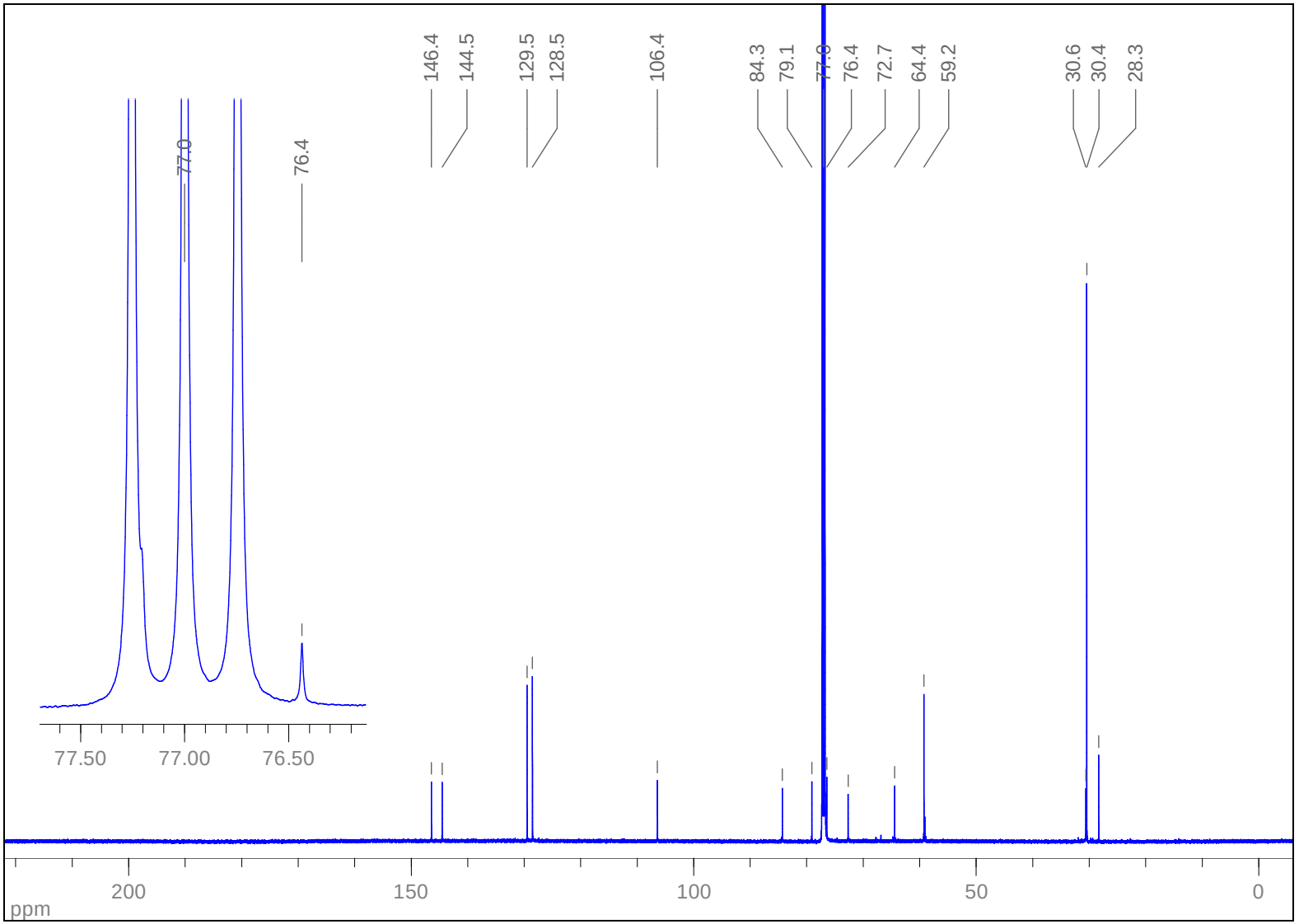

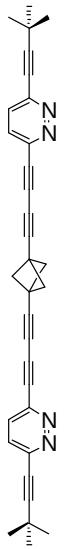

^{13}C APT NMR (125 MHz, $CDCl_3$): 1,3-Bis((6-(3,3-dimethylbut-1-ynyl)pyridazin-3-yl)buta-1,3-diynyl)bicyclo[1.1.1]pentane (**5**)

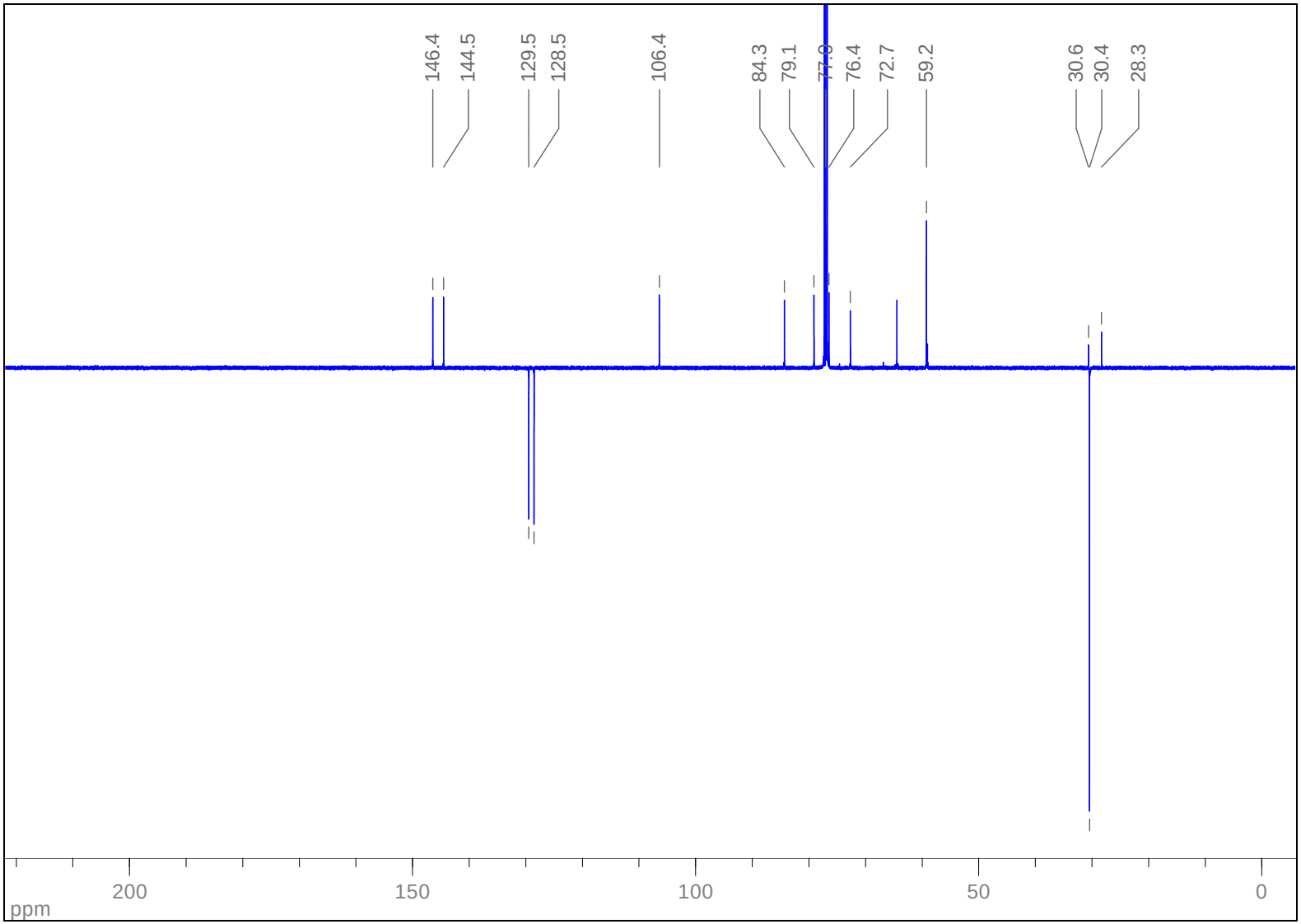

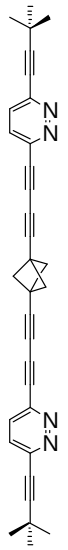

HSQC ($CDCl_3$): 1,3-Bis((6-(3,3-dimethylbut-1-ynyl)pyridazin-3-yl)buta-1,3-diynyl)bicyclo[1.1.1]pentane (**5**)

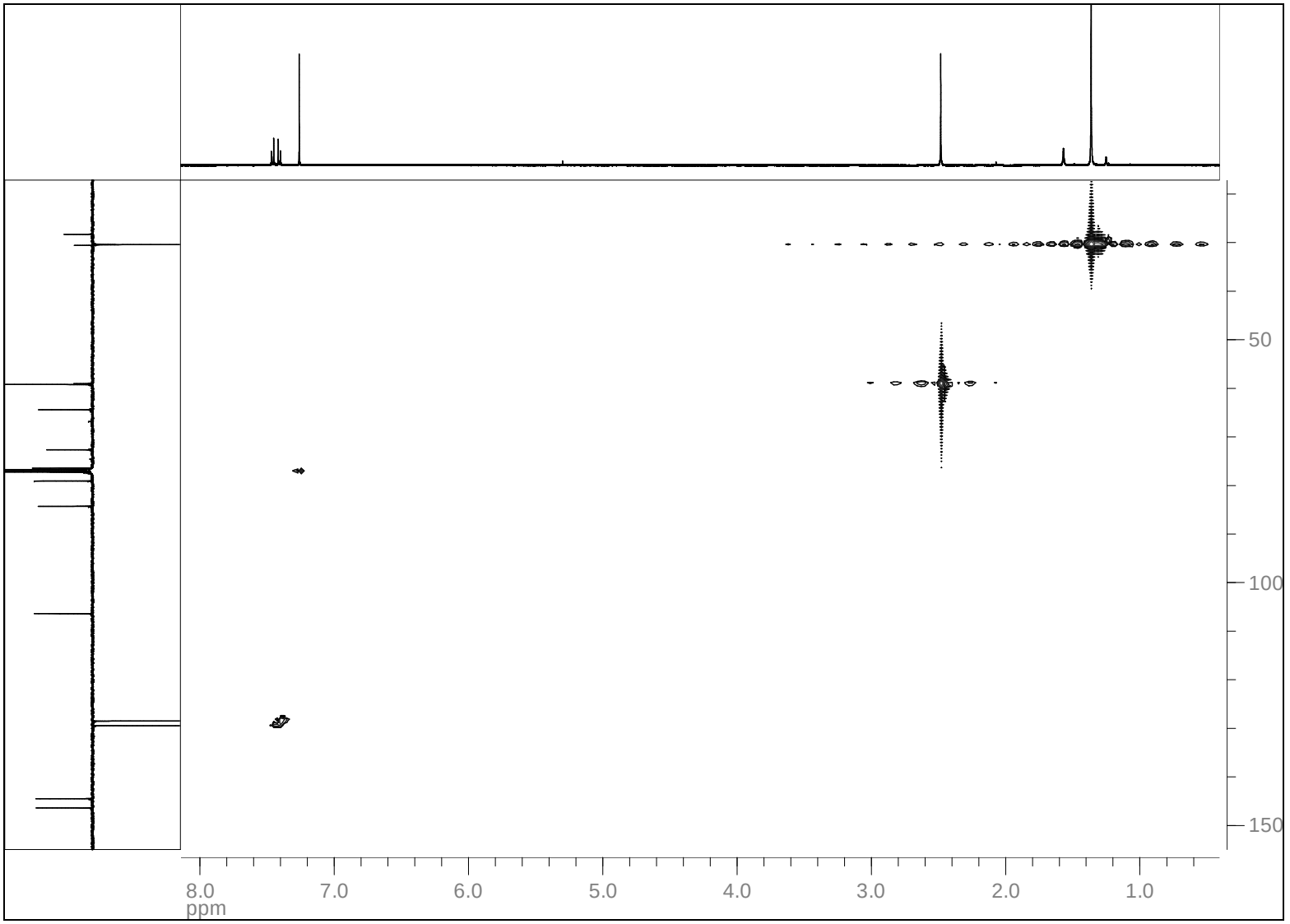

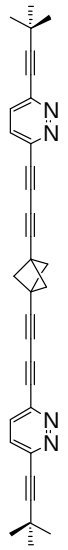

HMBC ($CDCl_3$): 1,3-Bis((6-(3,3-dimethylbut-1-ynyl)pyridazin-3-yl)buta-1,3-diynyl)bicyclo[1.1.1]pentane (**5**)

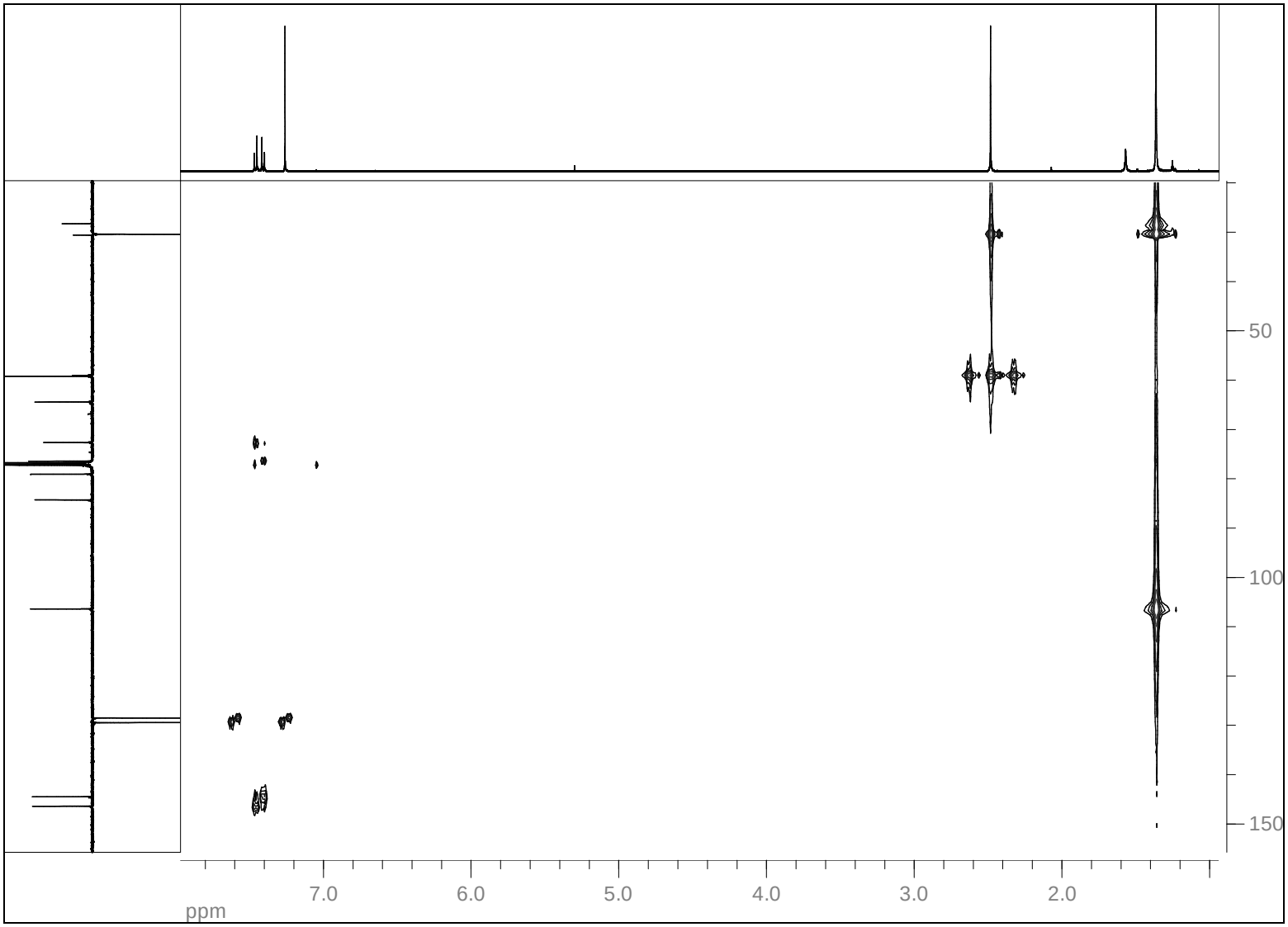

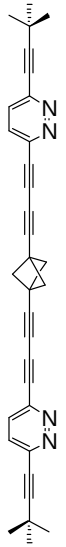

^{1}H NMR (400 MHz, $CDCl_3$): 3-*tert*-Butyl-6-chloropyridazine (**8**)

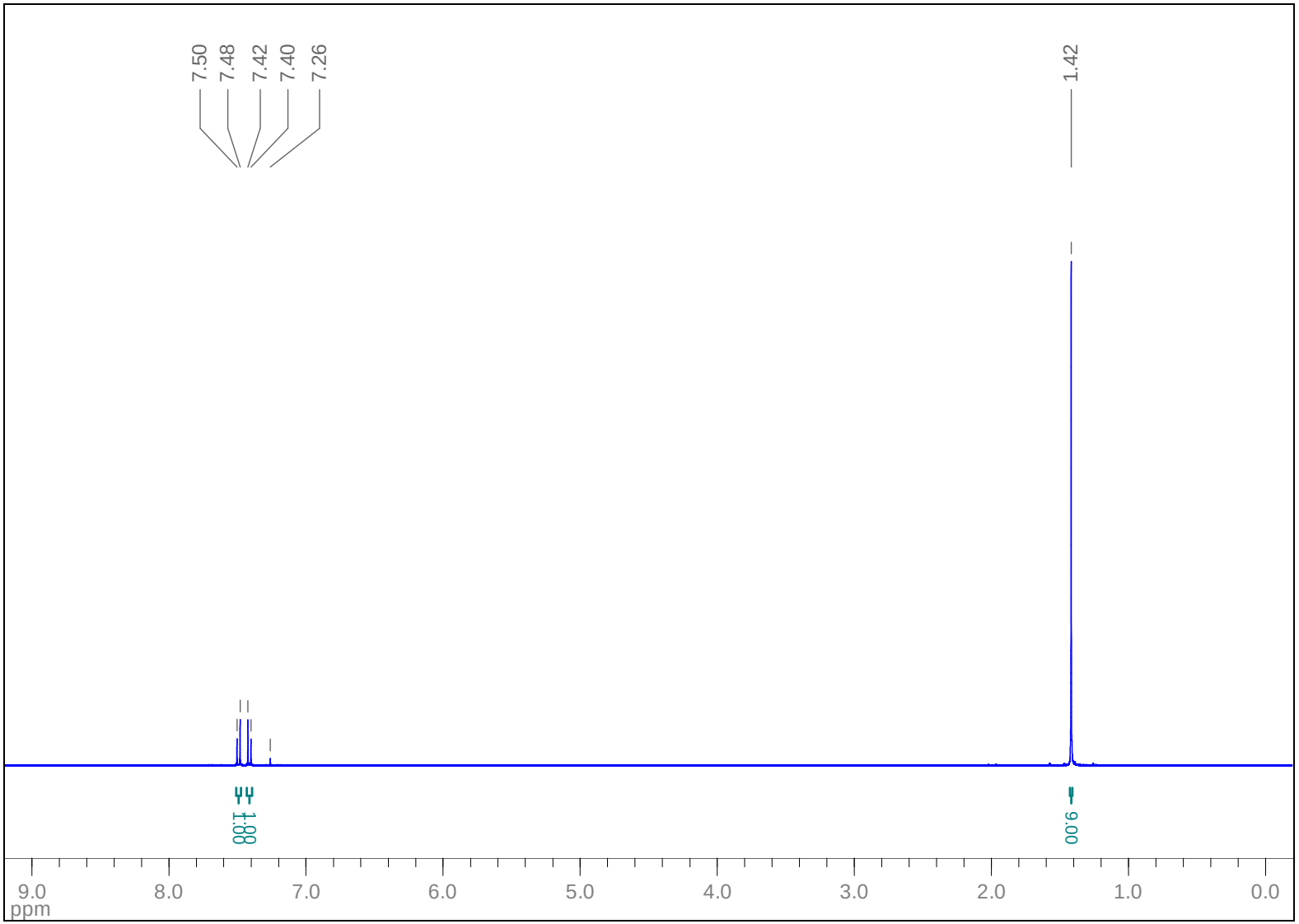

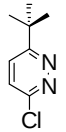

^{13}C {^{1}H} NMR (100 MHz, $CDCl_3$): 3-*tert*-Butyl-6-chloropyridazine (**8**)

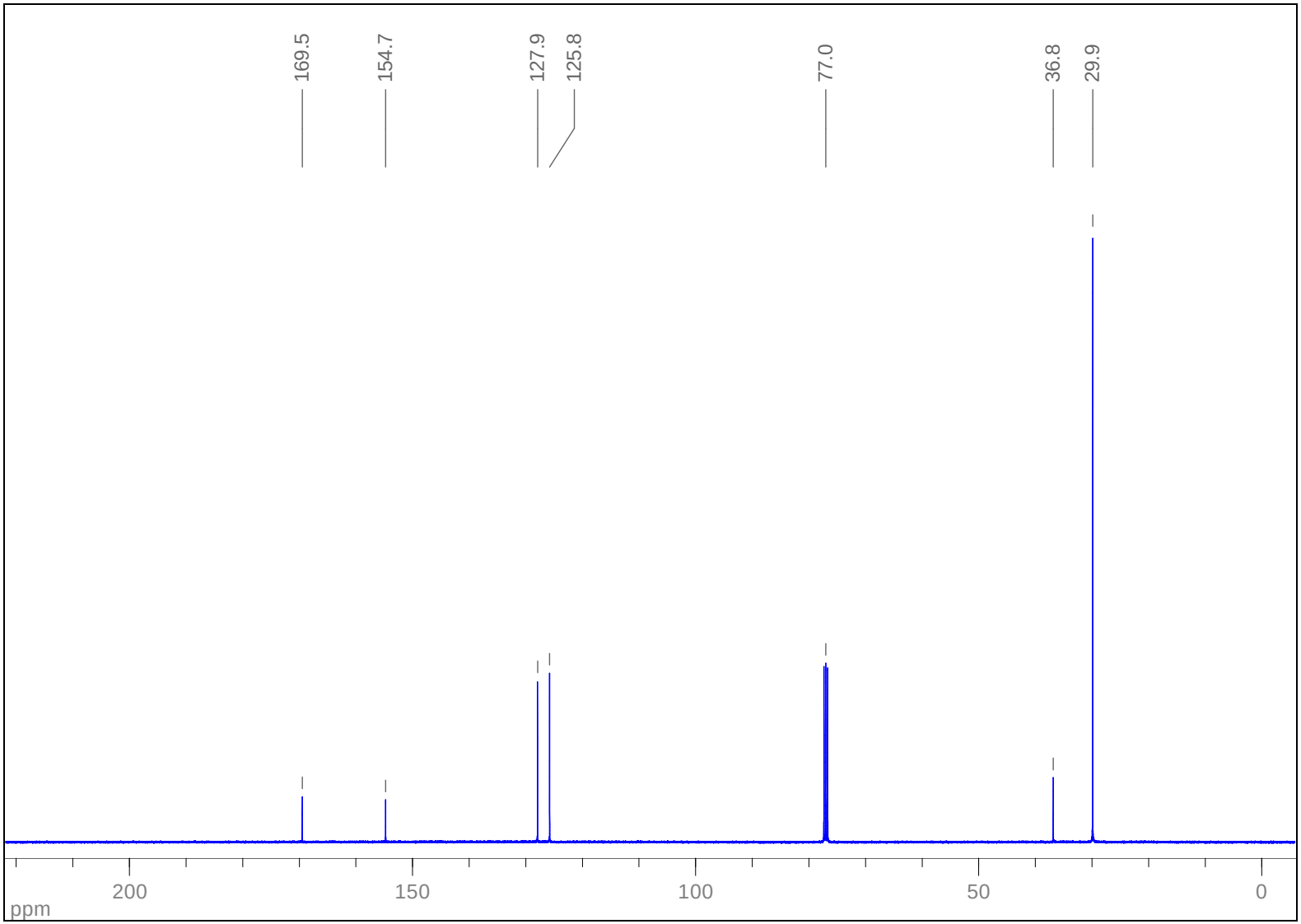

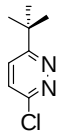

^{13}C APT NMR (100 MHz, $CDCl_3$): 3-*tert*-Butyl-6-chloropyridazine (**8**)

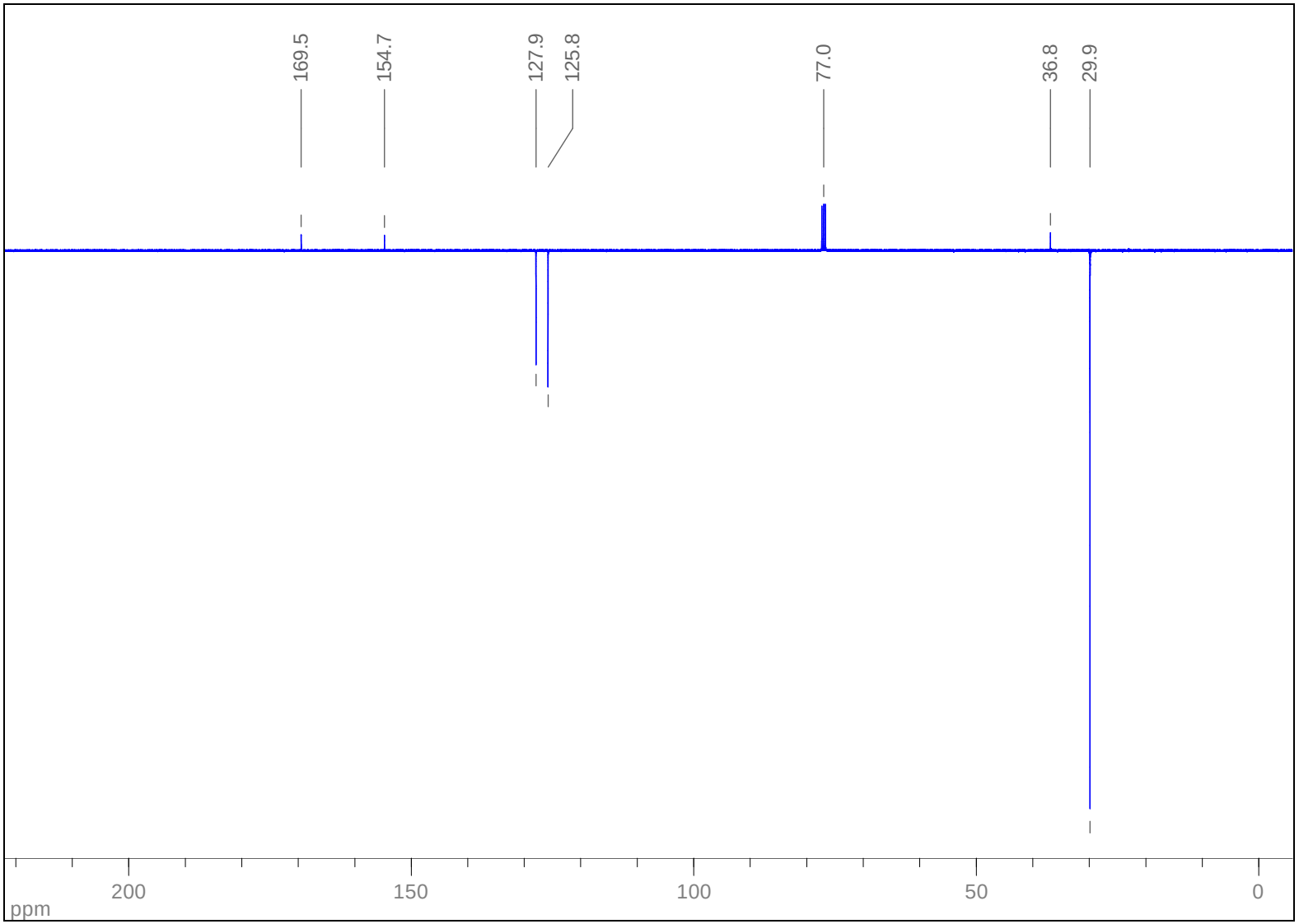

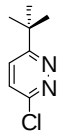

HSQC ($CDCl_3$): 3-*tert*-Butyl-6-chloropyridazine (**8**)

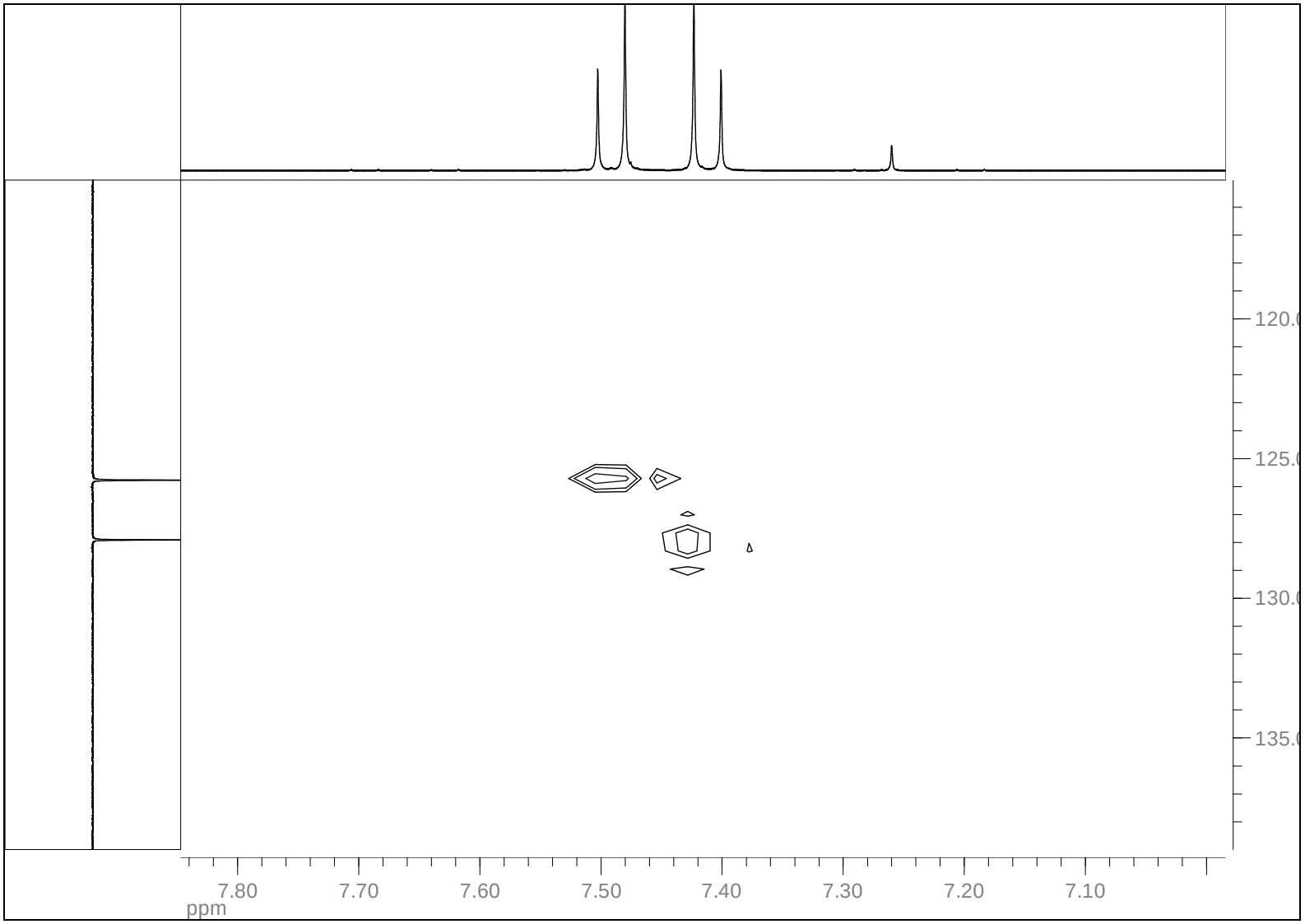

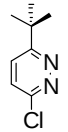

HMBC ($CDCl_3$): 3-*tert*-Butyl-6-chloropyridazine (**8**)

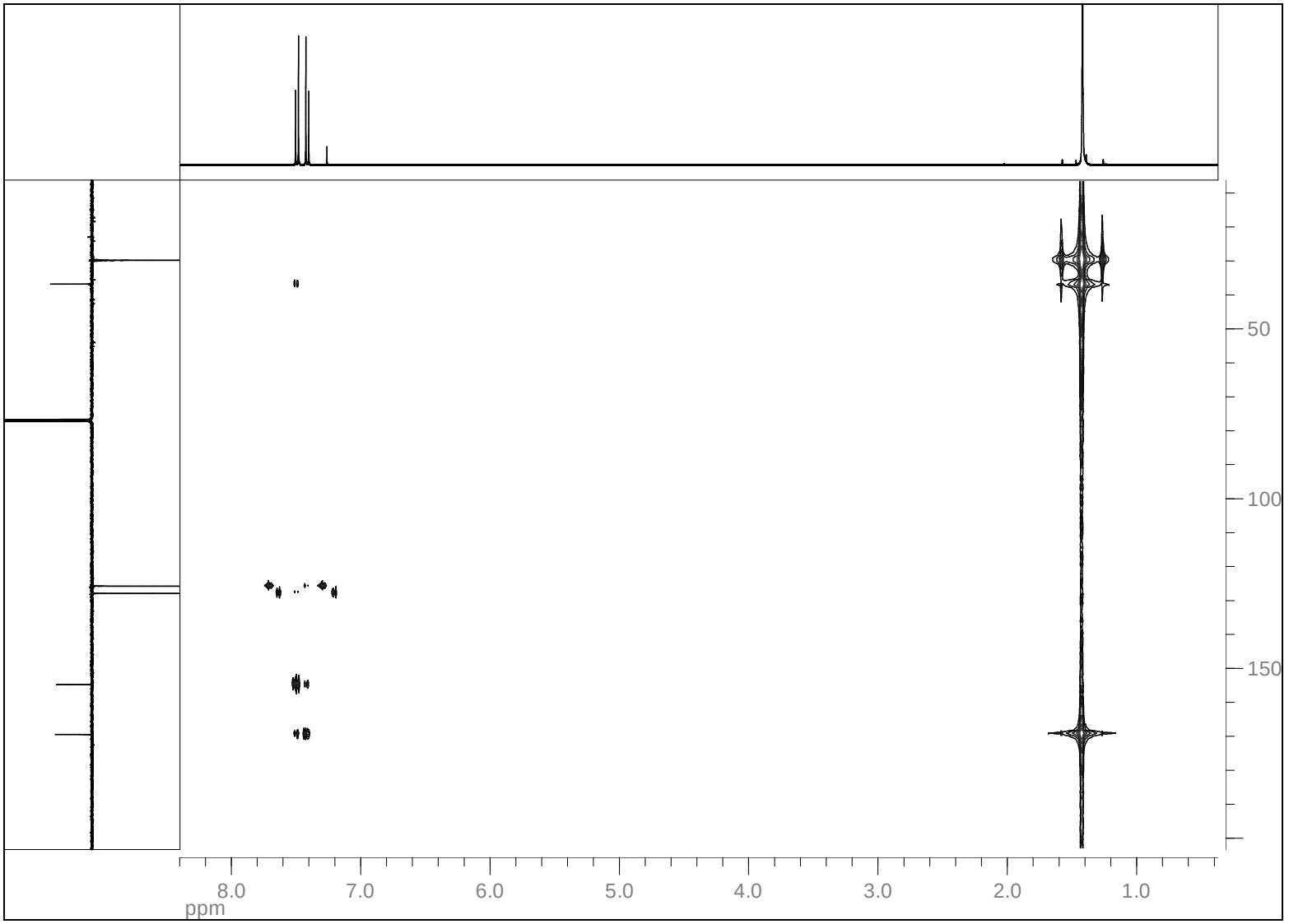

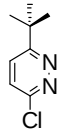

^{1}H NMR (400 MHz, $CDCl_3$): 3-*tert*-Butyl-6-iodopyridazine (**9**)

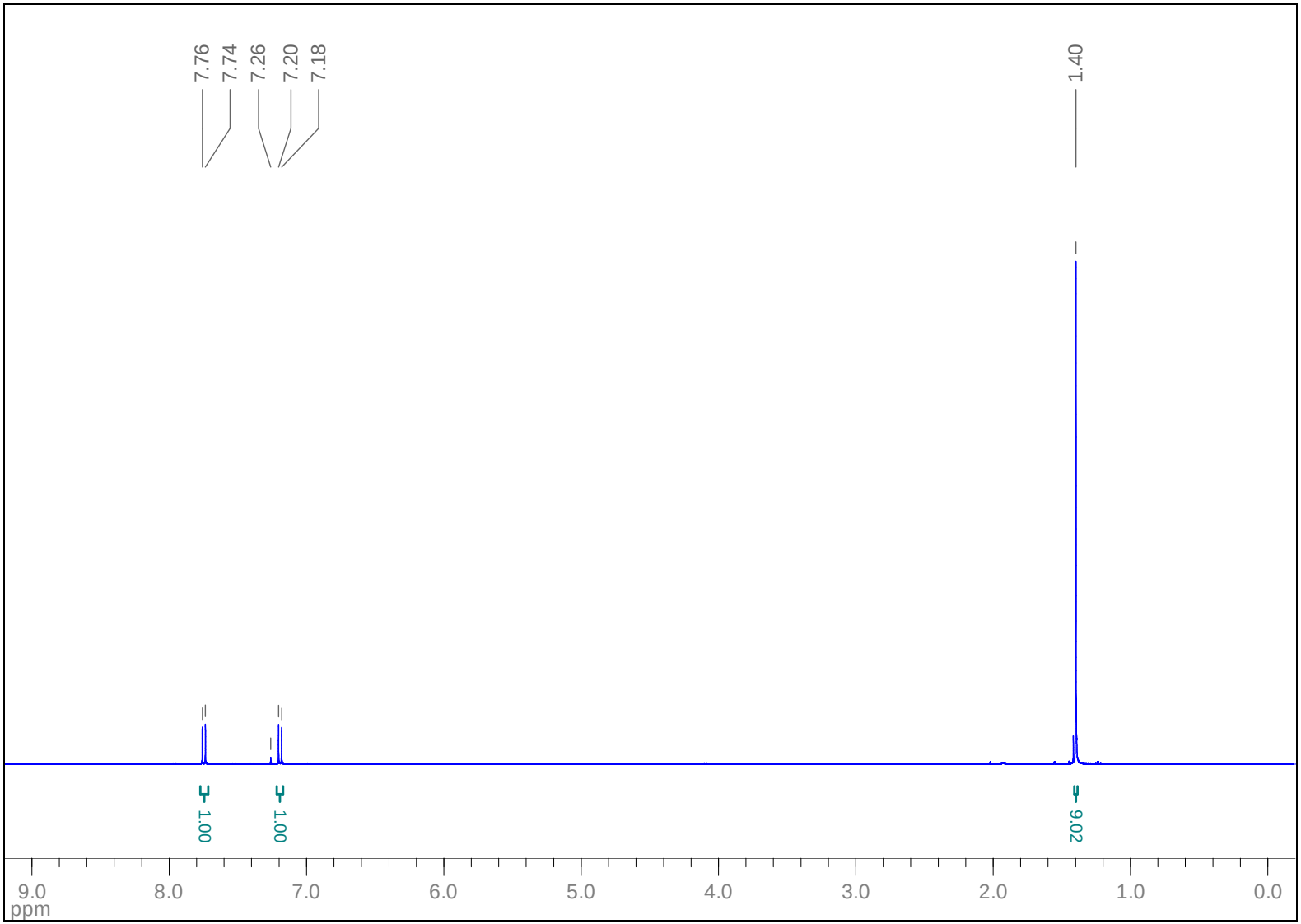

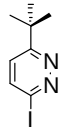

^{13}C {^{1}H} NMR (100 MHz, $CDCl_3$): 3-*tert*-Butyl-6-iodopyridazine (**9**)

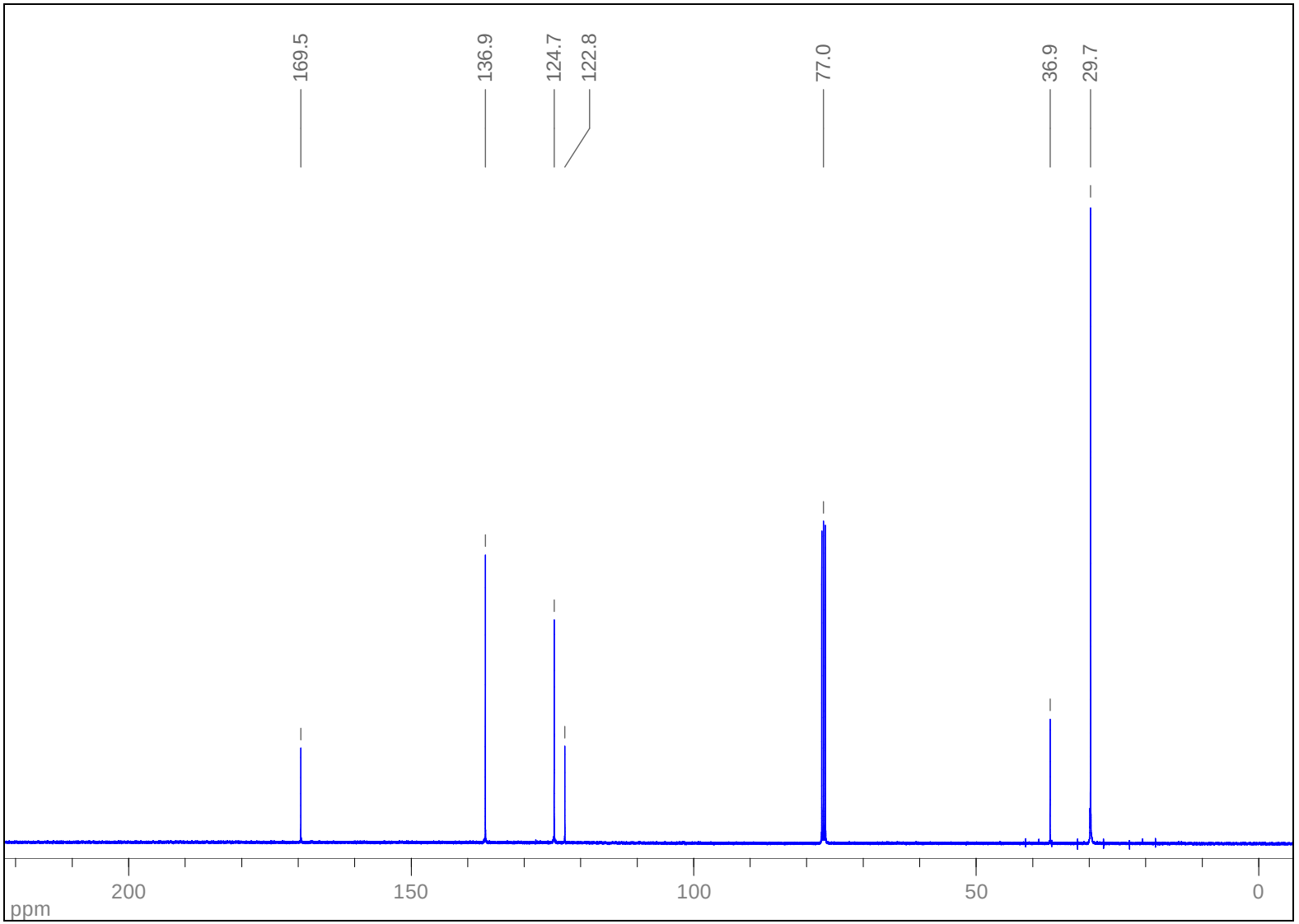

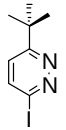

^{13}C APT NMR (100 MHz, $CDCl_3$): 3-*tert*-Butyl-6-iodopyridazine (**9**)

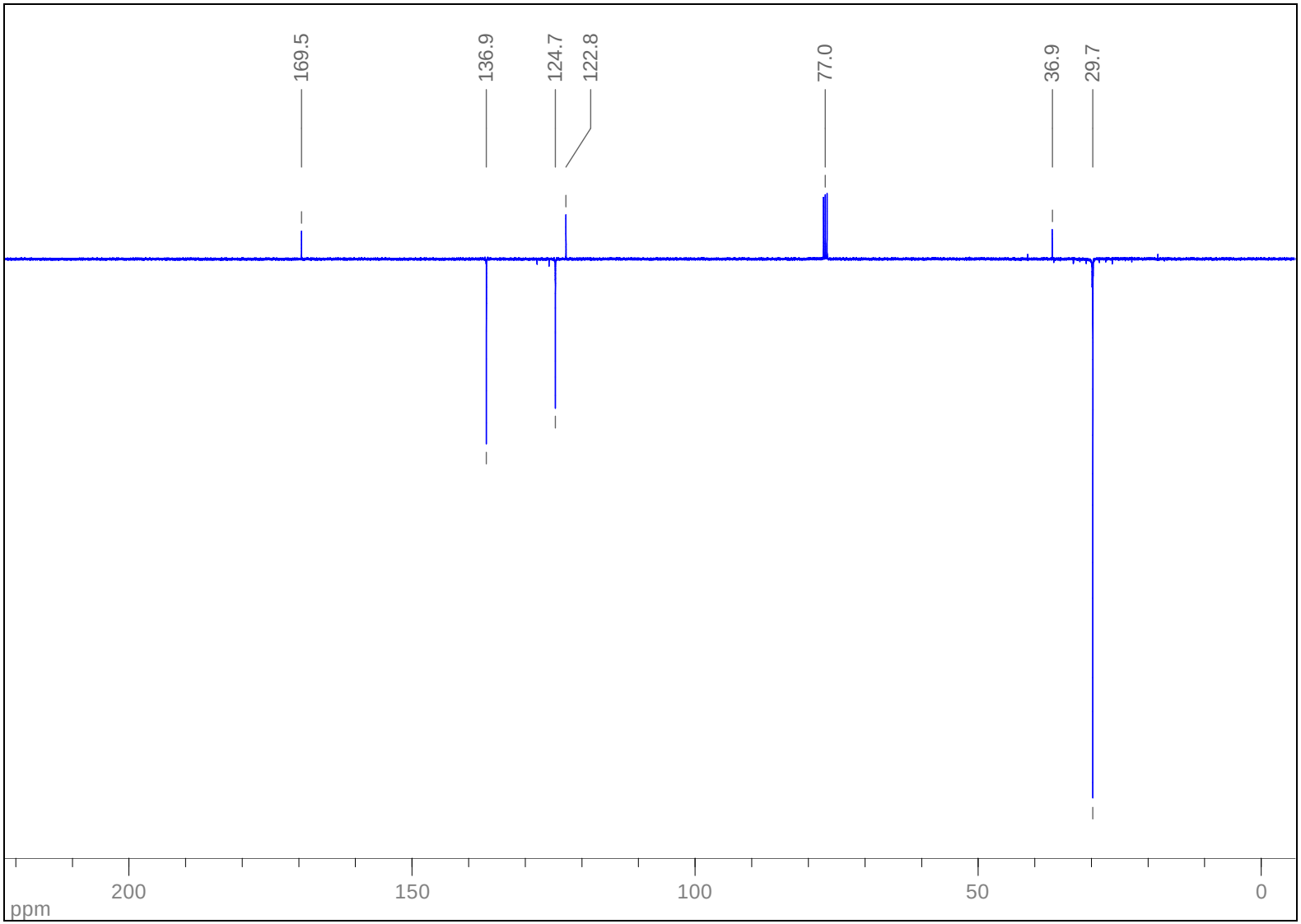

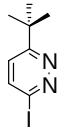

HSQC ($CDCl_3$): 3-*tert*-Butyl-6-iodopyridazine (**9**)

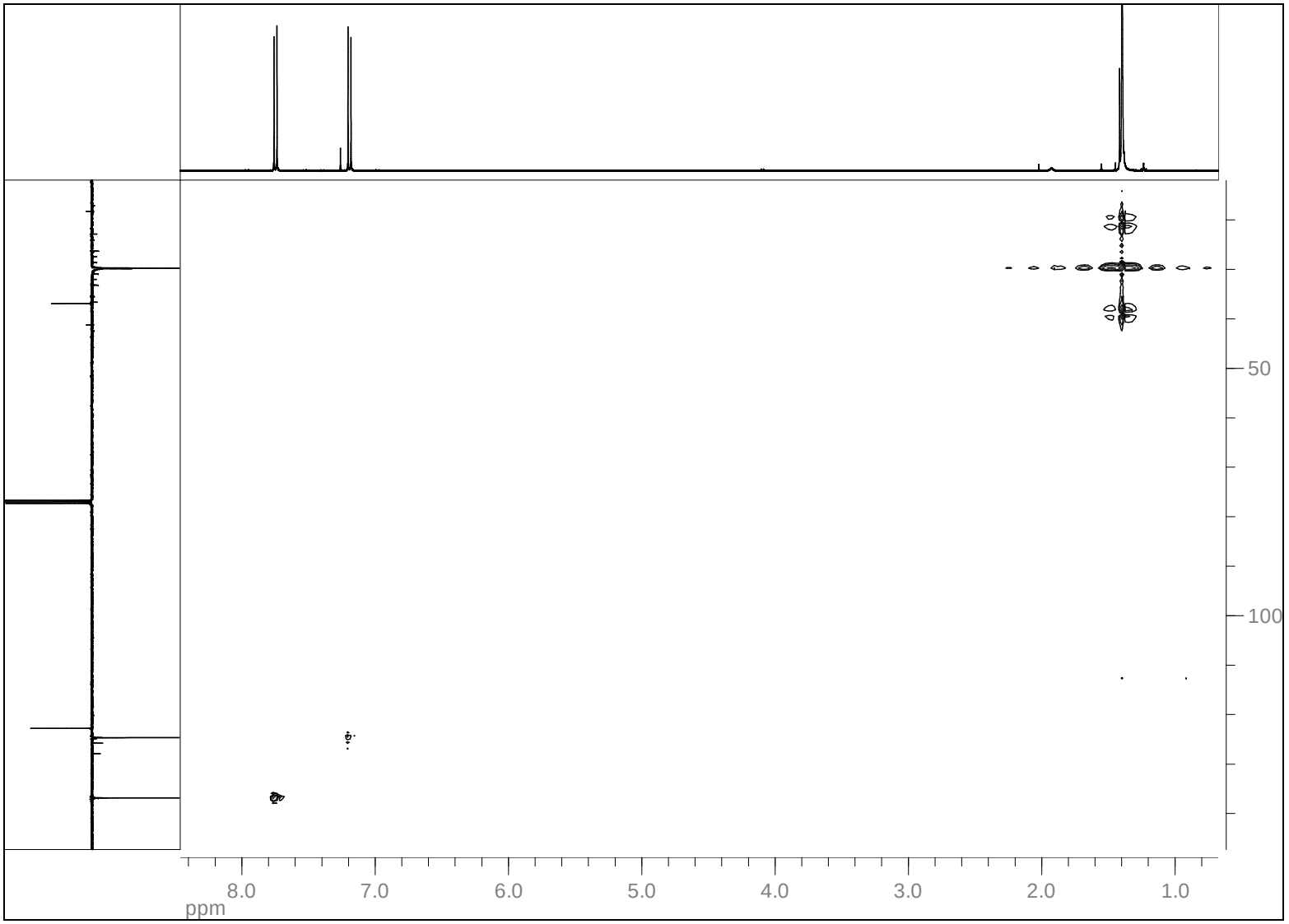

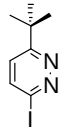

HMBC ($CDCl_3$): 3-*tert*-Butyl-6-iodopyridazine (**9**)

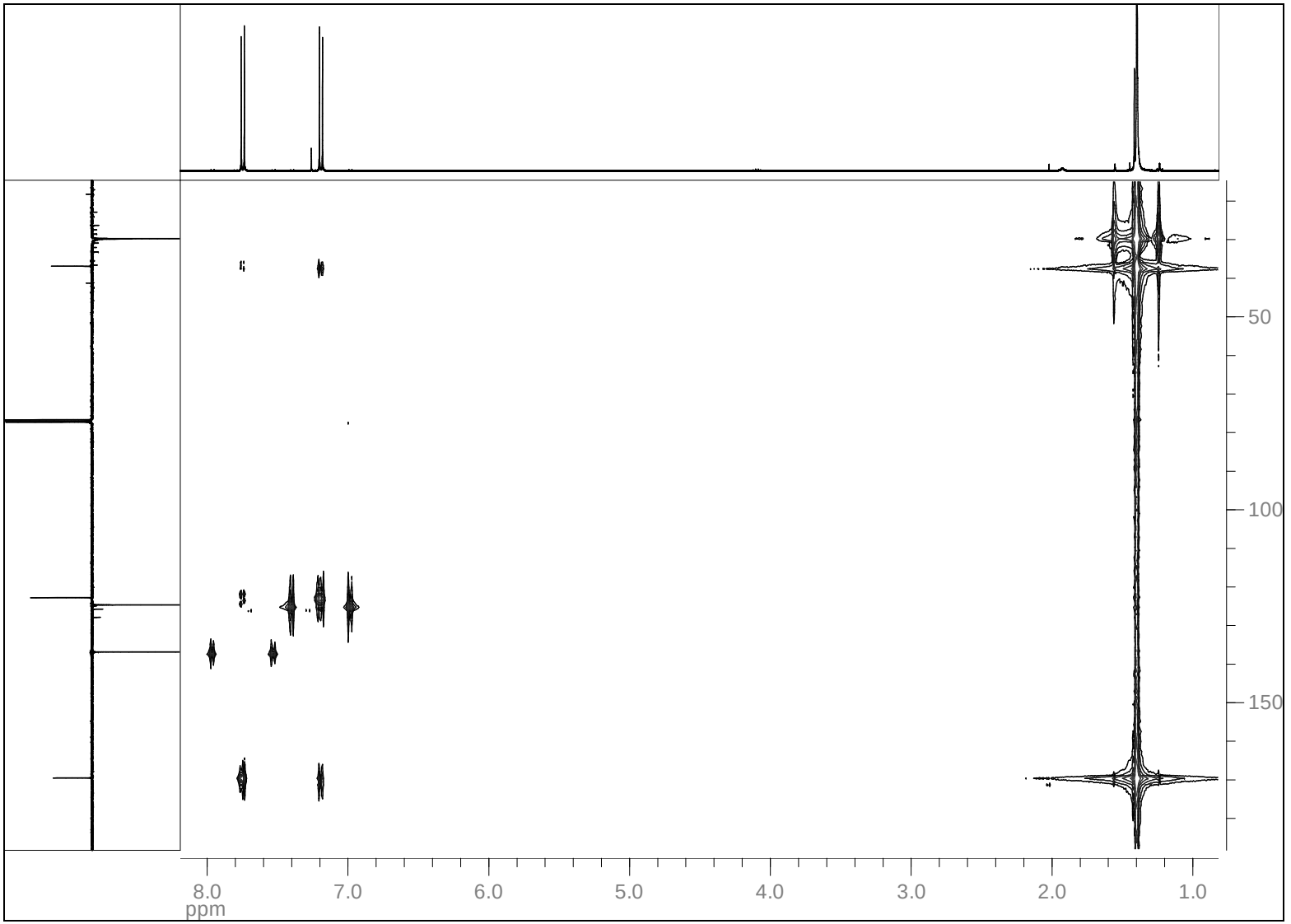

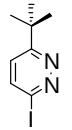

^{1}H NMR (400 MHz, $CDCl_3$): 3-*tert*-Butyl-6-((trimethylsilyl)ethynyl)pyridazine (**10**)

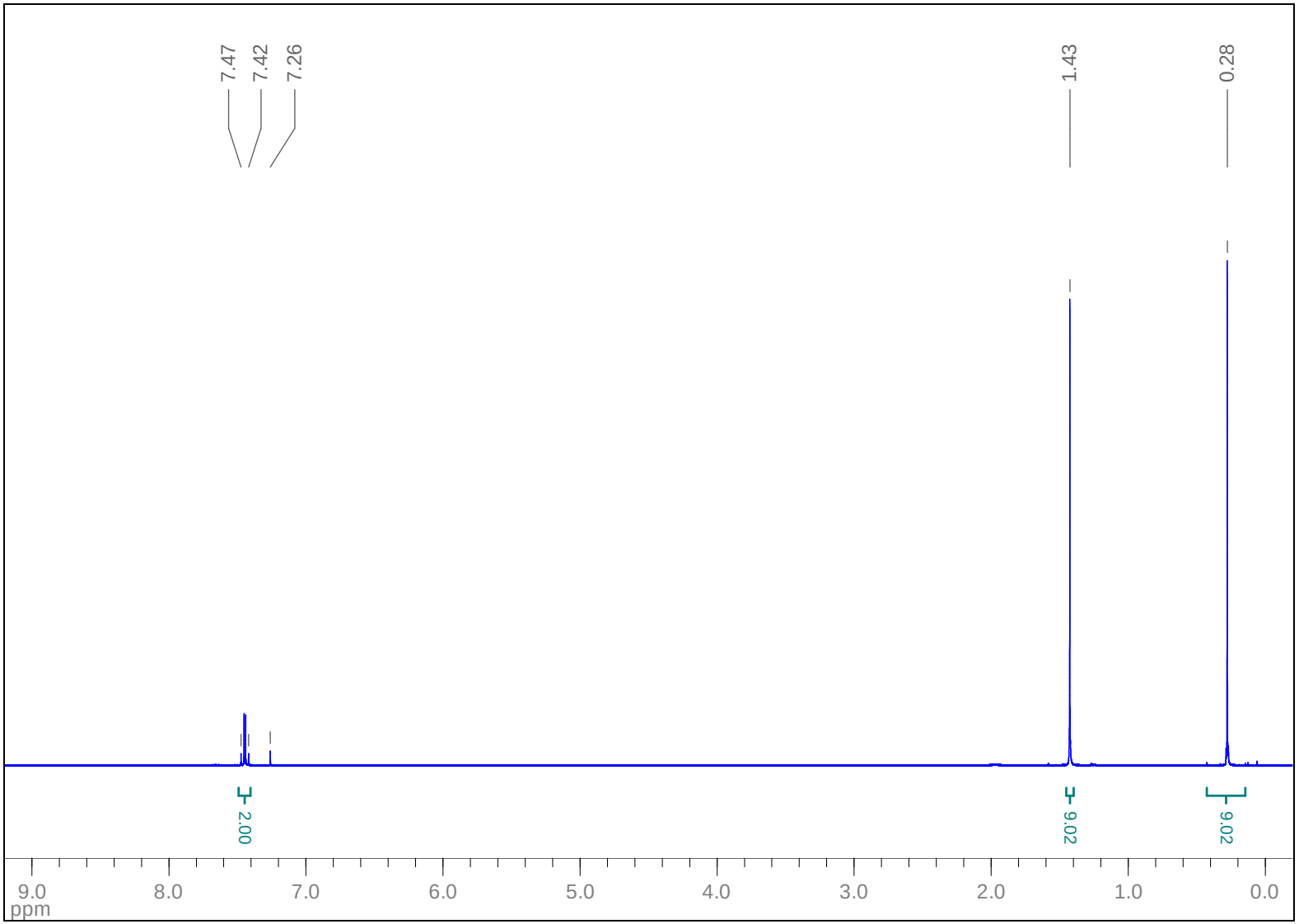

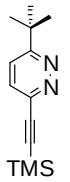

^{13}C {^{1}H} NMR (100 MHz, $CDCl_3$): 3-*tert*-Butyl-6-((trimethylsilyl)ethynyl)pyridazine (**10**)

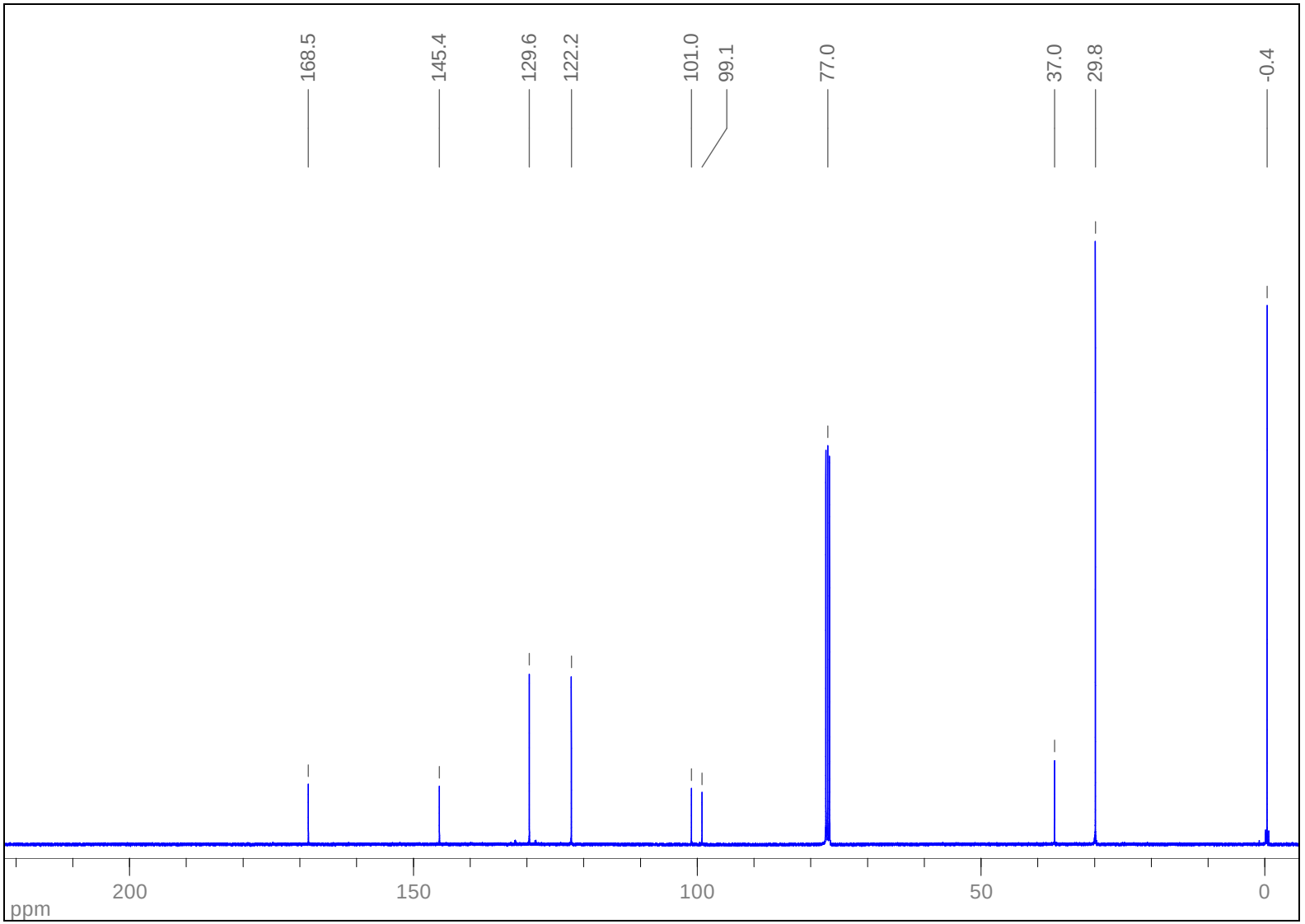

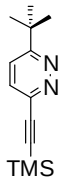

^{13}C APT NMR (100 MHz, $CDCl_3$): 3-*tert*-Butyl-6-((trimethylsilyl)ethynyl)pyridazine (**10**)

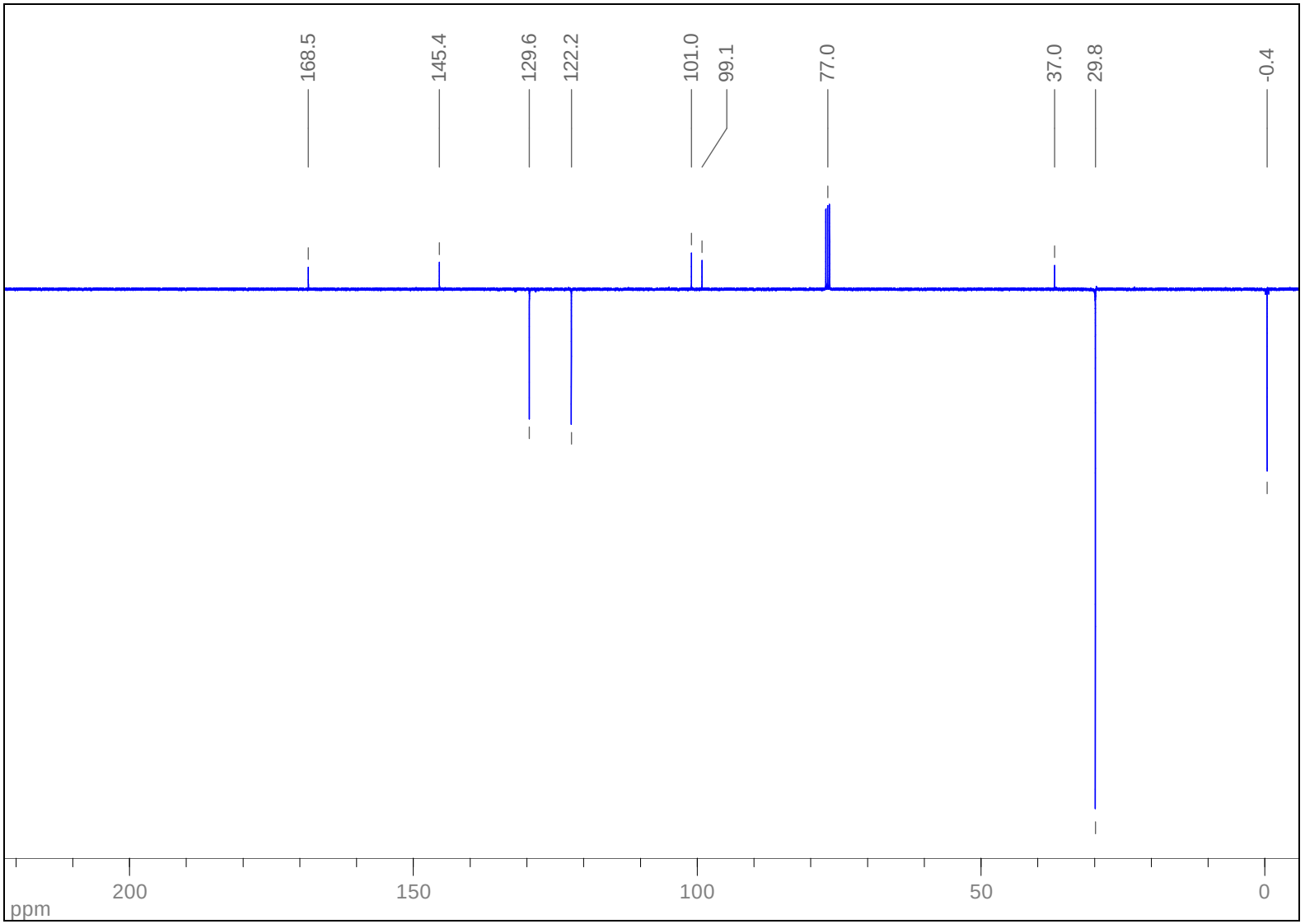

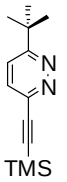

HSQC ($CDCl_3$): 3-*tert*-Butyl-6-((trimethylsilyl)ethynyl)pyridazine (**10**)

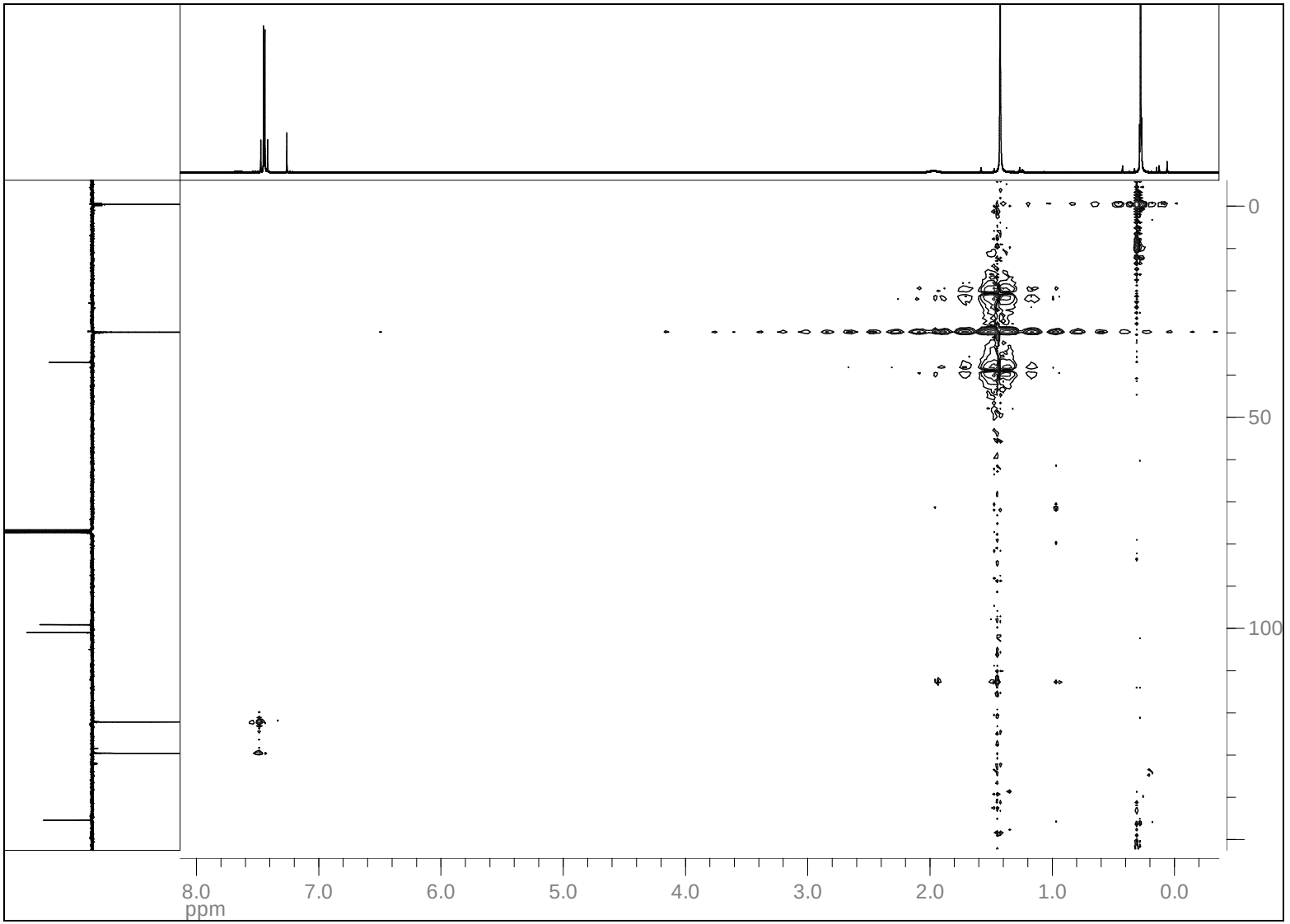

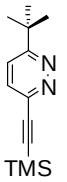

HMBC ($CDCl_3$): 3-*tert*-Butyl-6-((trimethylsilyl)ethynyl)pyridazine (**10**)

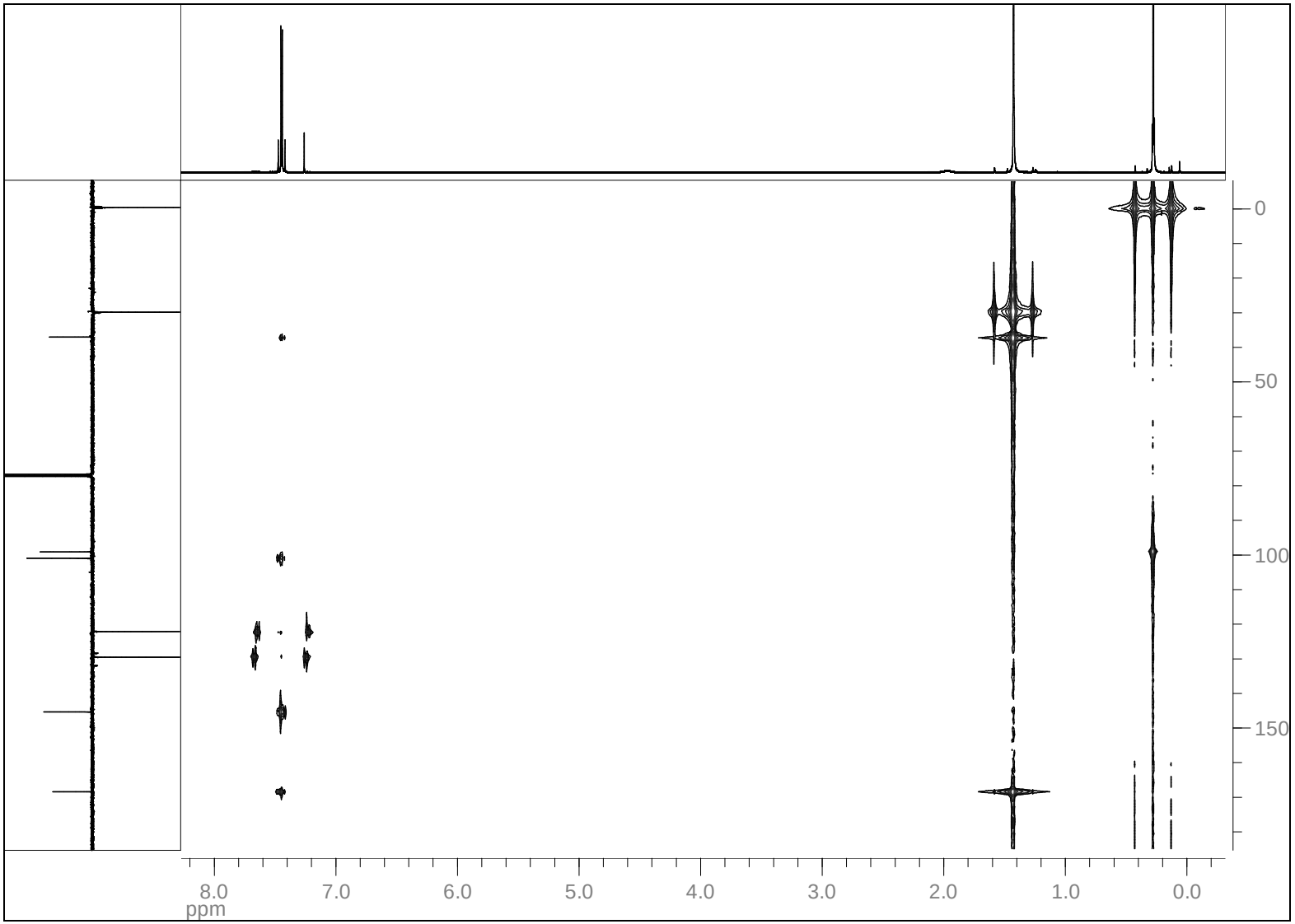

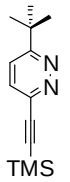

^{1}H NMR (400 MHz, $CDCl_3$): 3-*tert*-Butyl-6-ethynylpyridazine (**11**)

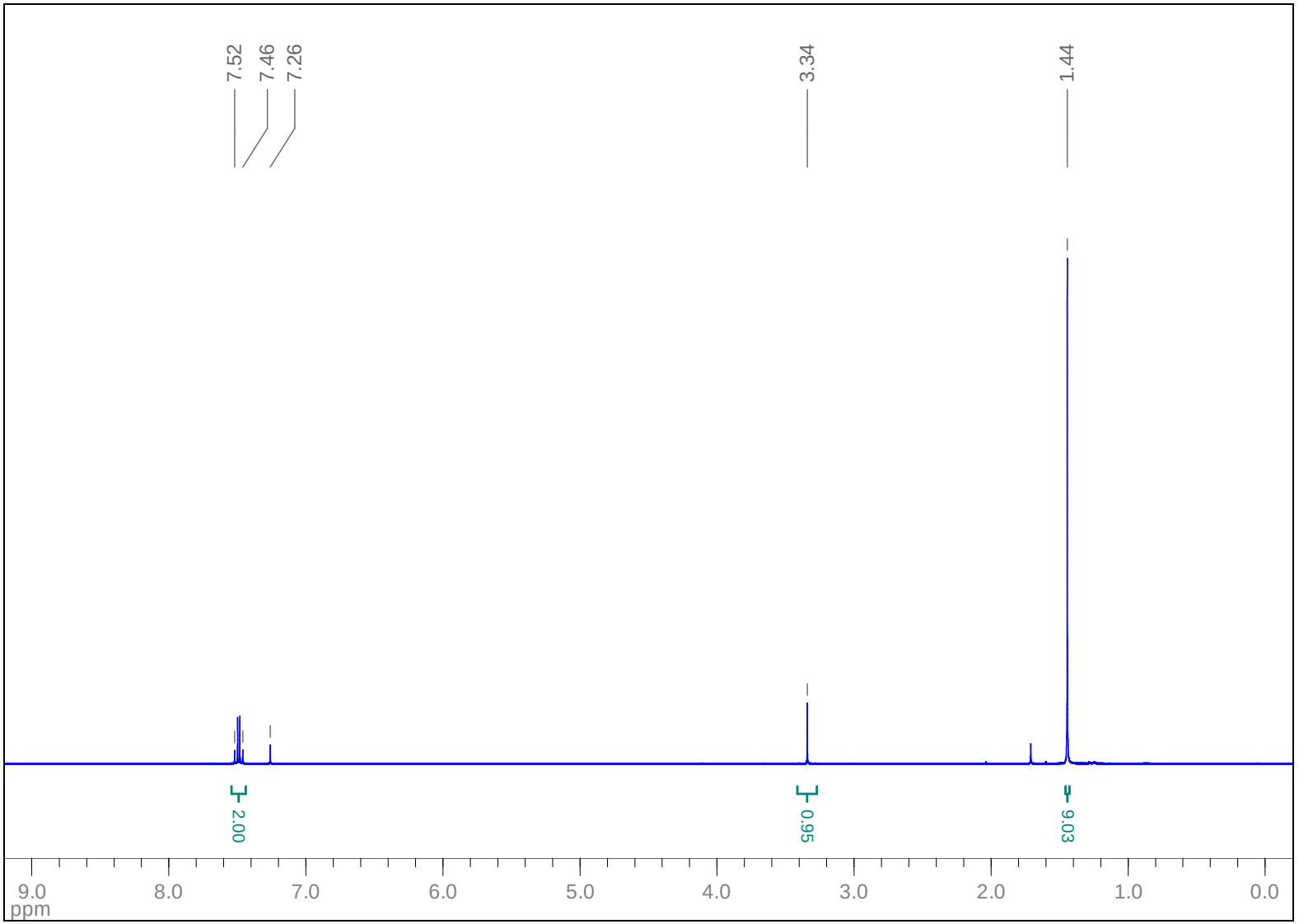

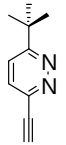

^{13}C {^{1}H} NMR (100 MHz, $CDCl_3$): 3-*tert*-Butyl-6-ethynylpyridazine (**11**)

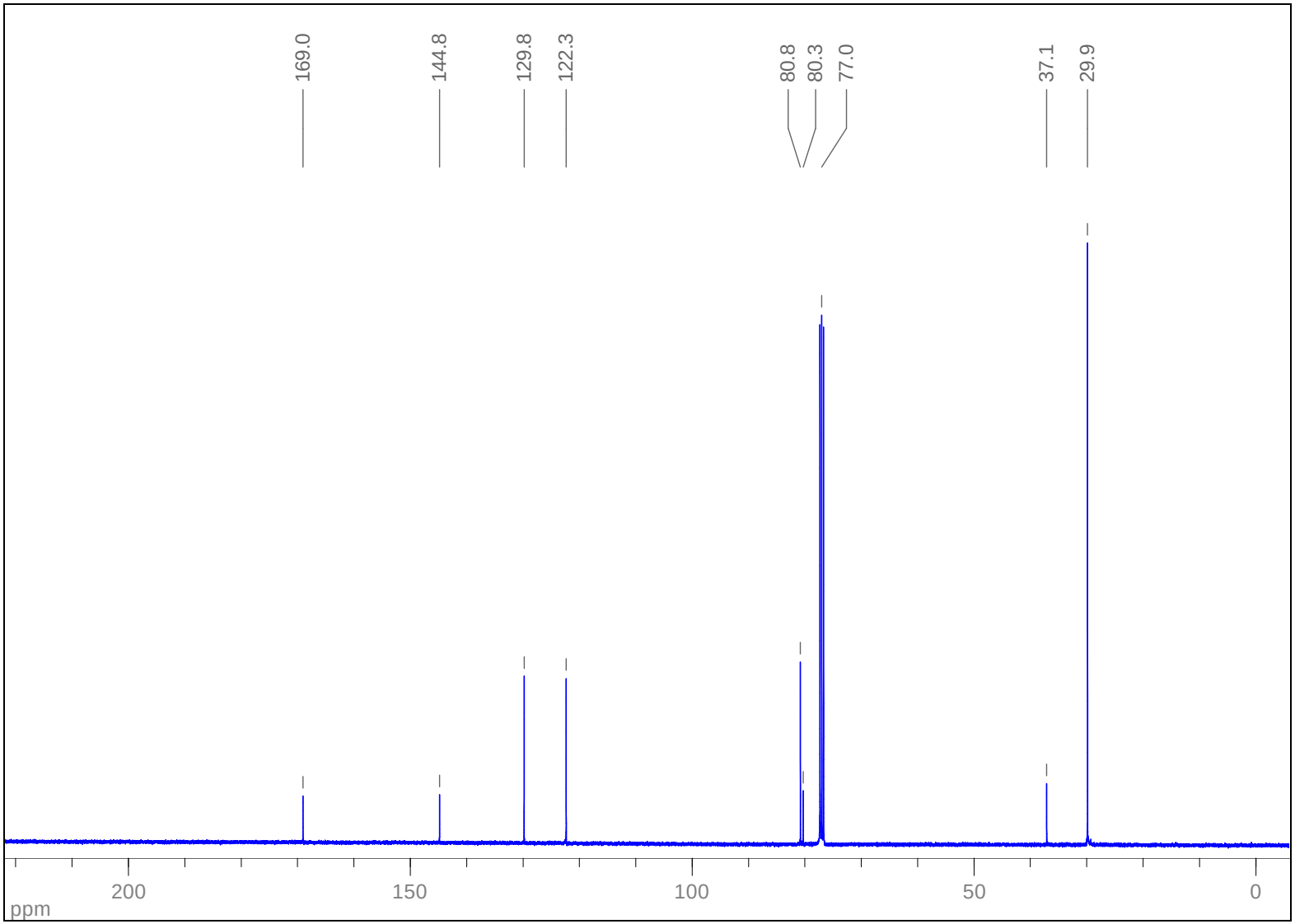

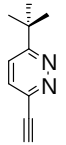

^{13}C APT NMR (100 MHz, $CDCl_3$): 3-*tert*-Butyl-6-ethynylpyridazine (**11**)

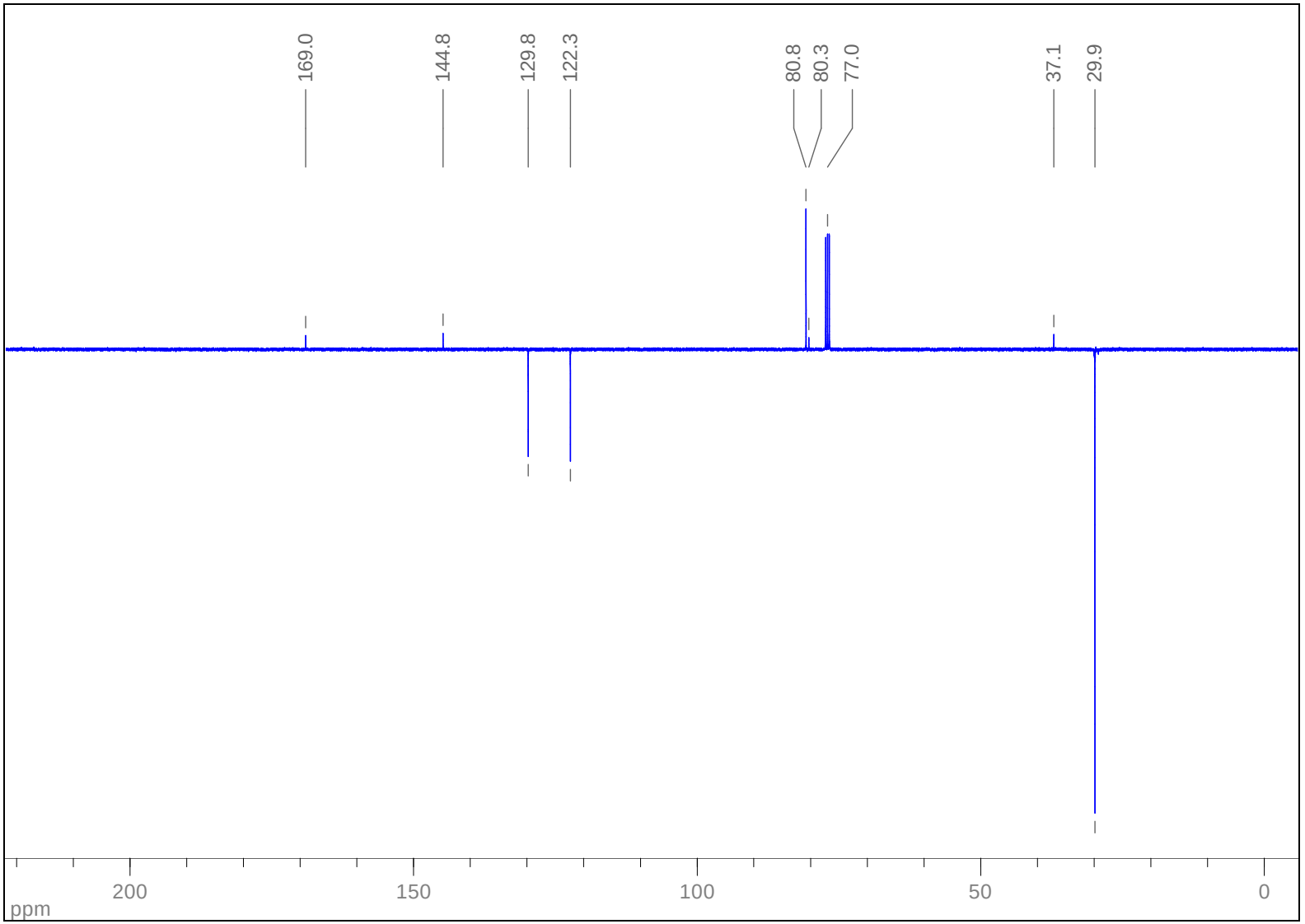

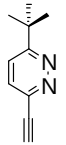

HSQC ($CDCl_3$): 3-*tert*-Butyl-6-ethynylpyridazine (**11**)

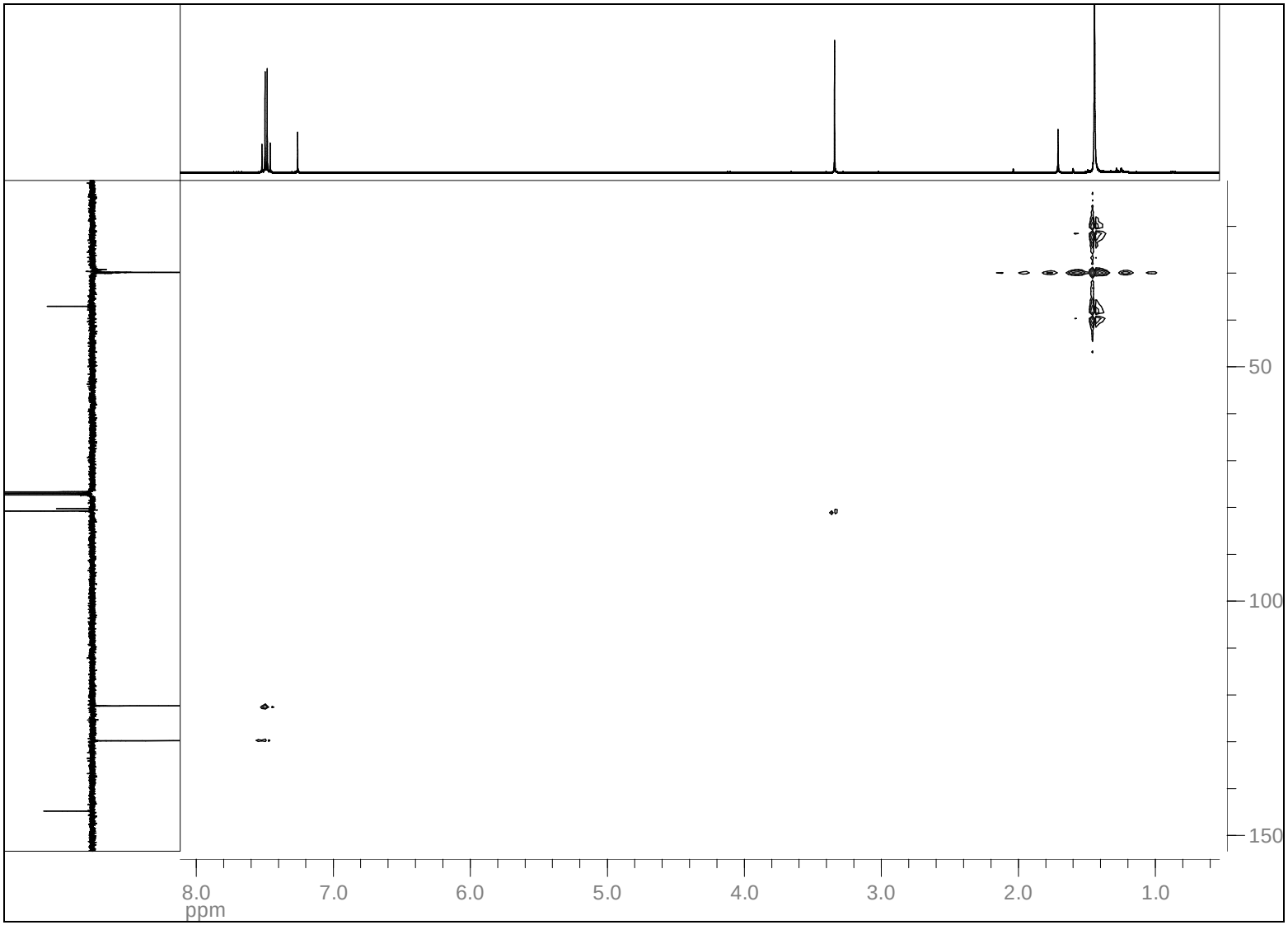

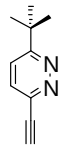

HMBC ($CDCl_3$): 3-*tert*-Butyl-6-ethynylpyridazine (**11**)

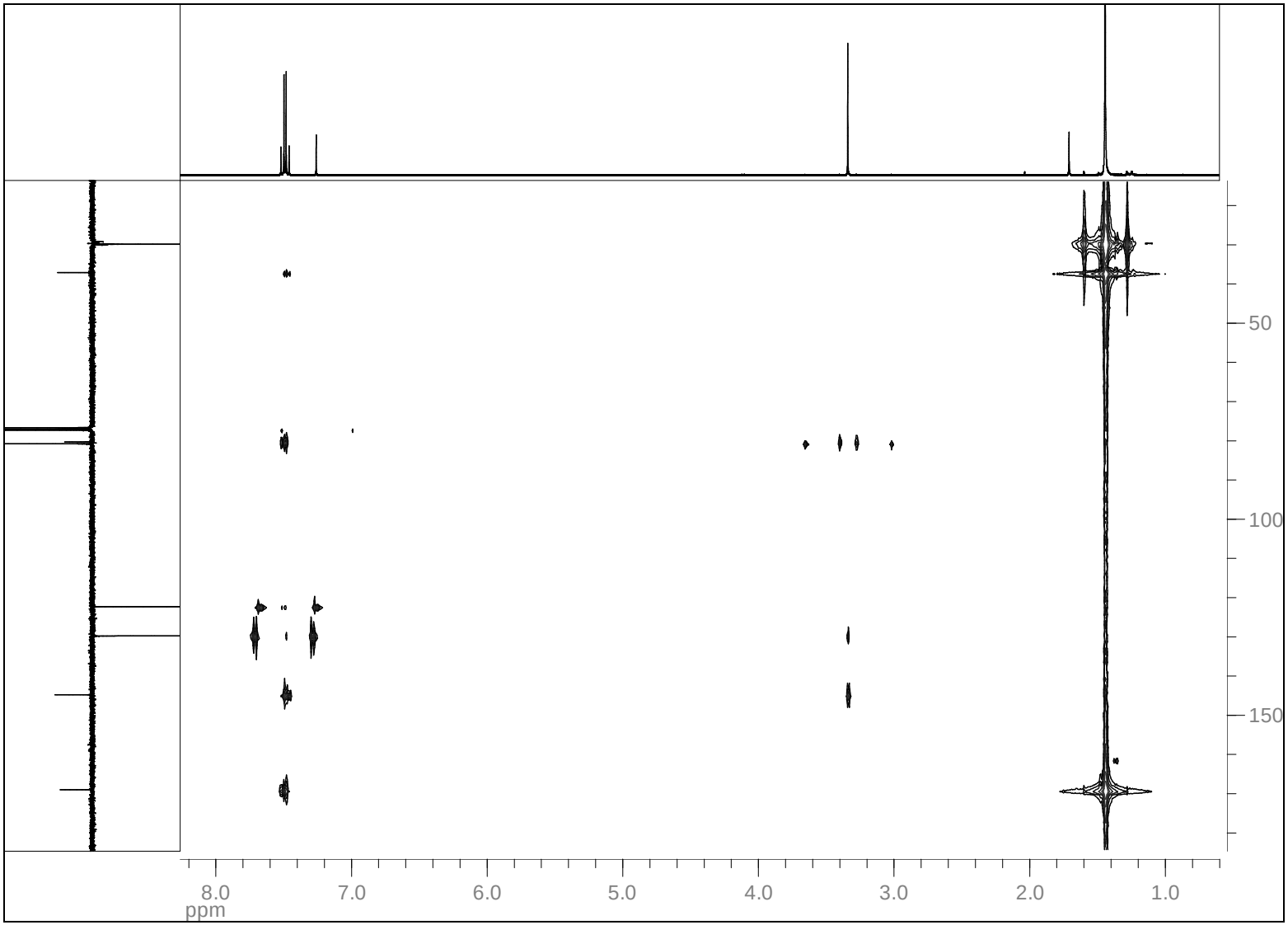

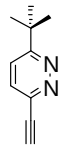

^{1}H NMR (400 MHz, $CDCl_3$): 3-(3,3-Dimethylbut-1-ynyl)-6-iodopyridazine (**12**)

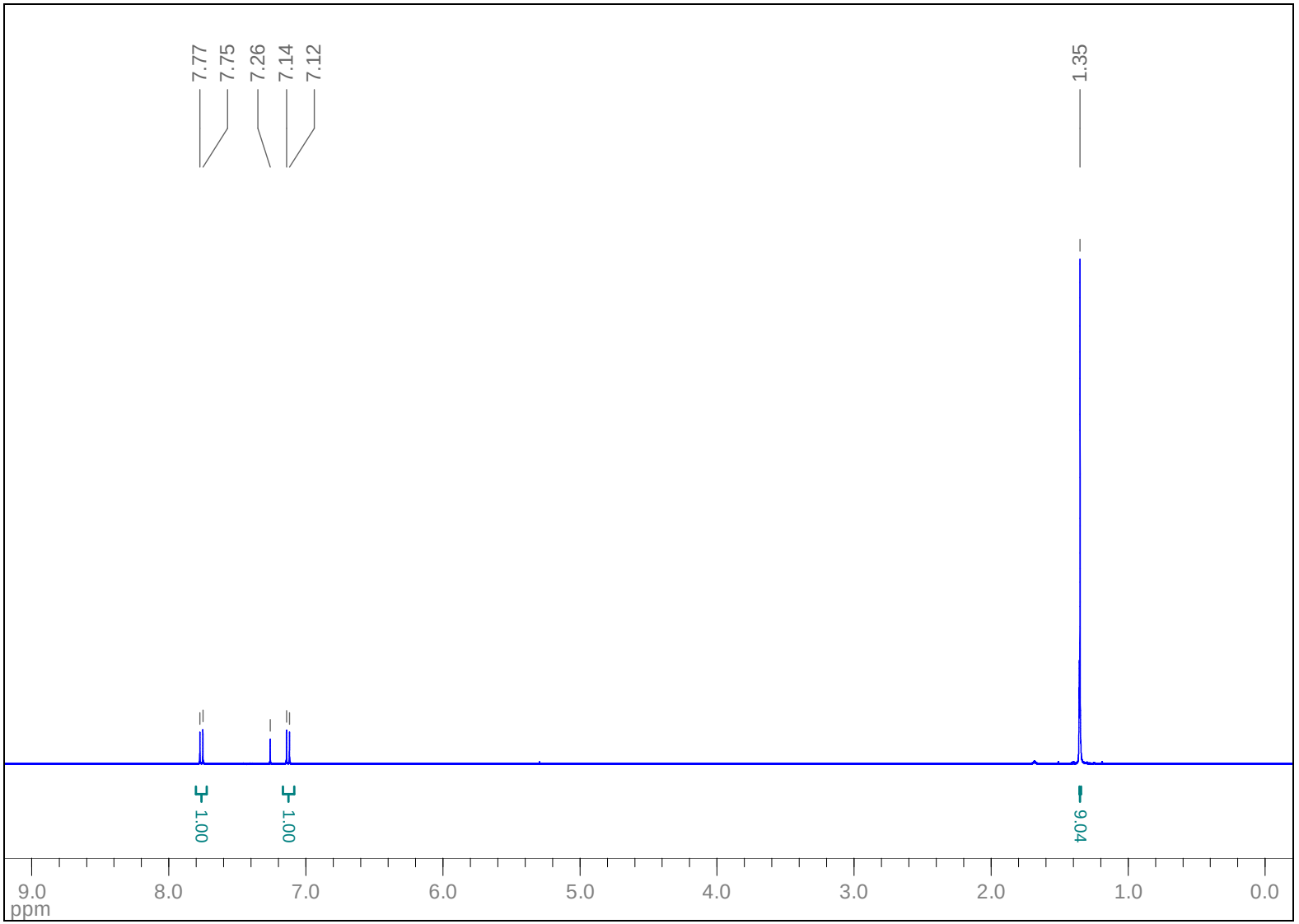

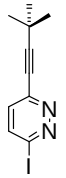

^{13}C {^{1}H} NMR (100 MHz, $CDCl_3$): 3-(3,3-Dimethylbut-1-ynyl)-6-iodopyridazine (**12**)

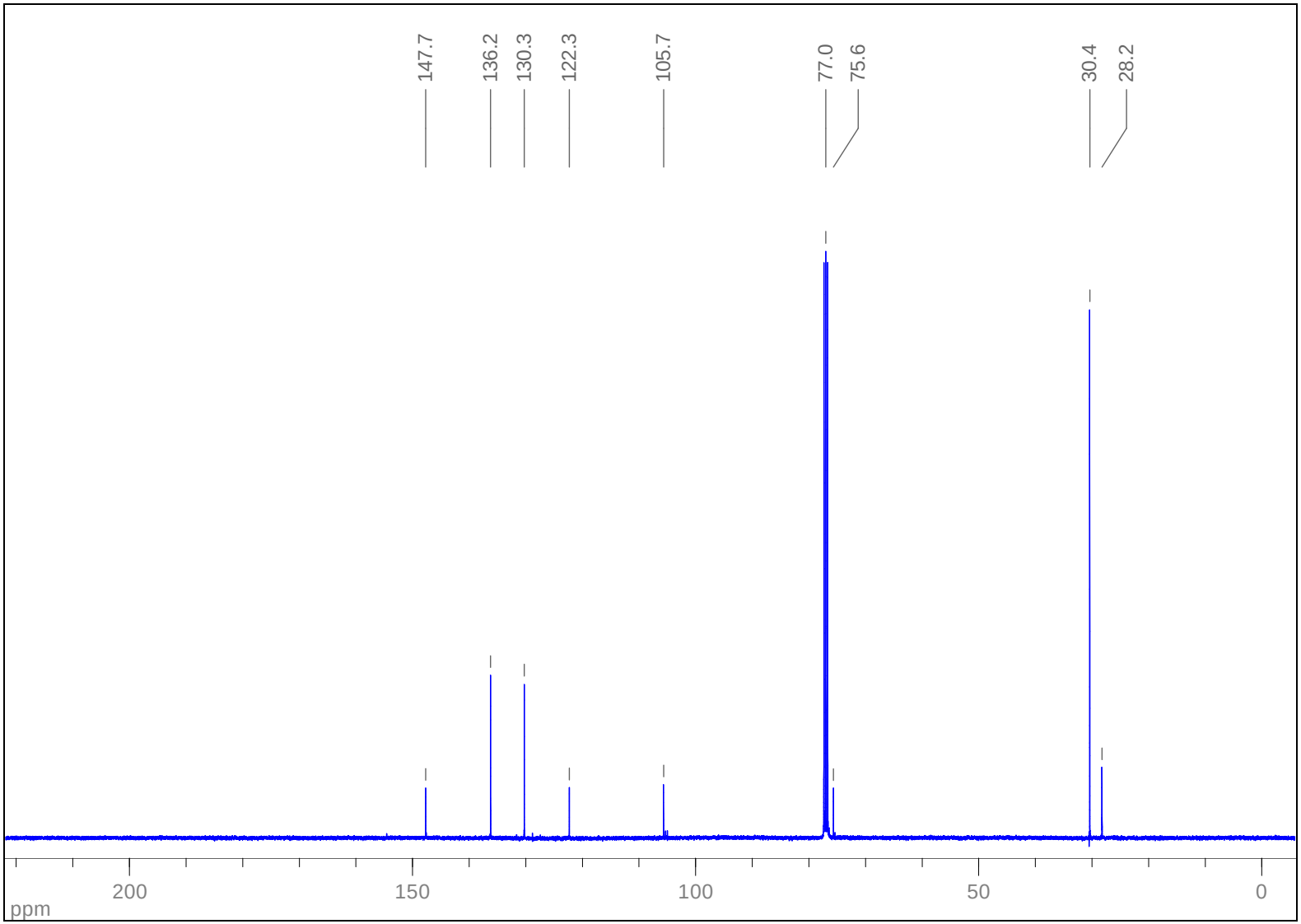

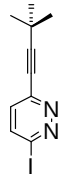

^{13}C APT NMR (100 MHz, $CDCl_3$): 3-(3,3-Dimethylbut-1-ynyl)-6-iodopyridazine (**12**)

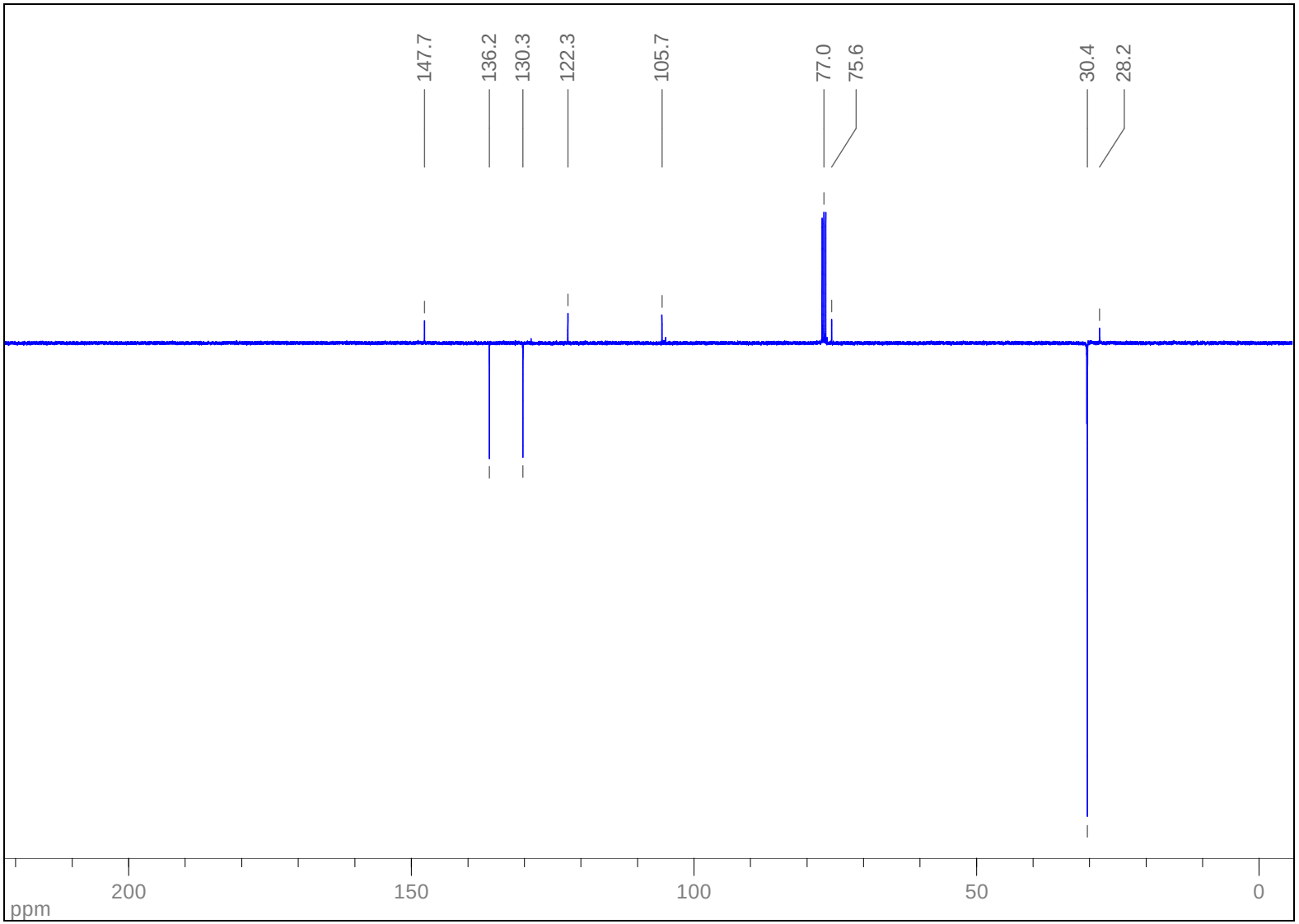

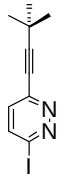

$^{1}H - {}^{1}H$ COSY ($CDCl_3$): 3-(3,3-Dimethylbut-1-ynyl)-6-iodopyridazine (**12**)

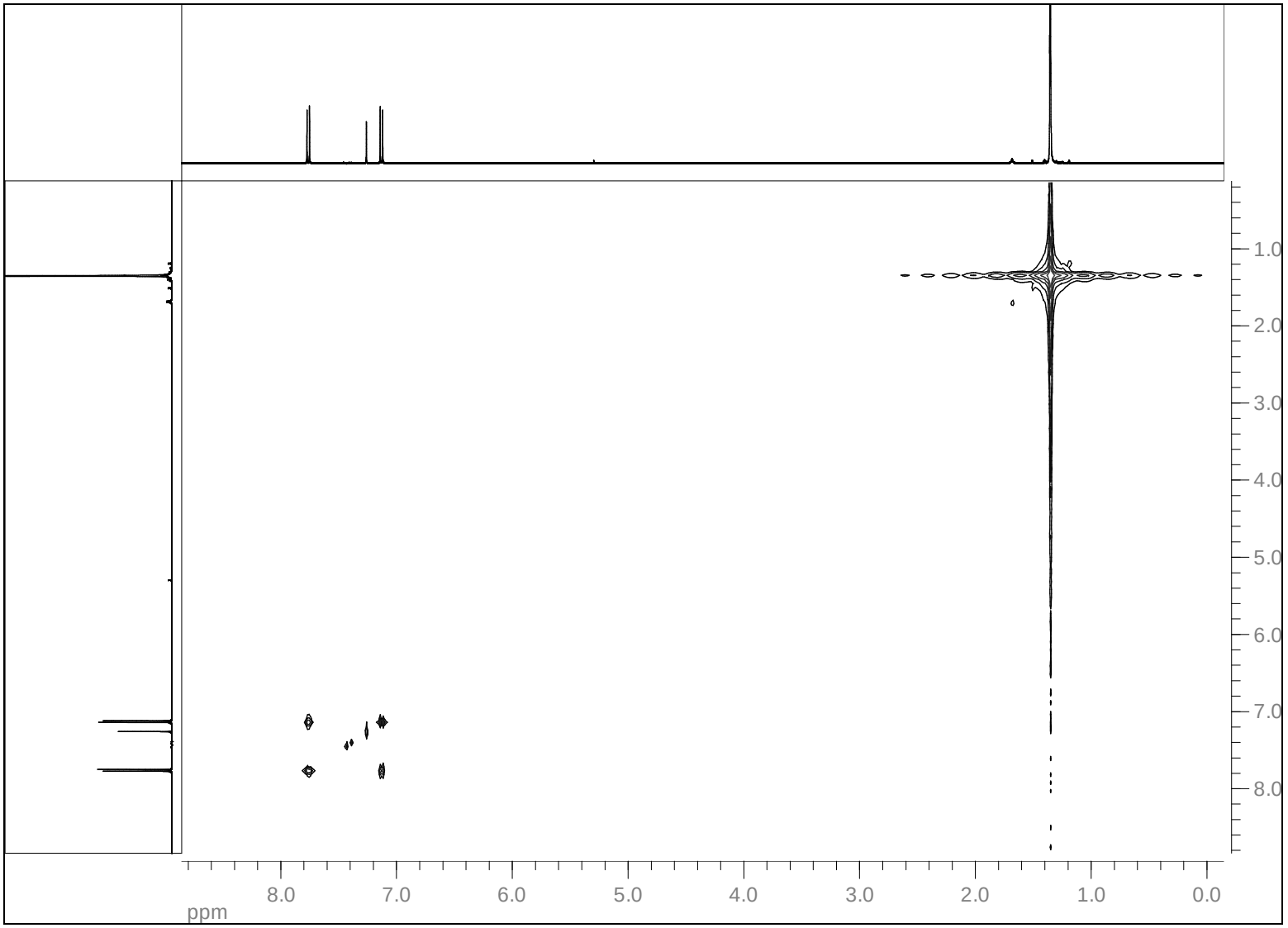

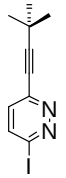

HSQC ($CDCl_3$): 3-(3,3-Dimethylbut-1-ynyl)-6-iodopyridazine (**12**)

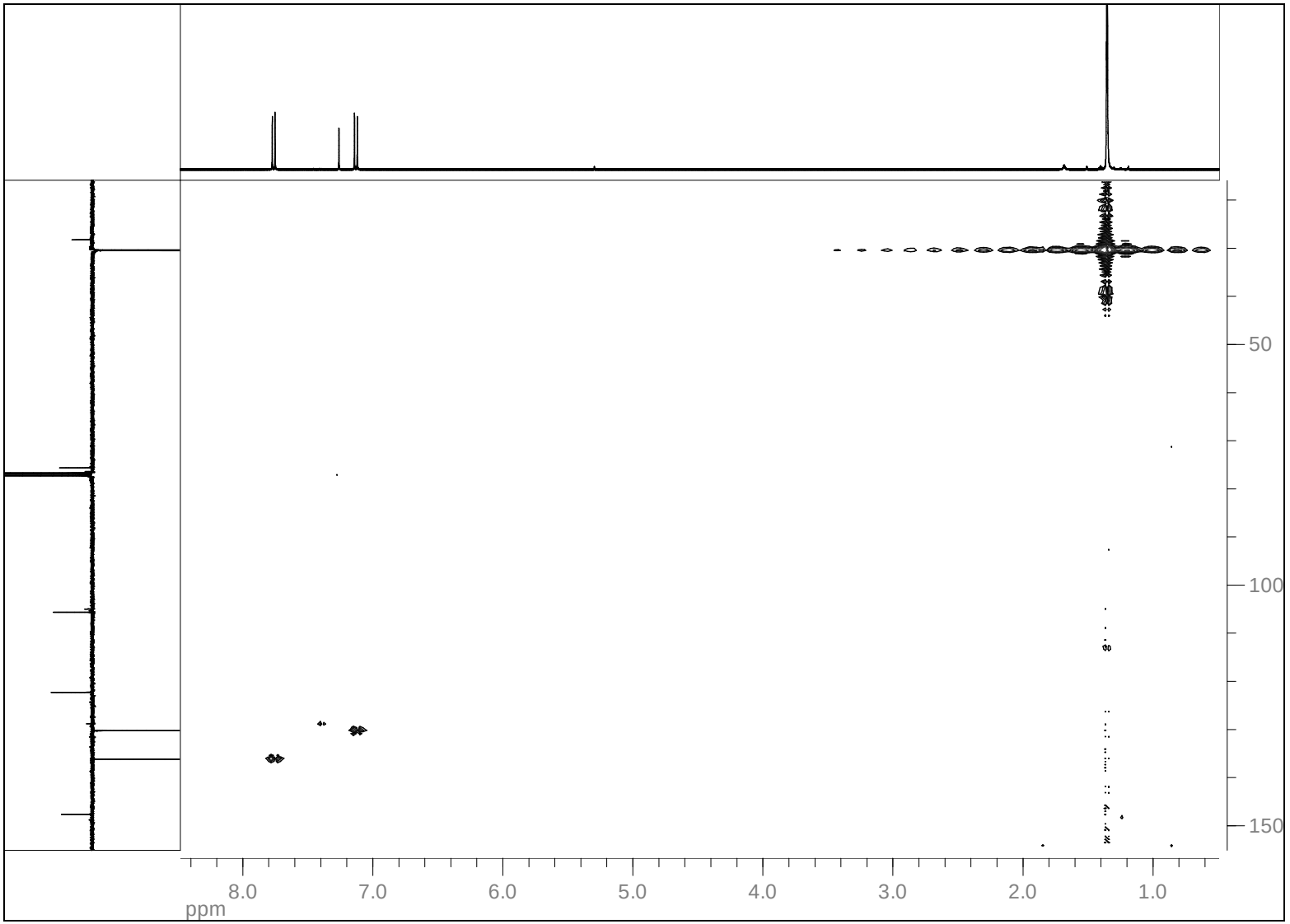

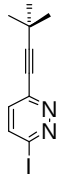

HMBC ($CDCl_3$): 3-(3,3-Dimethylbut-1-ynyl)-6-iodopyridazine (**12**)

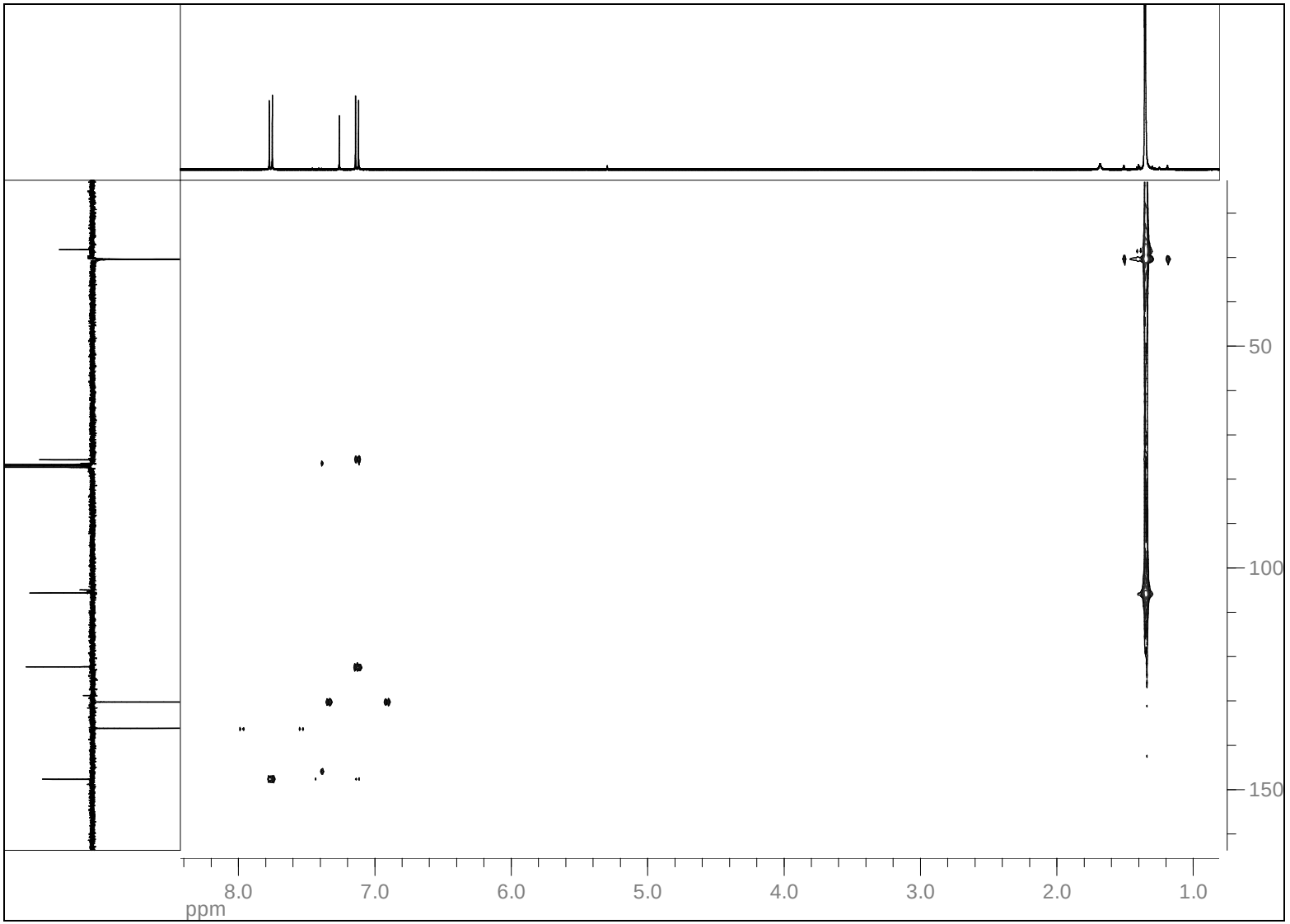

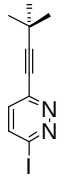

^{1}H NMR (400 MHz, $CDCl_3$): 1,3-Di(buta-1,3-diynyl)bicyclo[1.1.1]pentane (**18**)

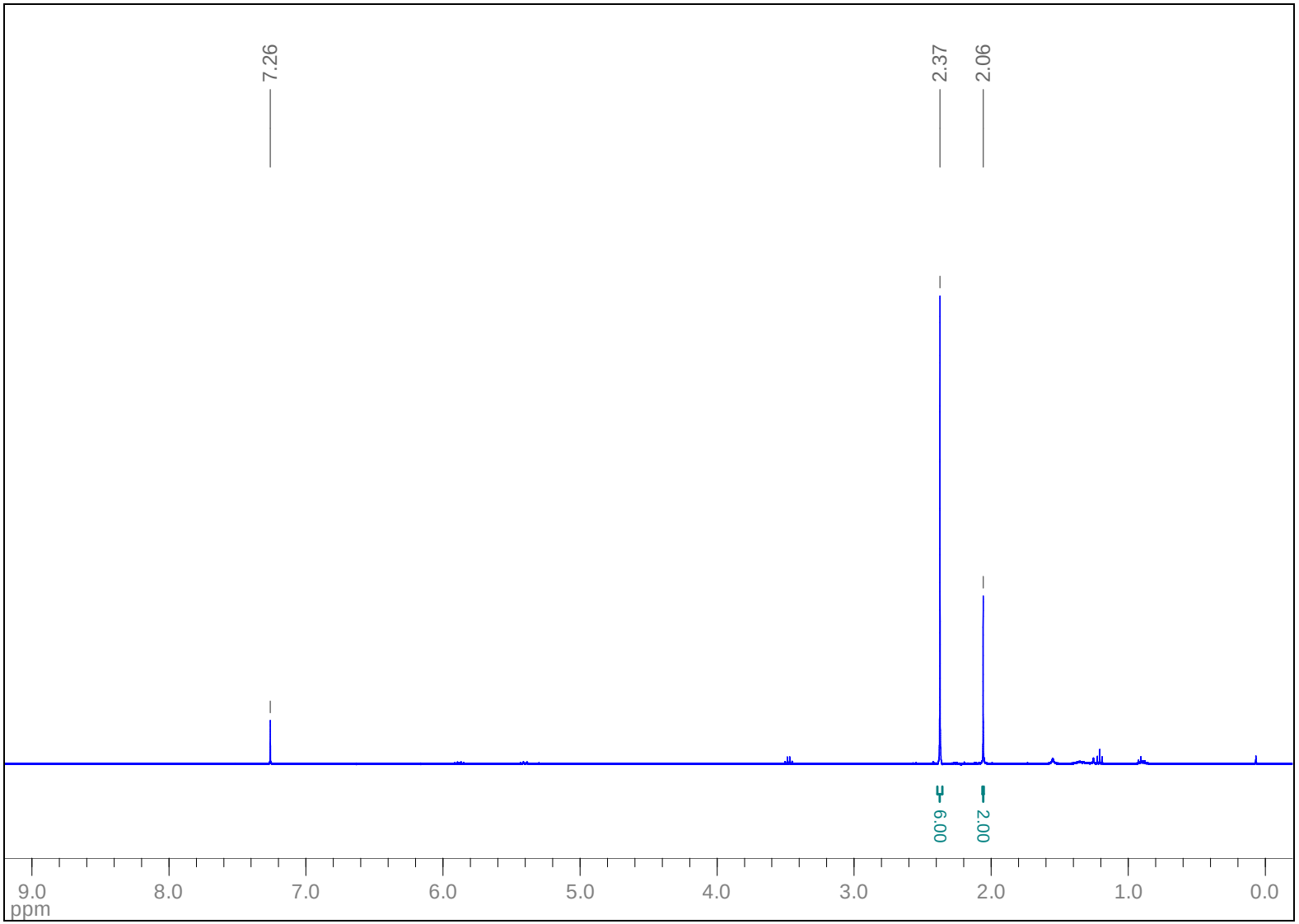

^{13}C {^{1}H} NMR (100 MHz, $CDCl_3$): 1,3-Di(buta-1,3-diynyl)bicyclo[1.1.1]pentane (**18**)

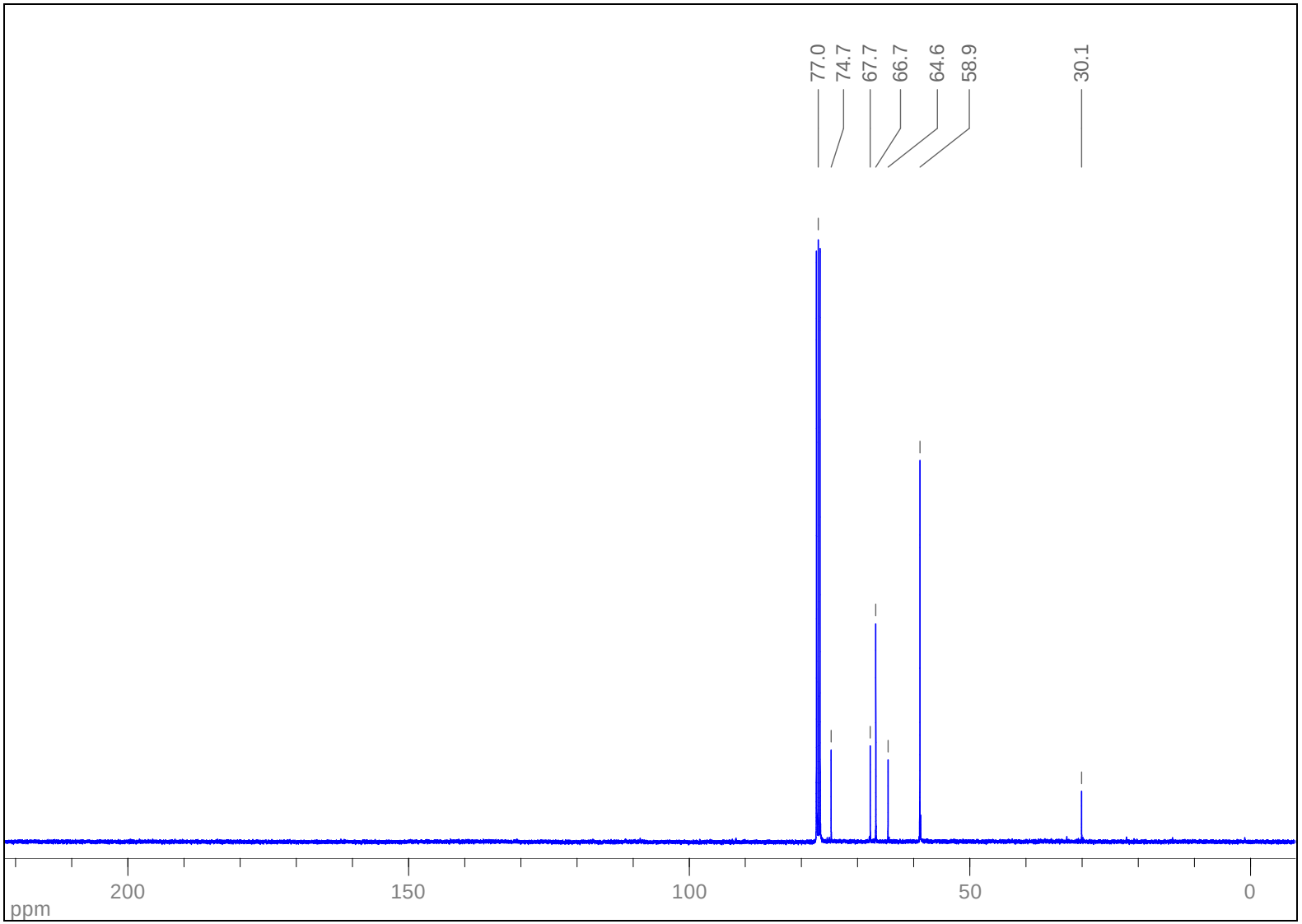

HSQC ($CDCl_3$): 1,3-Di(buta-1,3-diynyl)bicyclo[1.1.1]pentane (**18**)

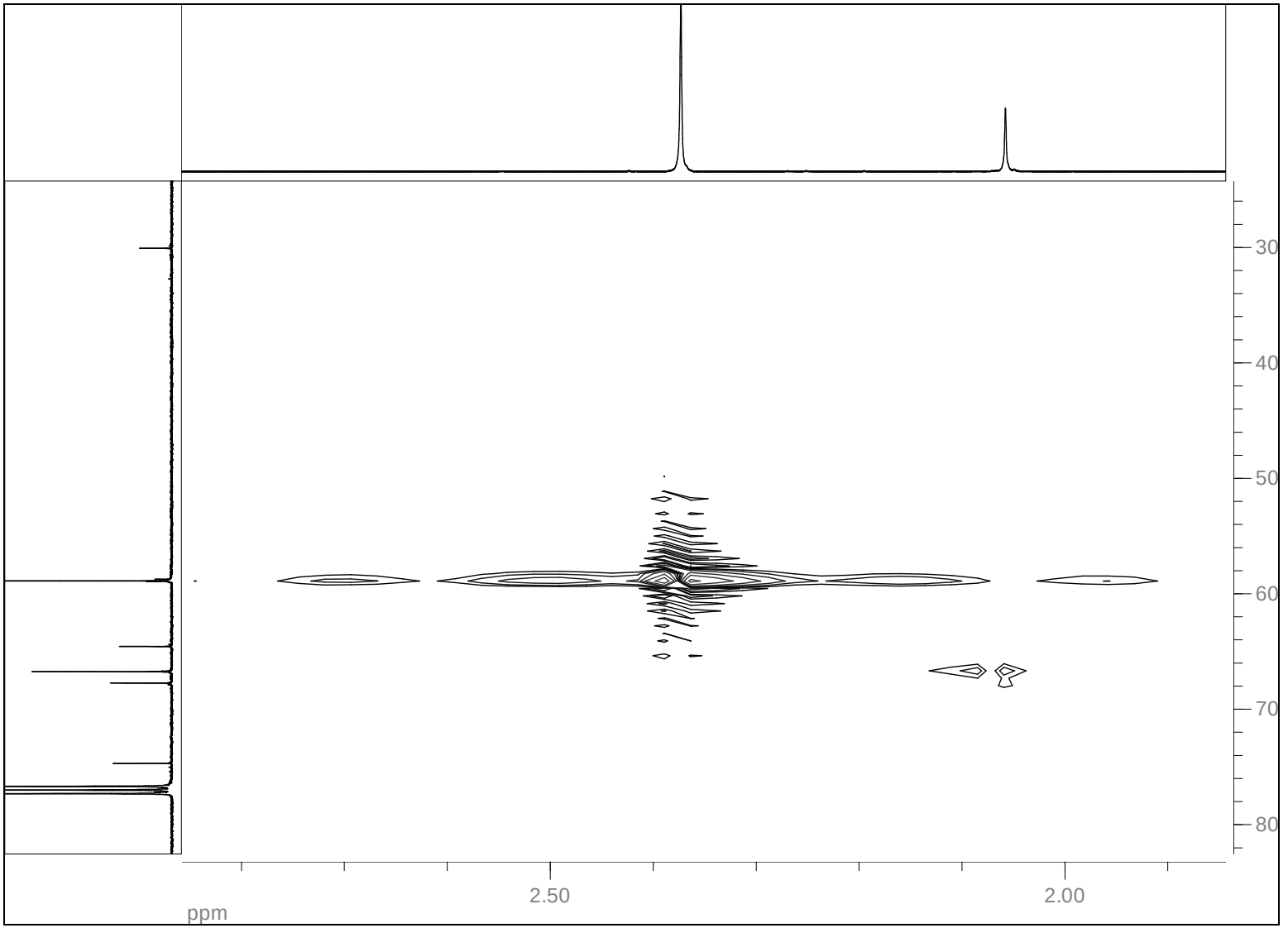

HMBC ($CDCl_3$): 1,3-Di(buta-1,3-diynyl)bicyclo[1.1.1]pentane (**18**)

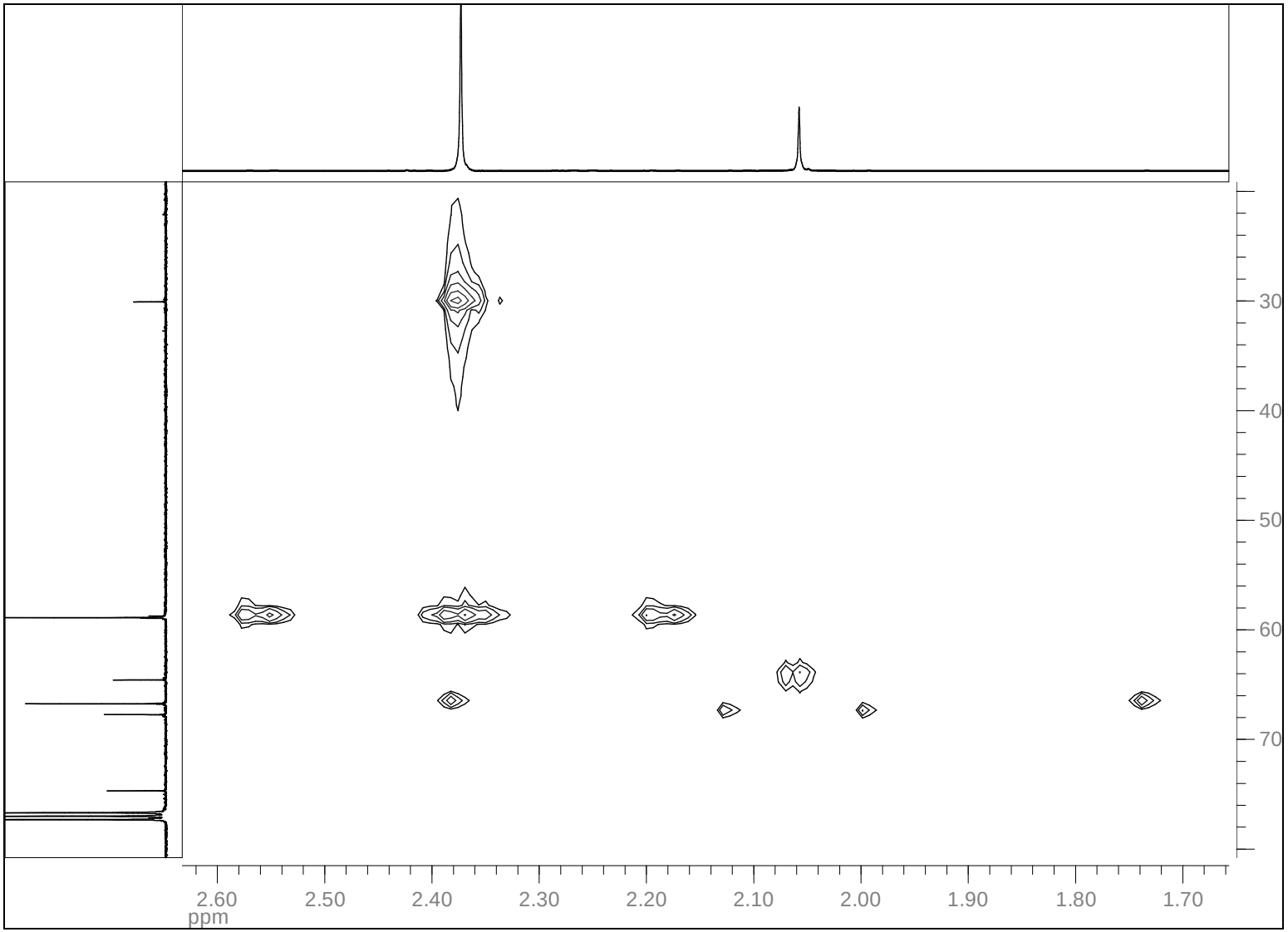

^{1}H NMR (400 MHz, $CDCl_3$): 3,3'-(Bicyclo[1.1.1]penta-1,3-diyl)diprop-2-yn-1-ol (**19**)

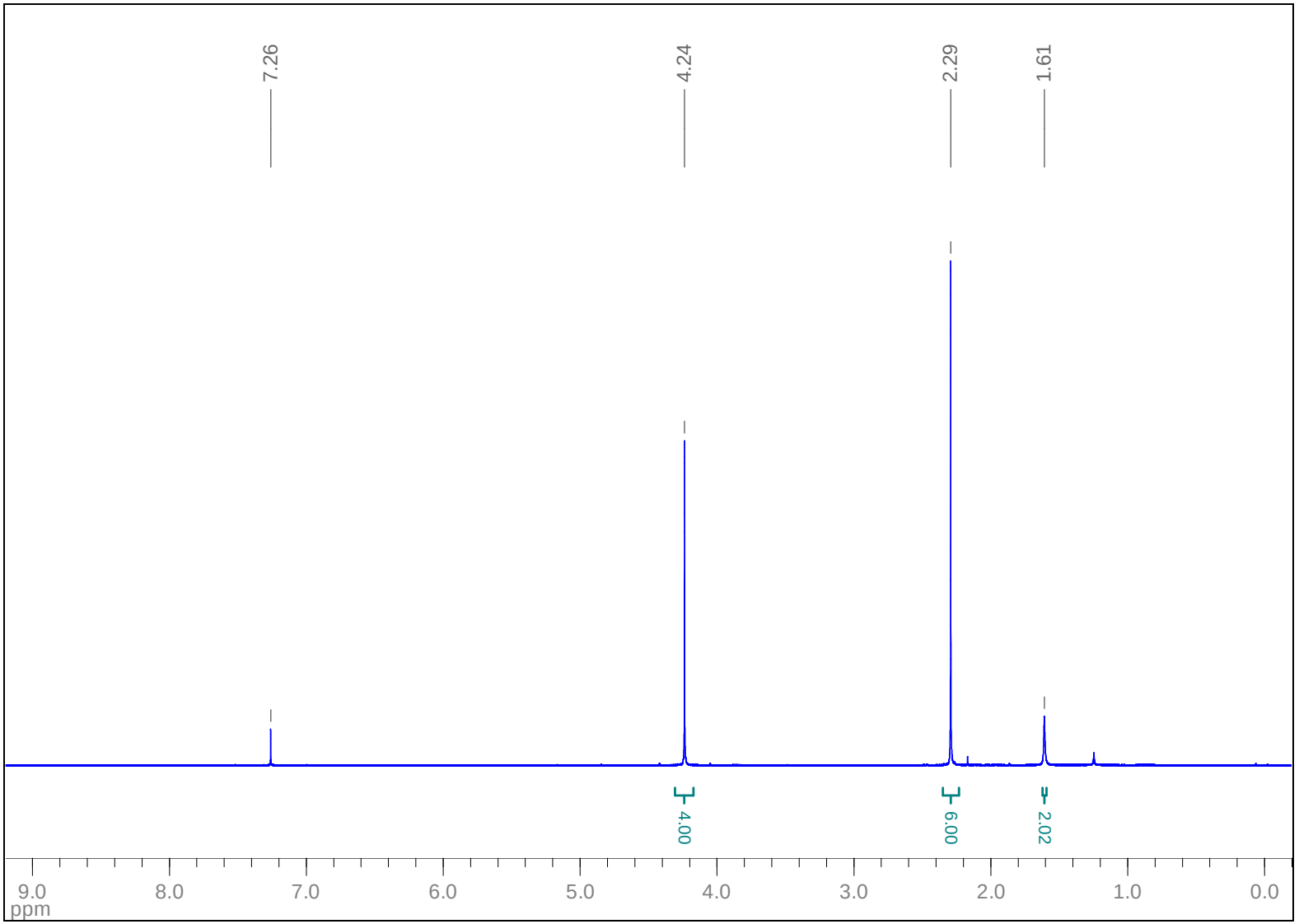

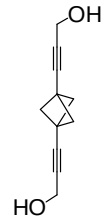

^{13}C {^{1}H} NMR (100 MHz, $CDCl_3$): 3,3'-(Bicyclo[1.1.1]penta-1,3-diyl)diprop-2-yn-1-ol (**19**)

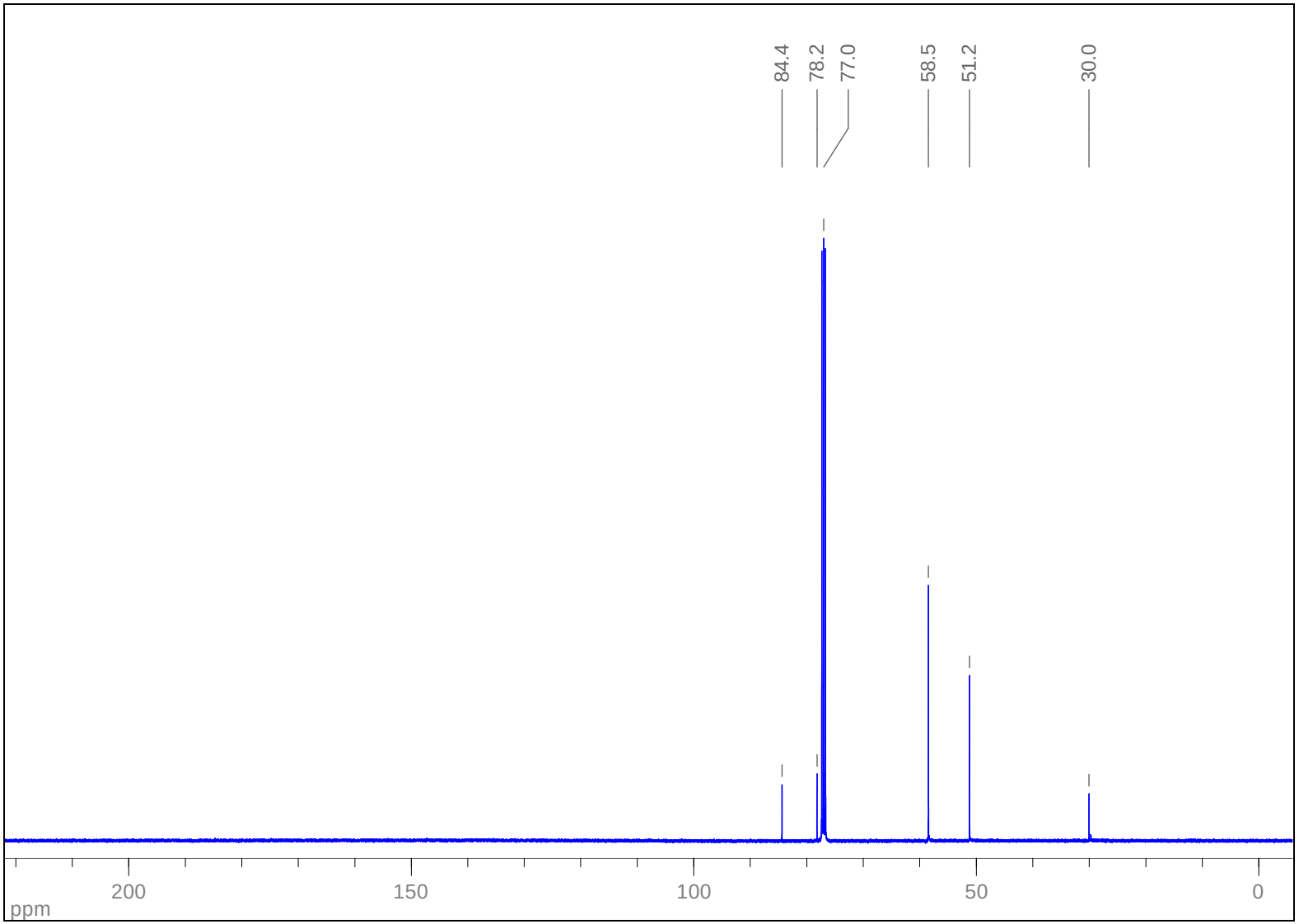

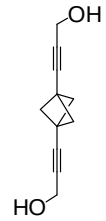

^{13}C APT NMR (100 MHz, $CDCl_3$): 3,3'-(Bicyclo[1.1.1]penta-1,3-diyl)diprop-2-yn-1-ol (**19**)

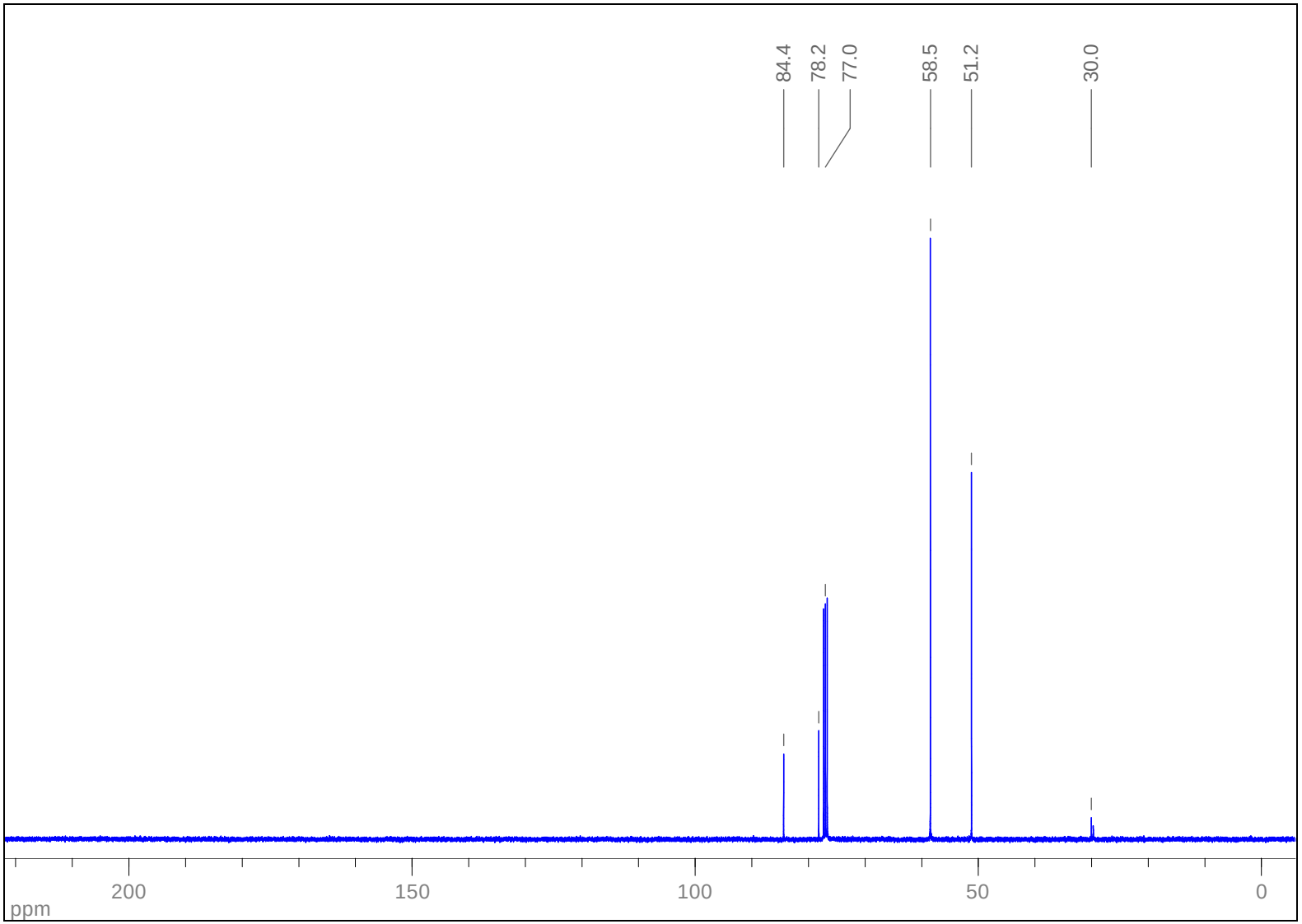

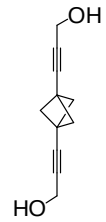

HSQC ($CDCl_3$): 3,3'-(Bicyclo[1.1.1]penta-1,3-diyl)diprop-2-yn-1-ol (**19**)

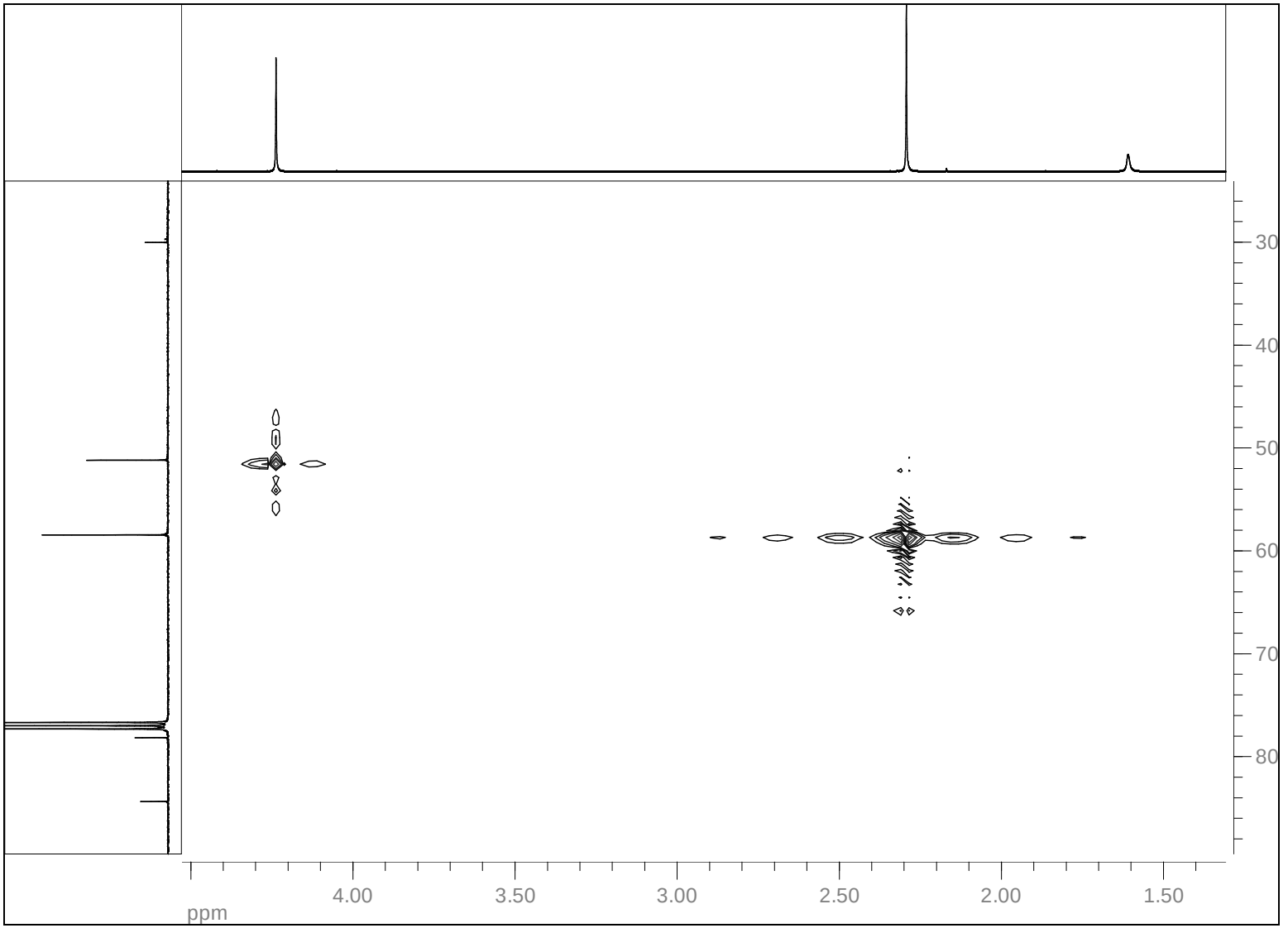

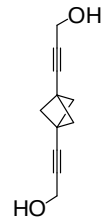

HMBC ($CDCl_3$): 3,3'-(Bicyclo[1.1.1]penta-1,3-diyl)diprop-2-yn-1-ol (**19**)

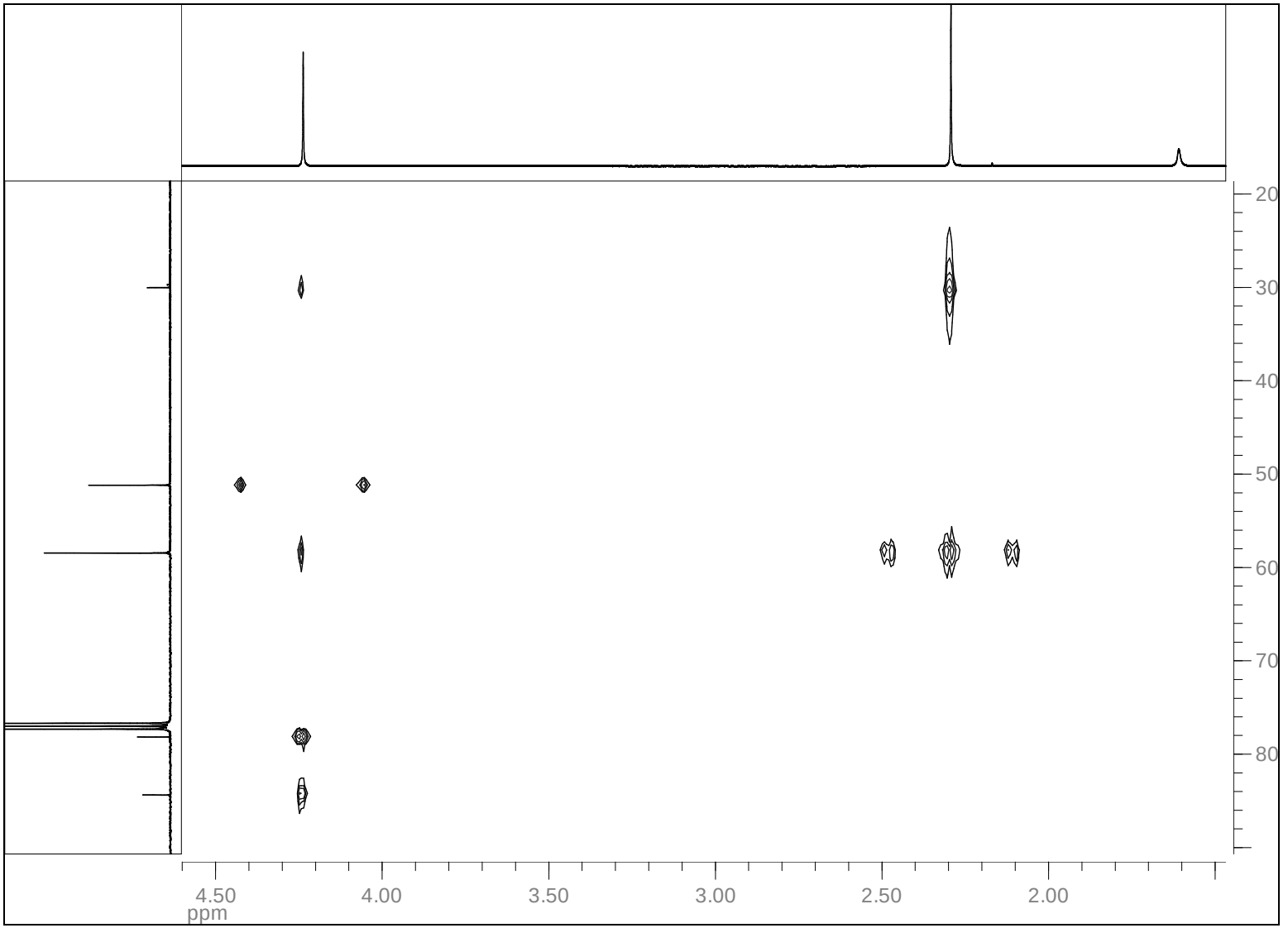

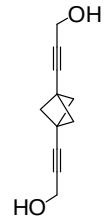

^{1}H NMR (400 MHz, $CDCl_3$): 3,3'-(Bicyclo[1.1.1]penta-1,3-diyl)dipropiolaldehyde (**20**)

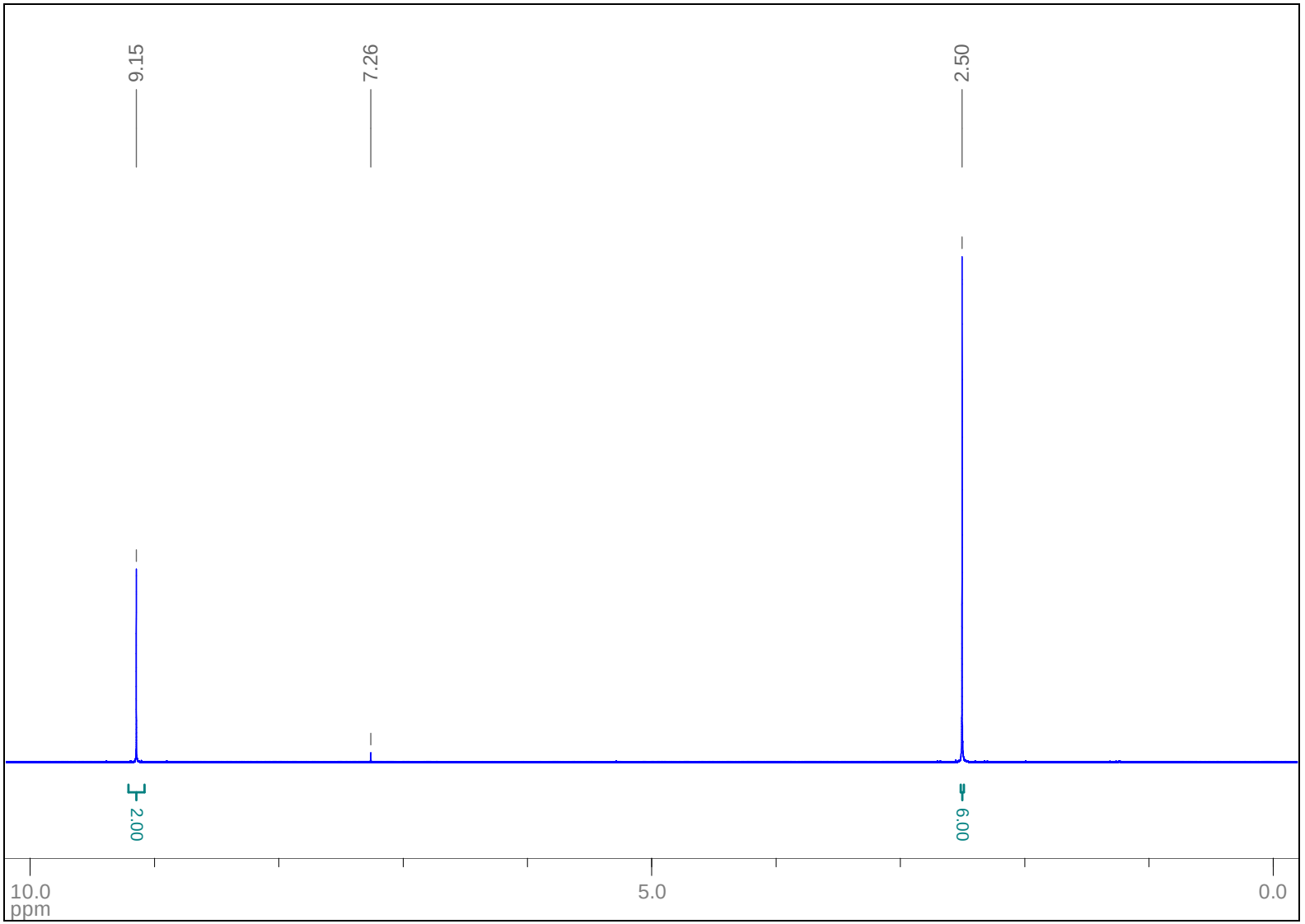

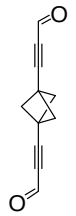

^{13}C {^{1}H} NMR (100 MHz, $CDCl_3$): 3,3'-(Bicyclo[1.1.1]penta-1,3-diyl)dipropiolaldehyde (**20**)

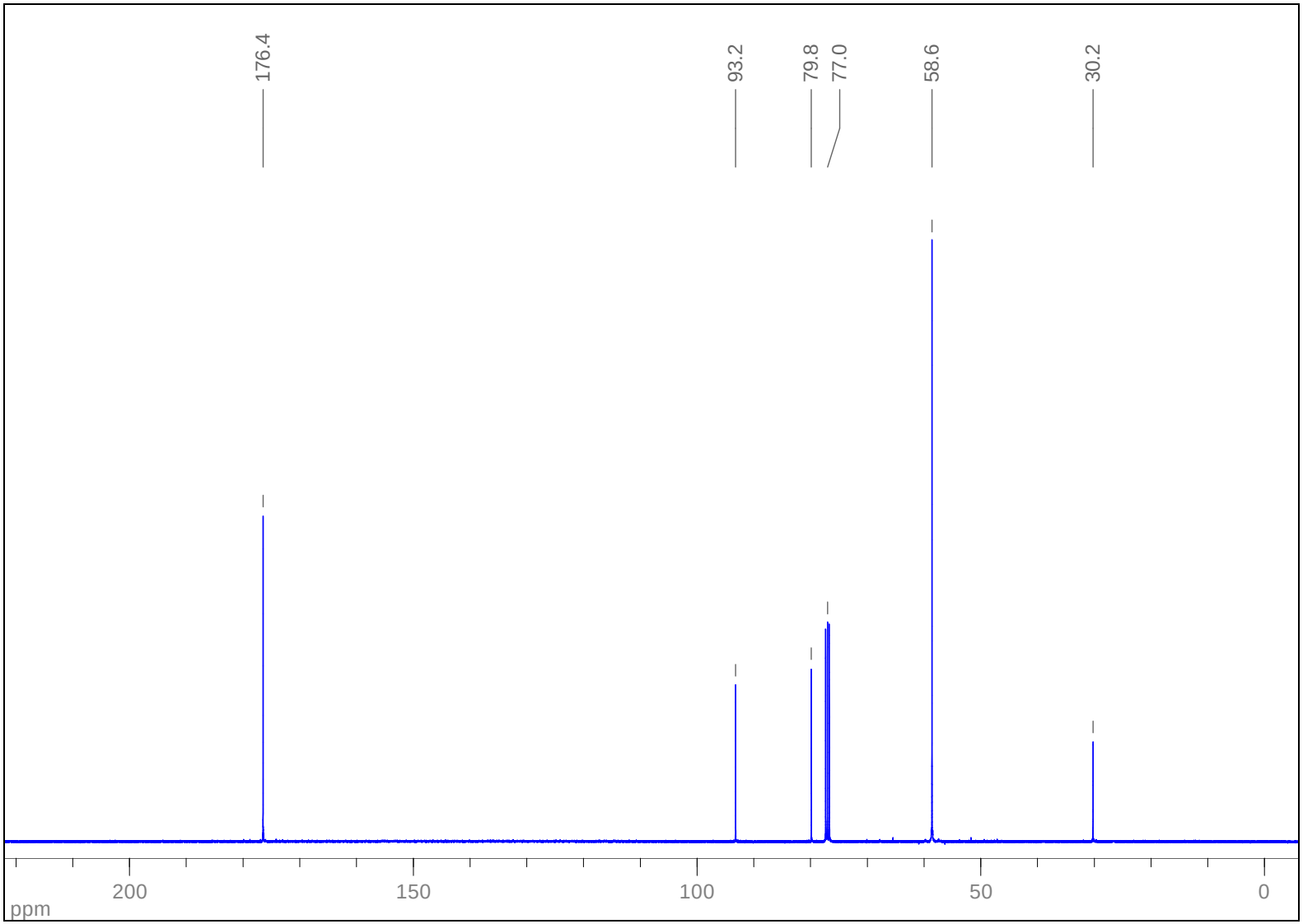

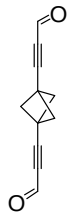

^{13}C APT NMR (100 MHz, $CDCl_3$): 3,3'-(Bicyclo[1.1.1]penta-1,3-diyl)dipropiolaldehyde (**20**)

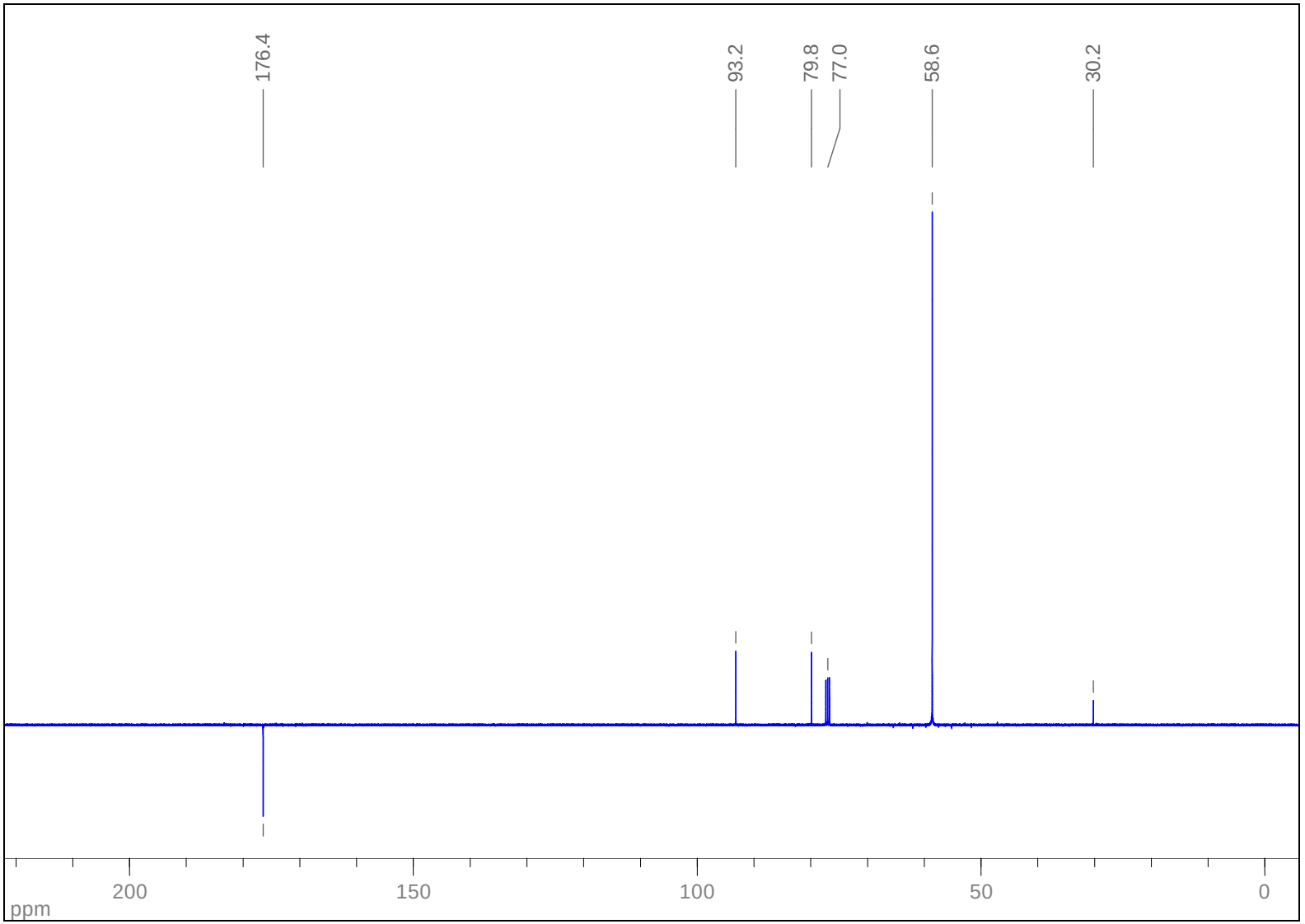

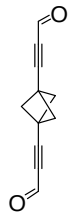

HSQC ($CDCl_3$): 3,3'-(Bicyclo[1.1.1]penta-1,3-diyl)dipropiolaldehyde (**20**)

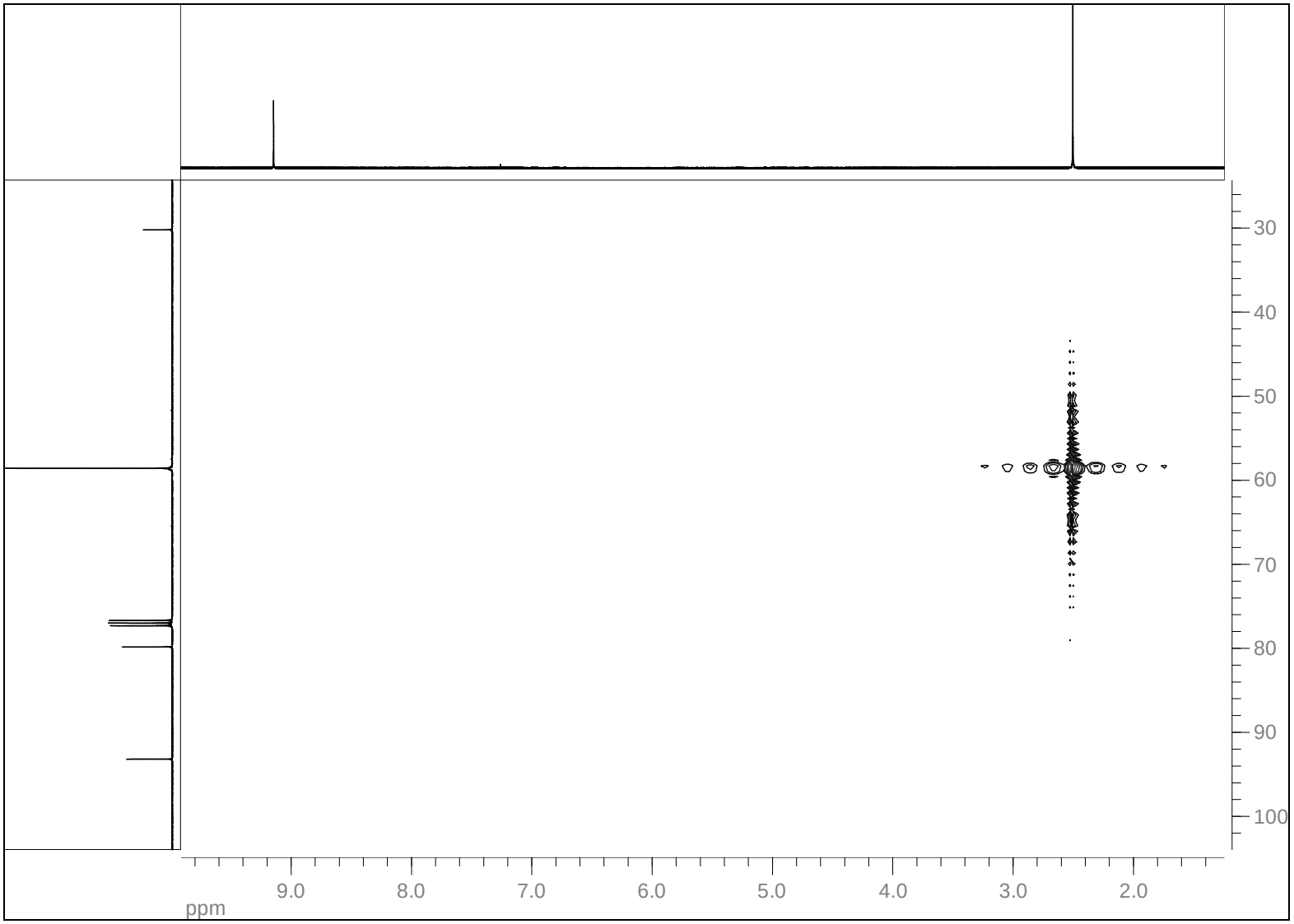

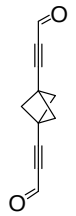

HMBC ($CDCl_3$): 3,3'-(Bicyclo[1.1.1]penta-1,3-diyl)dipropiolaldehyde (**20**)

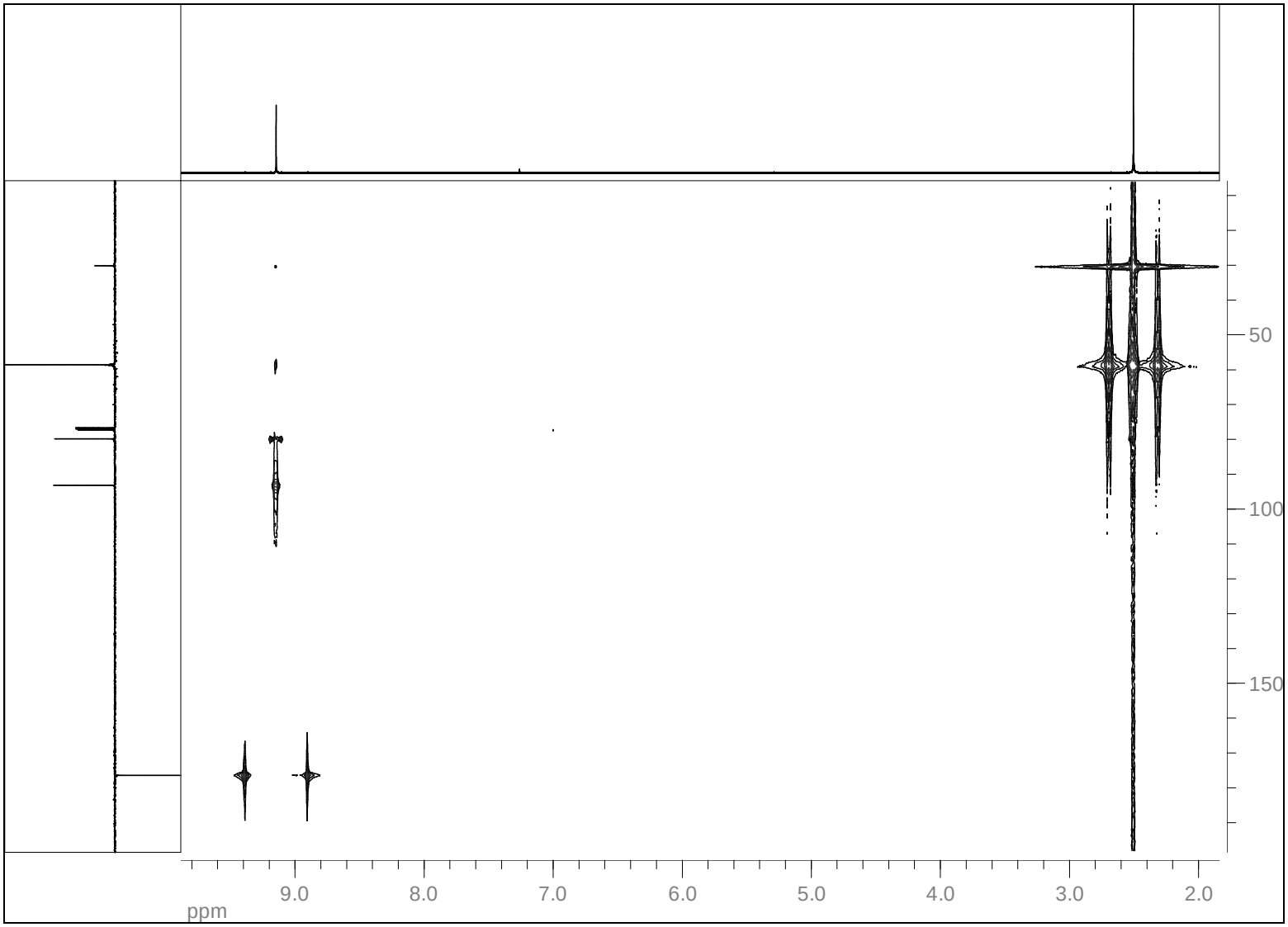

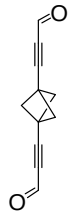

^{1}H NMR (400 MHz, $CDCl_3$): 1,3-Bis(4,4-dibromobut-3-en-1-ynyl)bicyclo[1.1.1]pentane (**21**)

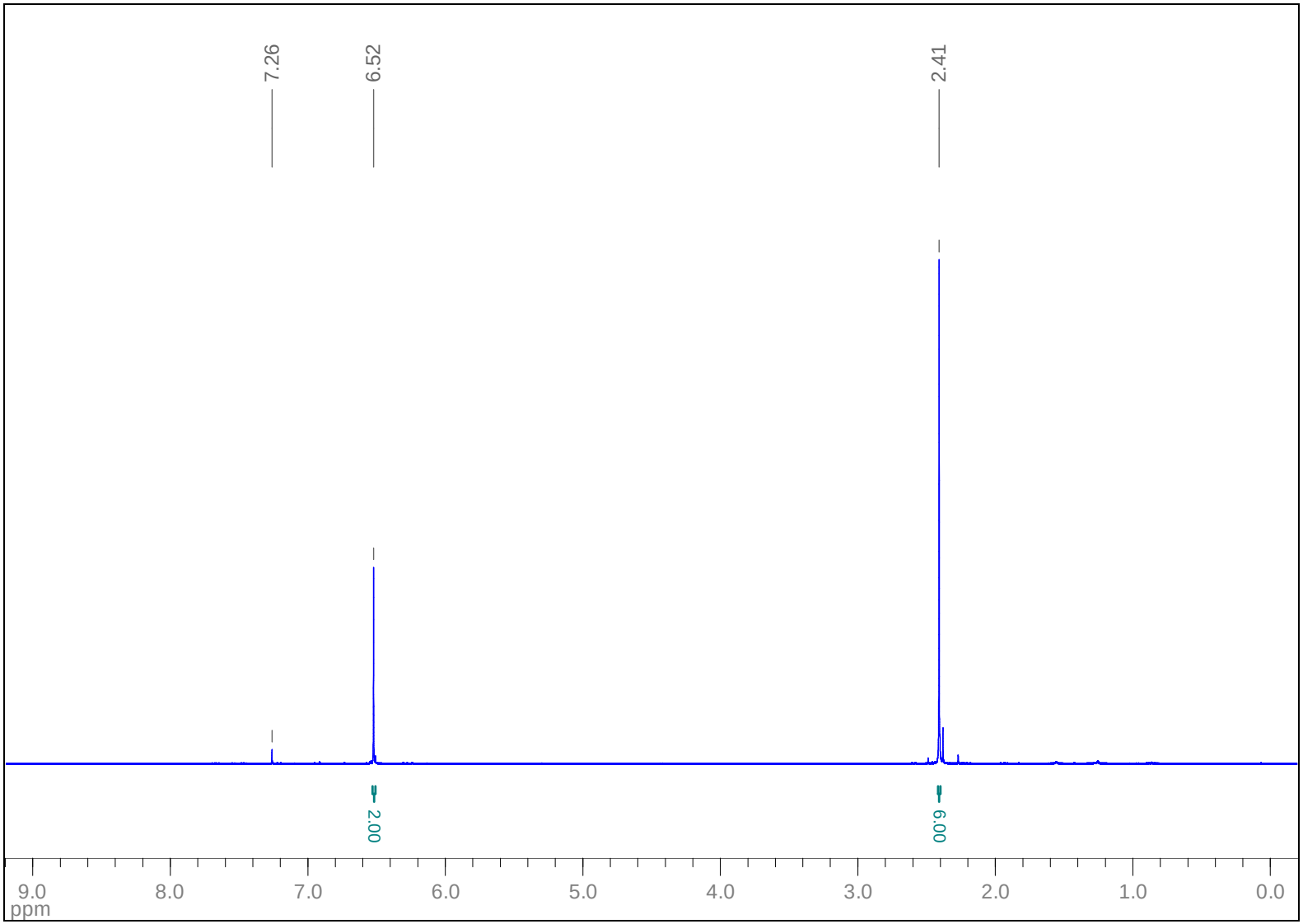

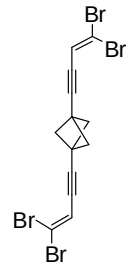

^{13}C {^{1}H} NMR (100 MHz, $CDCl_3$): 1,3-Bis(4,4-dibromobut-3-en-1-ynyl)bicyclo[1.1.1]pentane (**21**)

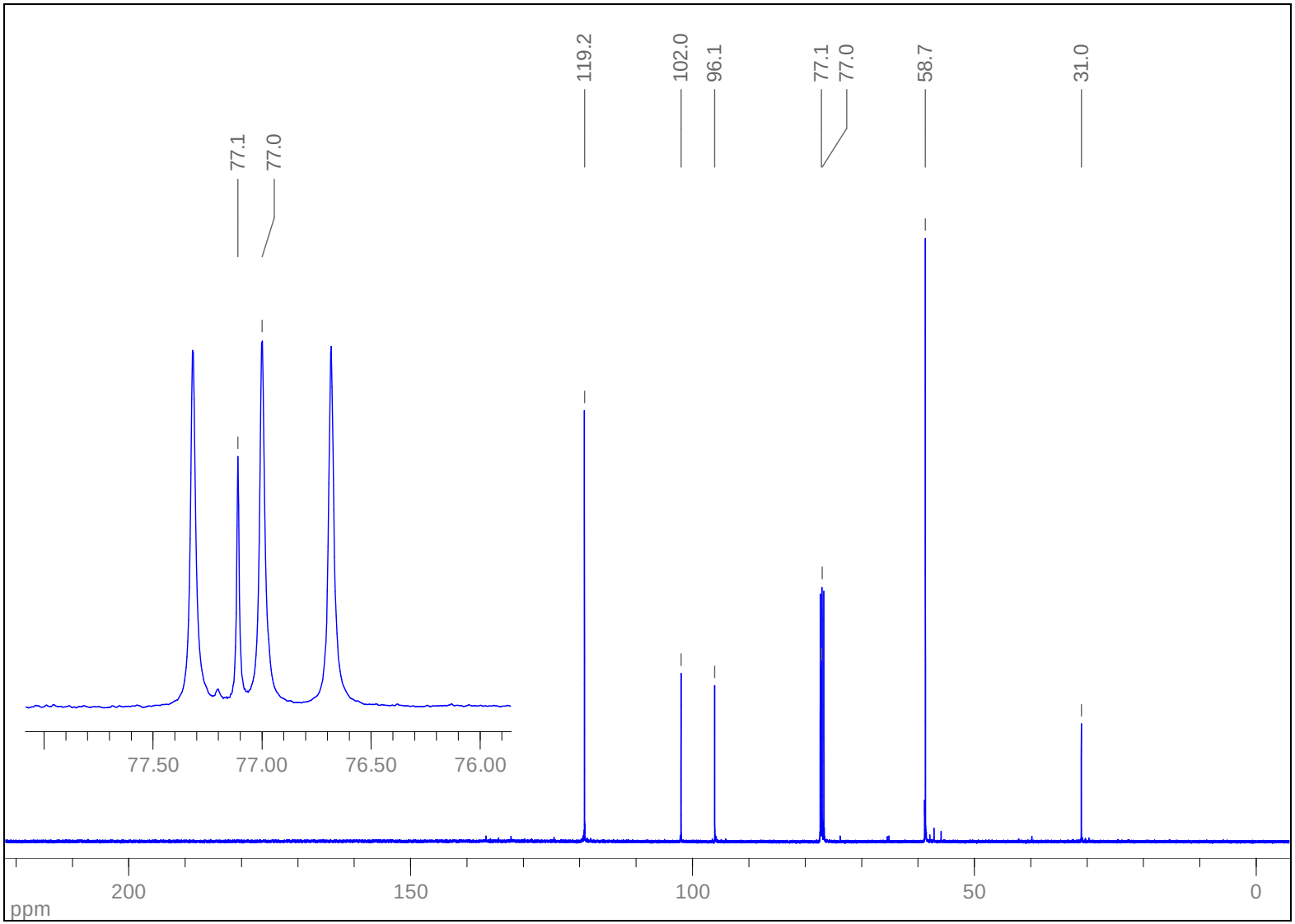

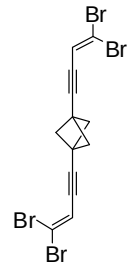

^{13}C APT NMR (100 MHz, $CDCl_3$): 1,3-Bis(4,4-dibromobut-3-en-1-ynyl)bicyclo[1.1.1]pentane (**21**)

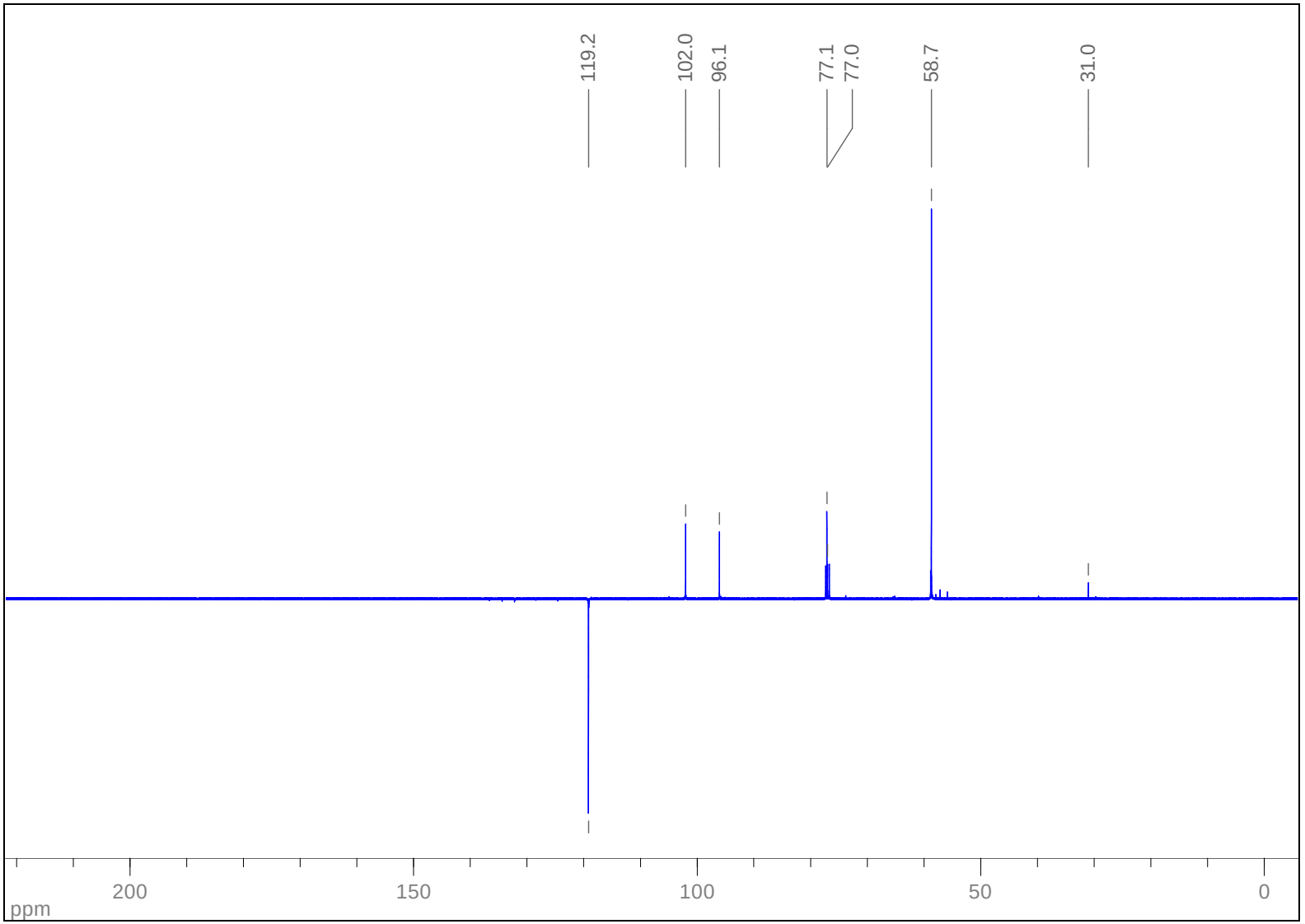

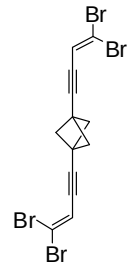

HSQC ($CDCl_3$): 1,3-Bis(4,4-dibromobut-3-en-1-ynyl)bicyclo[1.1.1]pentane (**21**)

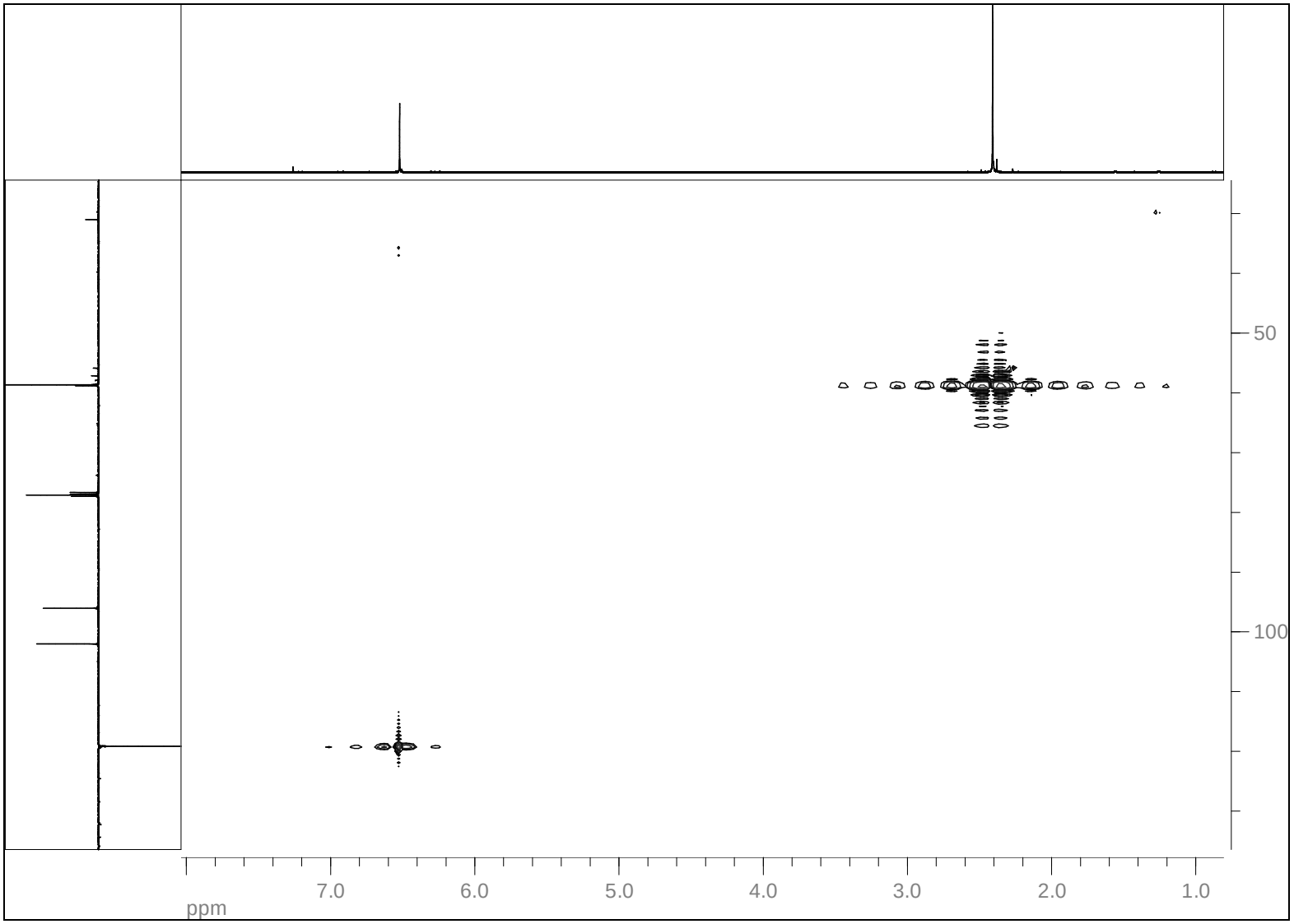

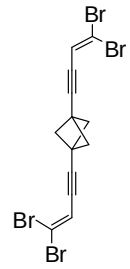

HMBC ($CDCl_3$): 1,3-Bis(4,4-dibromobut-3-en-1-ynyl)bicyclo[1.1.1]pentane (**21**)

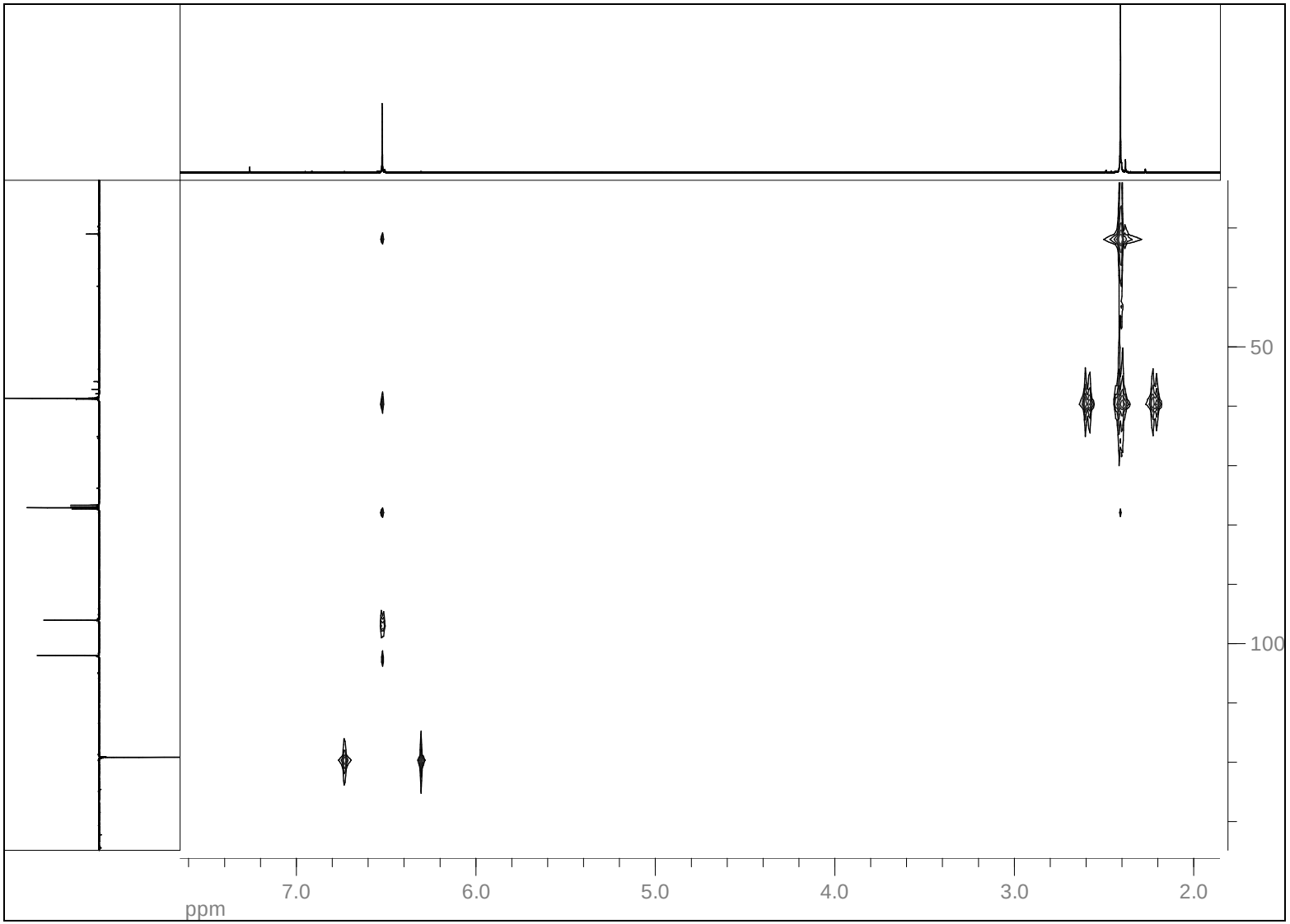

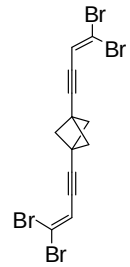

X-ray: 1,2-Bis(6-*tert*-butylpyridazin-3-yl)ethyne (**1**) (displacement ellipsoids are shown at the 30% probability level)

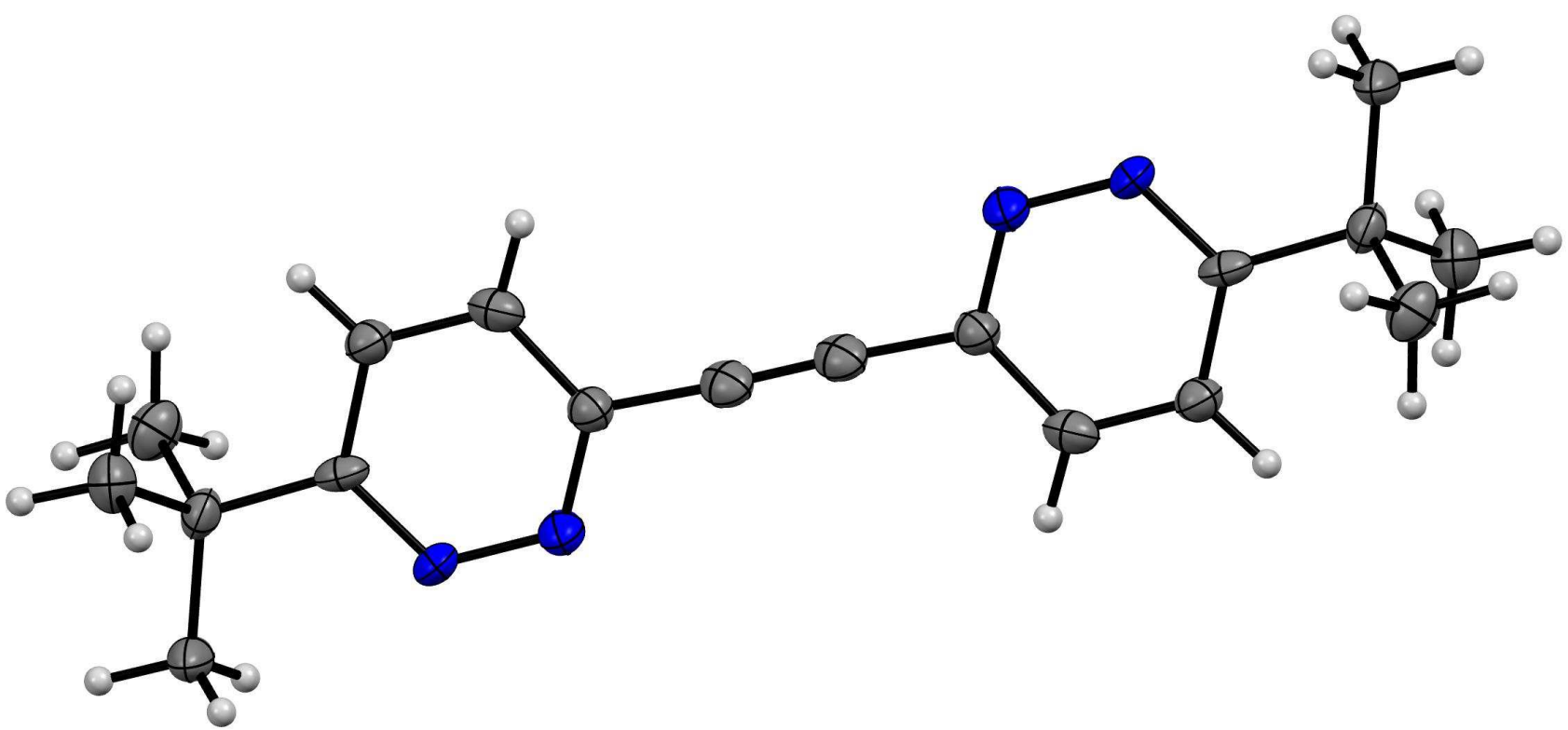

X-ray: Crystal packing of 1,2-bis(6-*tert*-butylpyridazin-3-yl)ethyne (**1**) (displacement ellipsoids are shown at the 30% probability level)

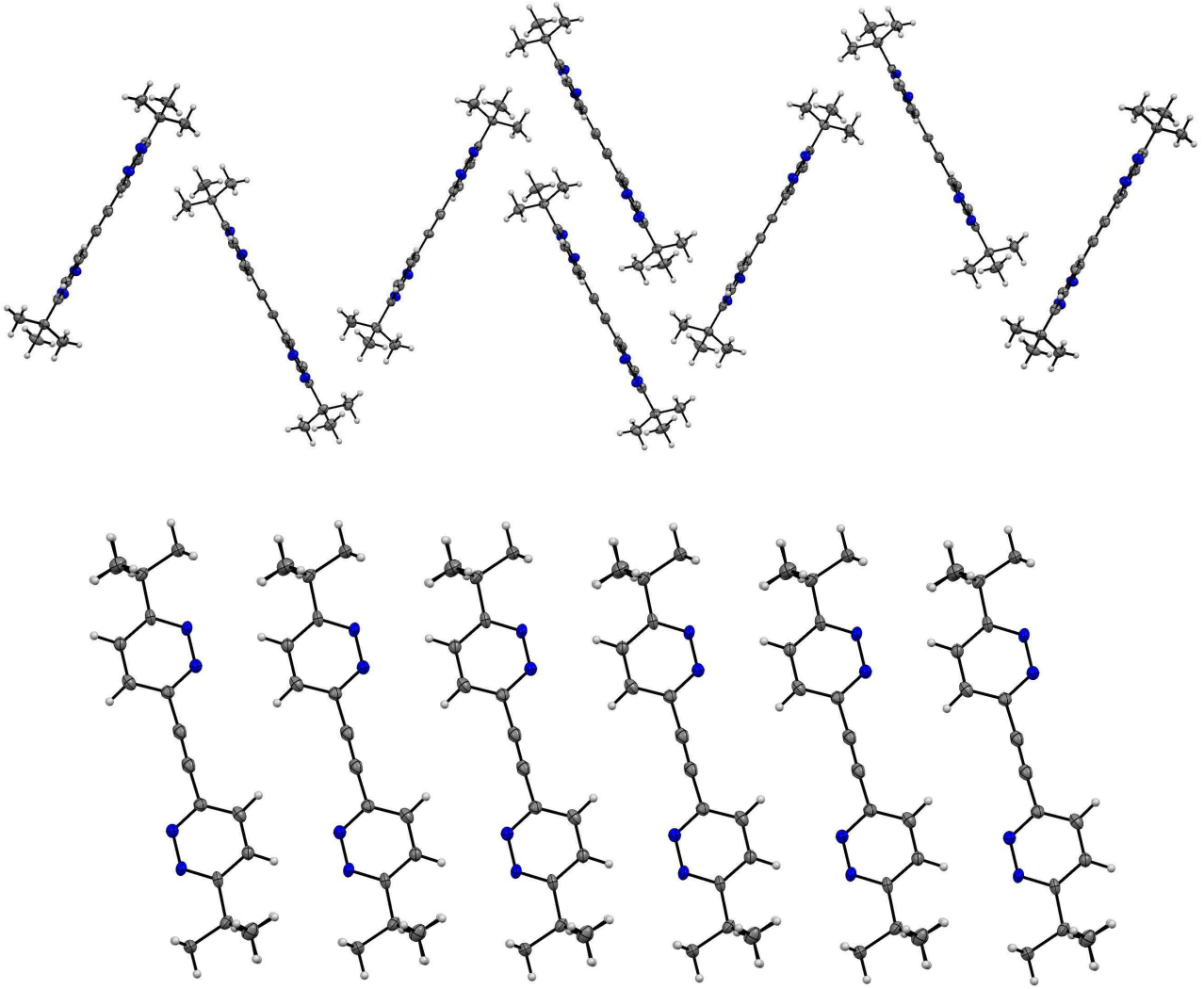

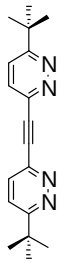

X-ray: 1,3-Bis((6-*tert*-butylpyridazin-3-yl)ethynyl)bicyclo[1.1.1]pentane (**2**) (displacement ellipsoids are shown at the 30% probability level)

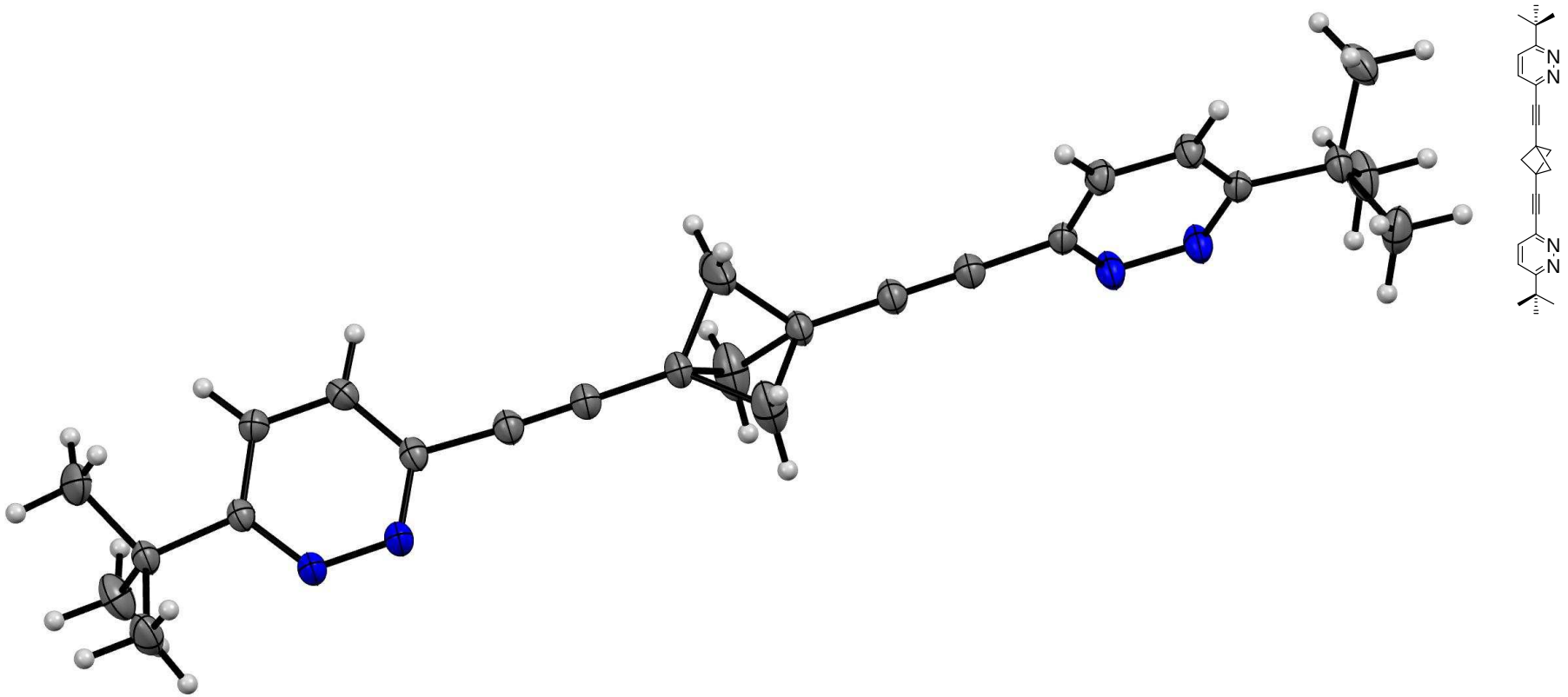

X-ray: Crystal packing of 1,3-bis((6-*tert*-butylpyridazin-3-yl)ethynyl)bicyclo[1.1.1]pentane (**2**) (displacement ellipsoids are shown at the 30% probability level)

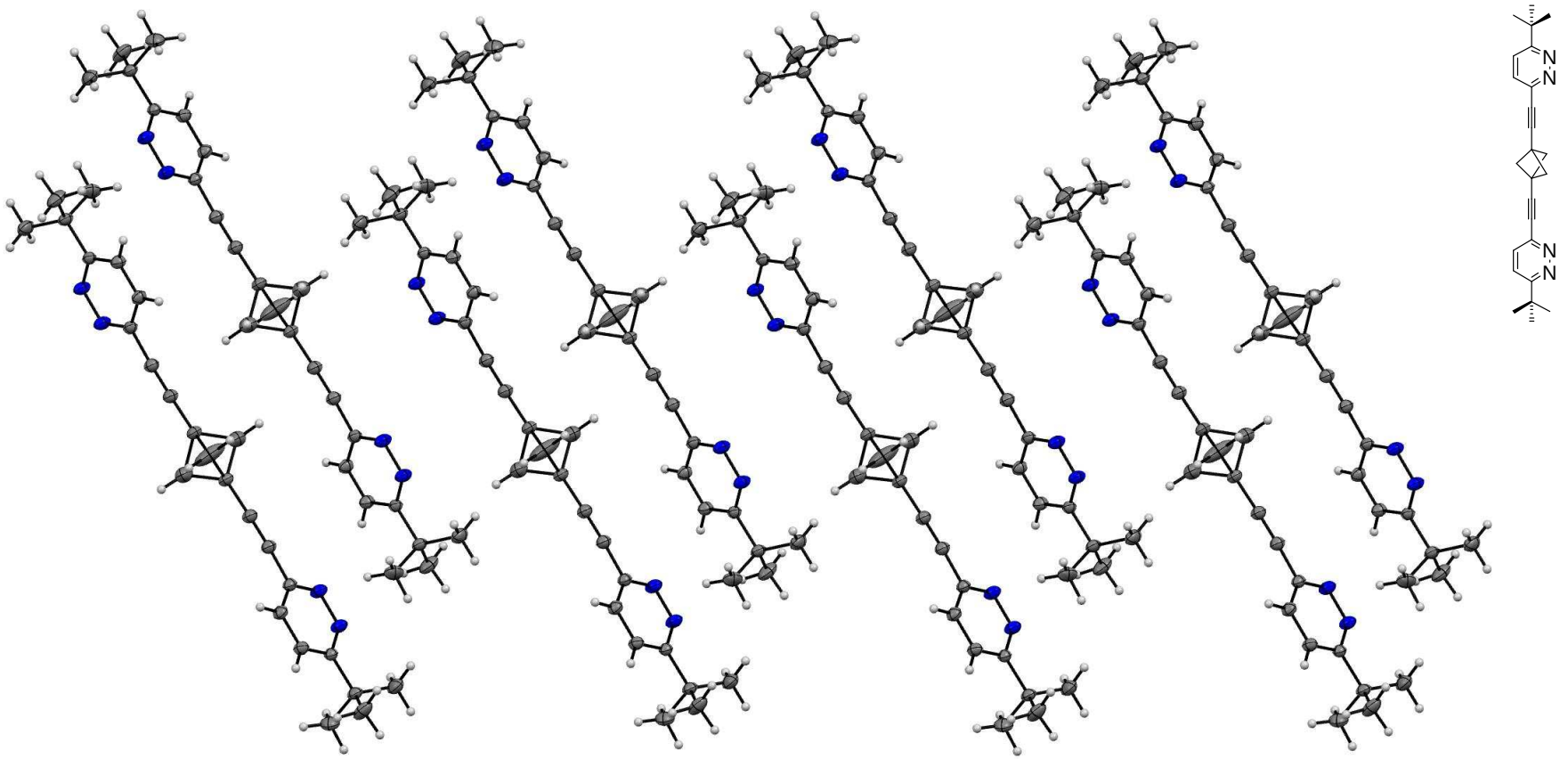

X-ray: 3-*tert*-Butyl-6-iodopyridazine (**9**) (displacement ellipsoids are shown at the 30% probability level)

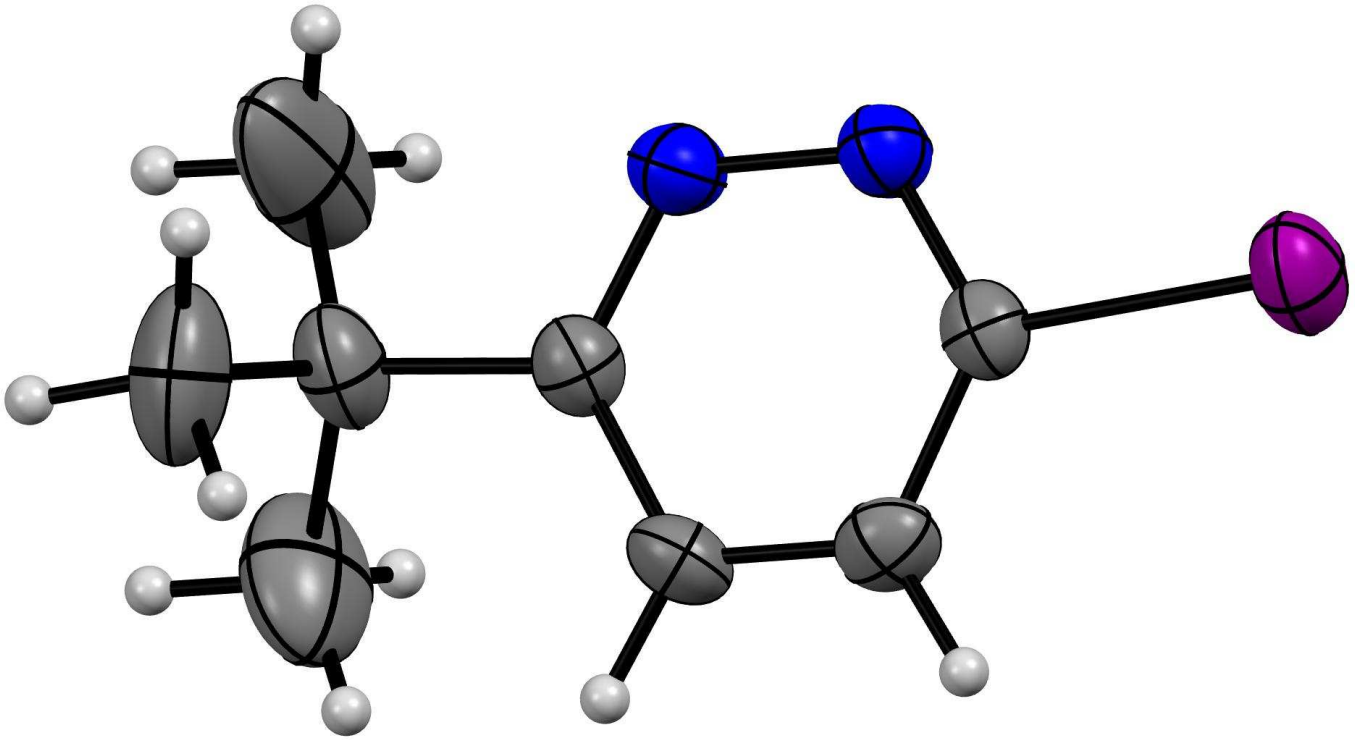

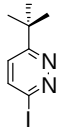

X-ray: Crystal packing of 3-*tert*-butyl-6-iodopyridazine (**9**) (displacement ellipsoids are shown at the 30% probability level)

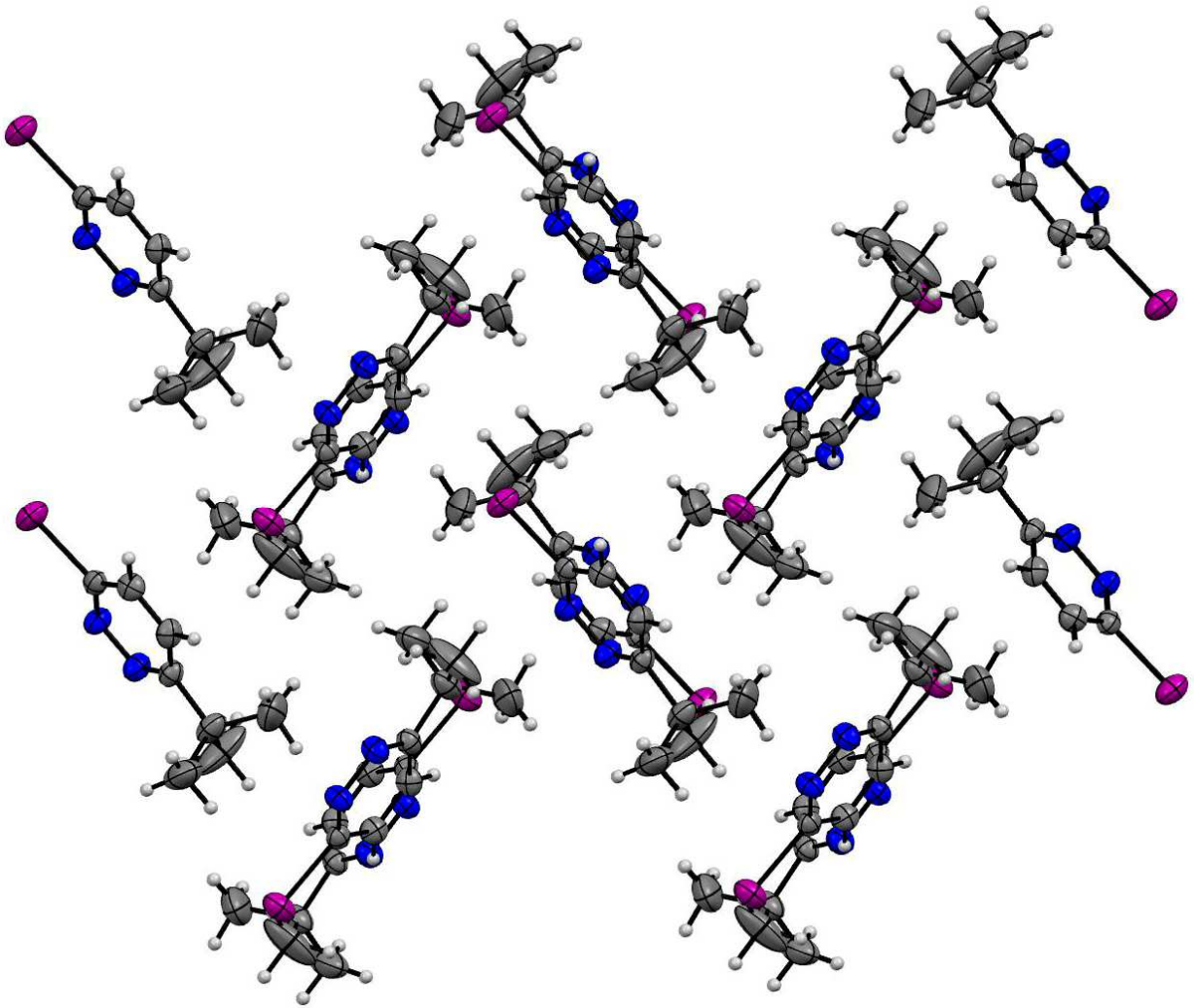

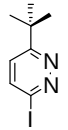

X-ray: 1,3-Di(buta-1,3-diynyl)bicyclo[1.1.1]pentane (**18**) (displacement ellipsoids are shown at the 30% probability level)

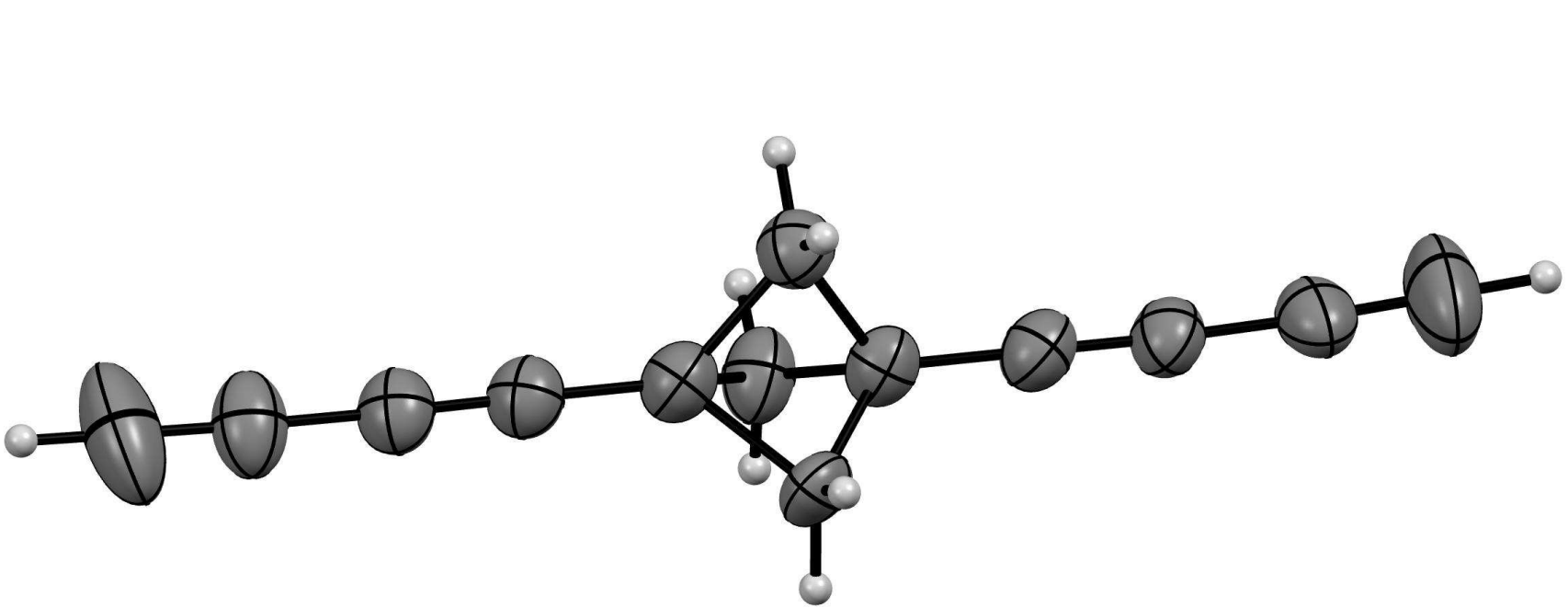

X-ray: Crystal packing of 1,3-di(buta-1,3-diynyl)bicyclo[1.1.1]pentane (**18**) (displacement ellipsoids are shown at the 30% probability level)

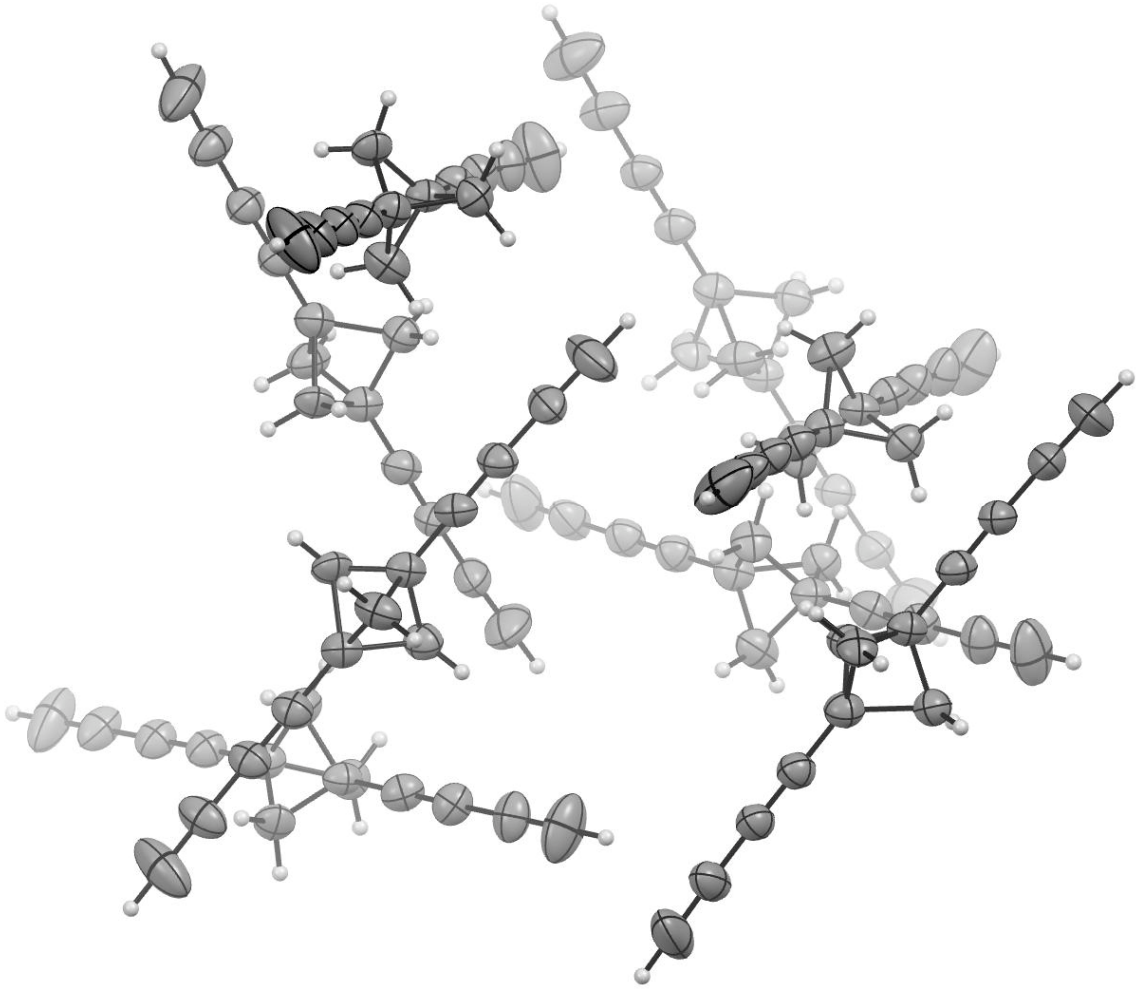

X-ray: 3,3'-(Bicyclo[1.1.1]penta-1,3-diyl)diprop-2-yn-1-ol (**19**) (displacement ellipsoids are shown at the 30% probability level)

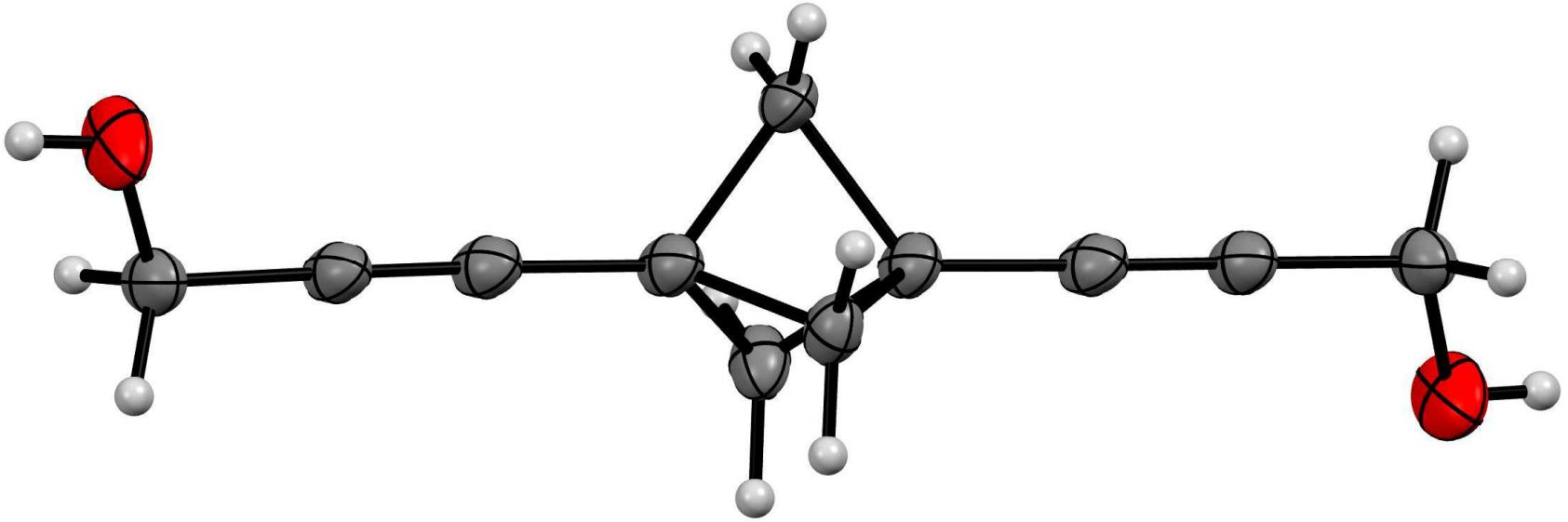

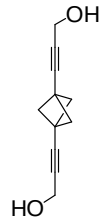

X-ray: Crystal packing of 3,3'-(bicyclo[1.1.1]penta-1,3-diyl)diprop-2-yn-1-ol (**19**) (displacement ellipsoids are shown at the 30% probability level)

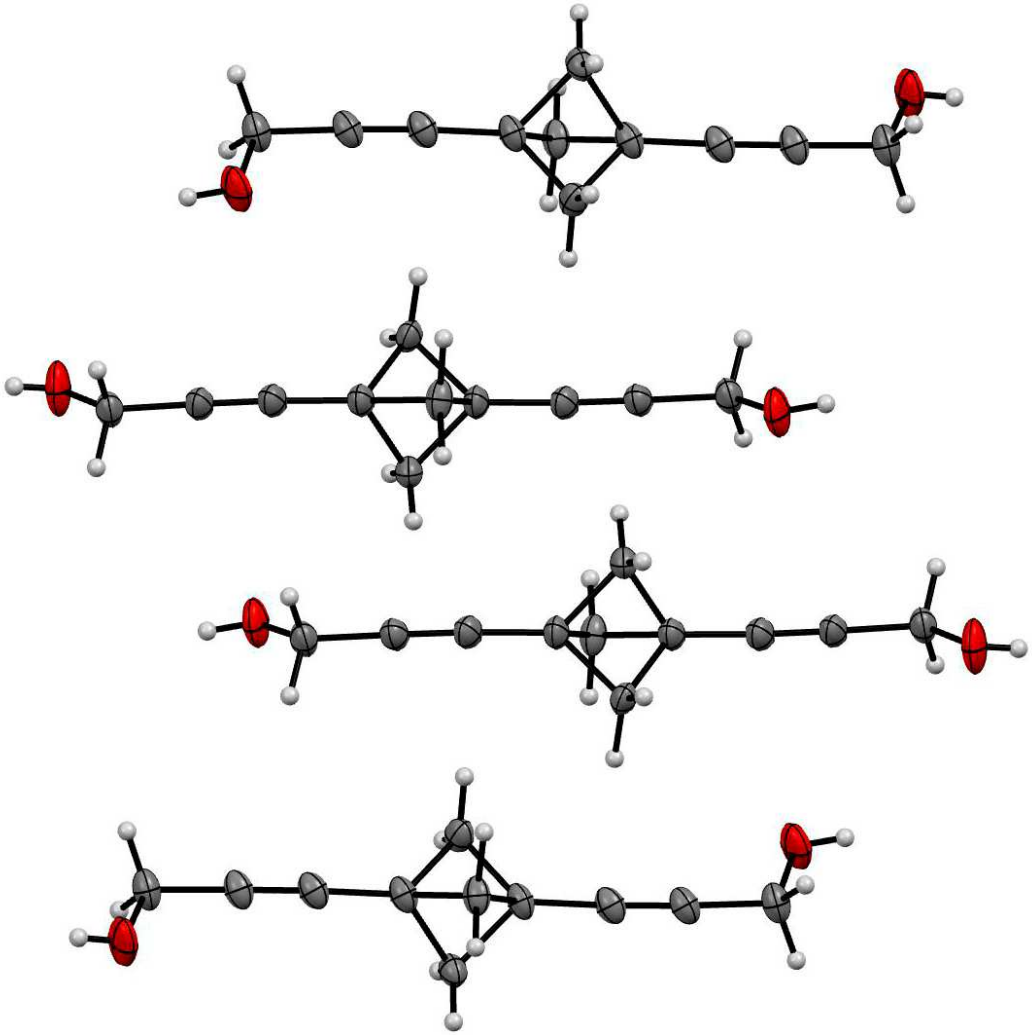

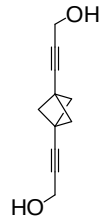

X-ray: 1,3-Bis(4,4-dibromobut-3-en-1-ynyl)bicyclo[1.1.1]pentane (**21**) (displacement ellipsoids are shown at the 30% probability level)

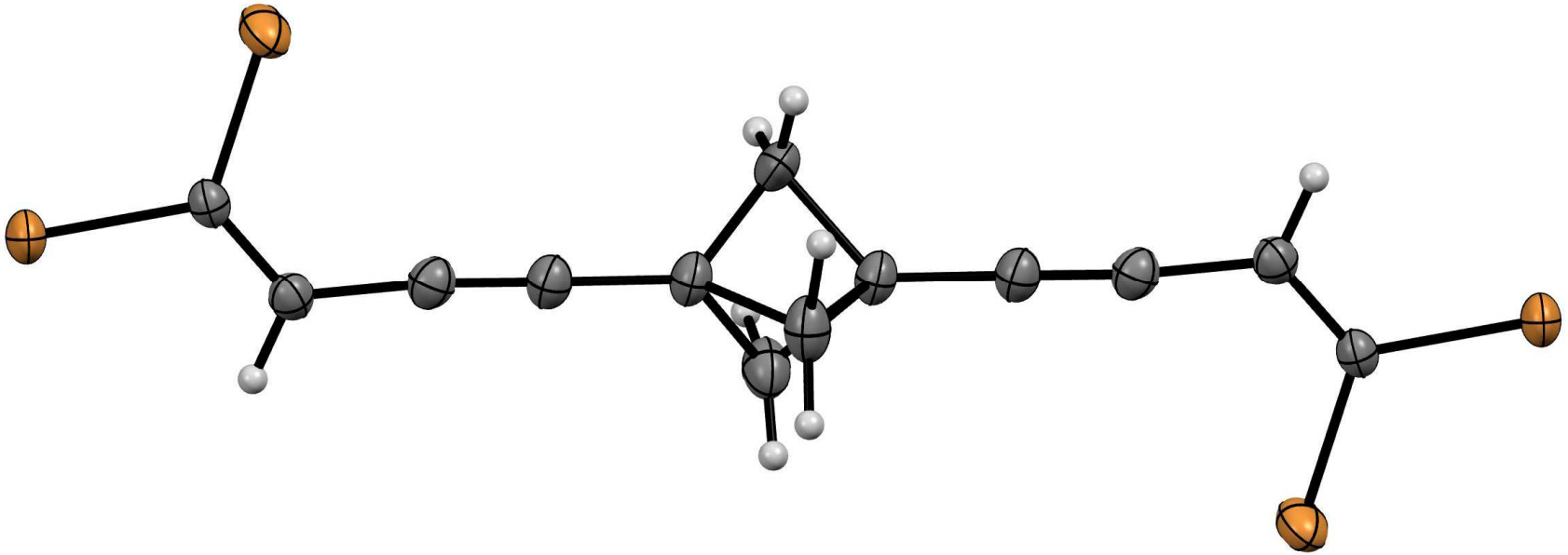

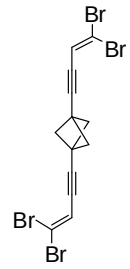

X-ray: Crystal packing of 1,3-bis(4,4-dibromobut-3-en-1-ynyl)bicyclo[1.1.1]pentane (**21**) (displacement ellipsoids are shown at the 30% probability level)